12-2012

Planet Formation in Transition Disks: Modeling, Spectroscopy, and Theory

Joseph Liskowsky
Clemson University, jliskow@clemson.edu

Planet Formation in Transition Disks: Modeling, Spectroscopy, and Theory

---

A Dissertation
Presented to
the Graduate School of
Clemson University

In Partial Fulfillment
of the Requirements for the Degree
Doctor of Philosophy
Physics

---

by
Joseph Paul Liskowsky
December 2012

Accepted by:
Dr. Sean D. Brittain, Committee Chair
Dr. Murray S. Daw
Dr. Dieter H. Hartmann
Dr. Bradley S. Meyer

Abstract

An important field of modern astronomy is the study of planets. Literally for millennia, careful observers of the night sky have tracked these 'wanderers', with their peculiar motions initiating avenues of inquiry not able to elucidated by a study of the stars alone: we have discovered that the planets (as well as Earth) orbit the sun and that the stars are so far away, even their relative positions do not seem to shift perceptibly when Earth's position moves hundreds of millions of miles. With the advent of the telescope, and subsequent improvements upon it over the course of centuries, accelerating to the dramatically immense telescopes available today and those on the horizon, we have been able to continuously probe farther and in more detail than the previous generation of scientists and telescopes allowed. Now, we are just entering the time when detection of planets outside of our own solar system has become possible, and we have found that planets are extraordinarily common in the galaxy (and by extrapolation, the universe). At the time of this document's composition, there are several thousand such examples of planets around other stars (being dubbed 'exoplanets'). We have discovered that planets are plentiful, but multiple open questions remain which are relevant to this work: How do planets form and, when a planet does form from its circumstellar envelope, what are the important processes that influence its formation?

This work adds to the understanding of circumstellar disks, the intermediate

stage between a cold collapsing cloud (of gas and dust) and a mature planetary system. Specifically, we study circumstellar disks in an evolved state termed 'transition disks'. This state corresponds to a time period where the dust in the disk has either undergone grain growth - where the microscopic grains have clumped together to form far fewer dust particles of much higher mass, or the inner portion (or an inner annulus) of the disk has lost a large amount of gas due to either a massive planet accreting the material onto it or via a photoevaporation process whereby the central star's radiation field ejects material from the inner disk out of the bound system in the the interstellar medium. It is presumed that this phase is the last gasp of the planetary disk's evolution before the debris disk stage and before a fully formed solar system evolves.

Our work specifically focuses on one object of this transition disk class: HD 100546. We add to the understanding of transition disks by showing that a model where rovibrational OH emission in the NIR is preferentially emitted along the 'wall' of the disk is consistent with observations, and furthermore that adding an eccentricity to this 'wall' component is required to generate the necessary observed line shape. In conjunction with this observation we present supporting material which motivates the usage of such an eccentric wall component in light of predictions of the influence of giant planet formation occurring within the disk.

Dedication

For Brian Donehew - a close friend who recently passed away. Your presence will be sorely missed. Life is less bright without you and I truly hope I will see you again.

Acknowledgments

I would like to thank many people for making this document a reality. First, I would like to thank my advisor, Sean Brittain, for helping me to understand the field and for my flexible work environment. Writing this document in absentia benefits it and my sanity. The large portion of the work I've done in graduate school would not have been possible without multiple trips to Mauna Kea, which I was fortunate enough to have the opportunity to visit during my tenure at Clemson, thanks to Sean's willingness to take me along. His many hours of editing manuscripts and text are noted and appreciated. His edits and comments have made me a much more clear and concise technical writer, though there is still likely work to be done in that regard. It has been a privilege working with you over the last five years. I would like to thank Terrence Rettig and Theodore Simon for their input into our work on FUors. It has been a pleasure working with both of you and I thank you for your insights. The work pertaining to HD 100546 could not have been as polished or as well thought-out without the significant and astute insights from both Joan Najita and John Carr. Their work on this project was essential to its completion. Many of the professors at Clemson, from whom I have learned a great deal of the physics I sought to learn while applying for graduate programs, I owe very much. Sincere thanks go to Murray Daw from whom I learned a great deal of theory in mechanics and statistical thermodynamics. This has served me well in my career thus far. I

have also become more of a philosopher than I thought I would when arriving at Clemson, to which I owe Dr. Daw thanks, particularly in the area of the foundation of quantum mechanics. I owe thanks to Catalina Marinescu from whom I learned a considerable amount of quantum theory, which helps in understanding everything that I do. Spectroscopy would not make any sense without the knowledge I gained from her. I would like to thank all of the astronomy professors in the department for all of the knowledge you have bestowed upon me through discussion, through classes, and during talks: Dieter Hartmann, thank you for the many discussions about GR and for the many pedagogical and life discussions we've had. Mark Leising, thank you for the classes you've taught, the excellent opportunity to work on the planetarium, and the latitude you've given us developing its content. Brad Meyer, thank you for the many (many) classes you have taught and your collaboration on the network code, and though it is in its infancy I believe we're creating a useful tool for the community. I am thankful for getting to know you and your family over the last five years. I would also like to thank all of the graduate students with whom I've interacted over the past five years. These acknowledgements do not convey the depth of the gratitude I feel for all of your efforts and our interactions. I'd like to thank two people I've never met and never will for getting me interested in astronomy in the first place: Carl Sagan and Jack Horkheimer, who taught me to dream big and to keep looking up. Most importantly, I'd like to thank my dad for everything he has sacrificed so that I could get this far. It hasn't gone unnoticed.

Table of Contents

List of Tables

List of Figures

Chapter 1

Early Stellar Evolution

1.1 Star Formation

Star formation occurs in vast molecular clouds which contain mostly hydrogen, but also relatively small amounts of other atoms, molecules, and dust grains. These molecular clouds have up to 10^6 $M_\odot$ in mass and extend for $\sim 10^2$ pc for the largest members (Solomon et al., 1979) which are known as Giant Molecular Clouds (GMCs; Murray, 2011). These clouds have star forming regions, which are typically identified by an association with hot, bright young stars (type O or type B), dust extinction, and a local enhancement in the relative particle density. Figure 1.1, the Orion Nebula, shows an example of this. The young, forming stars are those in red near the top right. They lie along the observable filamentary structures which seem to connect the stars (bright spots). Larger, more evolved stars are shown in blue. The formation of each star in this image is due to gravitational contraction of a volume of gas in the molecular cloud, in this case, along a filament. In this contraction, the force of gravity exceeds the pressure support of the gas, breaking the hydrostatic equilibrium and forming a collapsing region of rotating gas, as it is assumed that the

collapsing cloud has non-zero initial angular moment, which it loses slowly. As the cloud collapses, a protostar forms from its core and a circumstellar disk forms around it. This protostellar system is the precursor to an evolved solar system. This process, which encapsulates essentially all star formation, constitutes the Nebular Hypothesis, which was initially posited by natural philosophers in the 18^{th} Century. The density required (specifically, mass) to accomplish this gravitational contraction is the subject of the next section.

Figure 1.1 The Orion Nebula in the infrared. Objects rendered in red are imaged at 160μm, objects rendered in blue have been imaged at 8μm and 24μm, while objects rendered in green have been imaged at 70μm. Courtesy NASA/JPL-Caltech

1.2 Jean's Mass

Within a molecular cloud, the gravitational force pulls matter together, however this process is damped if the average velocity of the gas molecules due to some non-zero temperature yields a thermal energy greater than the potential energy of gravity. Therefore, the cloud, or a portion of the cloud will collapse under gravity for some low temperature T. For typical cloud densities this is $\sim 10\ K$. If we consider the cloud to be a sphere and the gas to be ideal, which is a good approximation for molecular cloud densities, being many orders of magnitude less dense than air at sea level, we can calculate the minimum mass a sphere must contain at a temperature T such that it will collapse under the influence of gravity. This is typically derived by using the virial theorem and substituting in the gravitational potential energy for a sphere of some prescribed density and the kinetic energy of all the particles (parameterized by a temperature T), and solving for the mass (Jeans, 1902). The so-called Jean's mass is

$$M_J = (\frac{5kT}{G\mu m_H})^{3/2}(\frac{3}{4\pi\rho})^{1/2}. \tag{1.1}$$

Here, G is the gravitational constant, μ is the mean molecular mass, m_H is the mass of a single hydrogen atom, k is Boltzmann's constant, and ρ is the density of the medium. Solving the equation of motion of a particle in the sphere, a free-fall timescale can be calculated:

$$\tau = (\frac{3\pi}{32G\rho})^{1/2}. \tag{1.2}$$

This prescription assumes that the cloud collapses isothermally and therefore causes a homologous collapse. As a large cloud collapses, it may exceed the Jean's

mass and portions of the cloud may satisfy the Jeans criteria, allowing multiple cores to form. This process is called fragmentation. For stellar masses under $\sim 8M_{\odot}$, this collapse follows to the protostellar phase where a quasi-hydrostatic star contracts slowly onto the main sequence. Its evolution then is dictated by the equations of stellar evolution:

$$\frac{dP}{dm} = -\frac{Gm}{4\pi r^4} \tag{1.3}$$

$$\frac{dr}{dm} = \frac{1}{4\pi r^2 \rho} \tag{1.4}$$

$$\frac{dT}{dm} = -\frac{3\kappa L}{64\pi^2 acT^3 r^4} \tag{1.5}$$

$$\frac{dL}{dm} = q \tag{1.6}$$

where m is the Lagrangian mass coordinate, κ is the opacity, L is the luminosity, a is the radiation constant, and q is the energy generation rate from nuclear reactions. The first equation gives the pressure gradient, which depends on mass shell. The second equation is a relation between the Lagrangian mass coordinate and the radial coordinate. The third equation relates the temperature gradient to the temperature of the shell and the luminosity passing through it. The fourth equation gives the energy generation rate via nuclear fusion. Typically, an a priori equation of state relates the pressure and temperature, while various other power law dependences are used to simplify other variables (for instance, q is often written as a power law in T). Numerical integration of these differential equations yields long term behavior and evolution of the star. After the isothermal collapse phase, the star undergoes several

stages of circumstellar evolution before moving onto the main sequence. Depending on its mass, the star may achieve main sequence status before the disk is fully cleared (eg. Vega). The next section describes, in detail, the various phases a circumstellar disk goes through on its path to becoming an evolved solar system.

1.3 Phases of a Circumstellar Disk

1.3.1 Massive Disk

As the collapsing cloud begins to rotate faster (due to the conservation of angular momentum), a dense central core forms, and the cloud flattens out into a flared circumstellar disk. In Fig. 1.2, this process is broken down into stages to facilitate an explanation: In frame A, the cloud is collapsing isothermally as the opacity of the dust at these densities is optically thin. The entire collapsing cloud complex has a small intrinsic angular momentum (around principal axis $\hat{z}$) which must be conserved during the evolution of the system. Because parcels of gas and dust near the top of the idealized sphere lack support in the $\hat{z}$ direction, they tend to drift to the x-y plane, though they are supported in the there by the centripetal force of rotation around the central axis (frame B). The net result is a flattening of the rotating sphere into a disk, conserving angular momentum (frame C). This process takes approximately 10^4 years for densities typical of these cloud cores and filaments, and results in a central protostar contracting towards the main sequence, a circumstellar disk surrounding and accreting material onto the central star via episodic accretion events (FUors; Hartmann & Kenyon, 1996), and infalling material from the envelope. The various stages of evolution of this massive gas-rich disk can be tracked by examination of the SED for each source.

1.3.2 Stages of Protostellar Evolution

Observations of the SEDs of Young Stellar Objects (YSOs) have shown interesting variety in the infrared, as many YSOs show a remarkable IR excess. Presumably, the excess in any of these SEDs comes from dust grains radiating energy which are embedded in the circumstellar disk. Lada & Wilking (1984); Lada (1987) invented a classification scheme for the differences in infrared slope of the SEDs of YSOs: Class I sources have a positive slope in the infrared portion of the SED and correspond to an incipient protostar and its massive circumstellar disk. Class II have essentially a flat slope in the IR, where the star has contracted towards the main sequence and the disk has accreted a large amount of its mass onto the star, diminishing the infrared excess. Class III have a negative slope or the red excess is small and is indistinguishable from the stellar SED, implying the disk is essentially emptied of material and is optically thin. Andre et al. (1993) introduce Class 0 sources which represent an isothermally collapsing cloud that has not fully formed a disk structure and is in an earlier stage of protostellar evolution than Class I (Fig. 1.3).

Class I sources are best associated with a massive disk that is accreting matter onto the central star, providing it with its eventual total mass. This phase takes

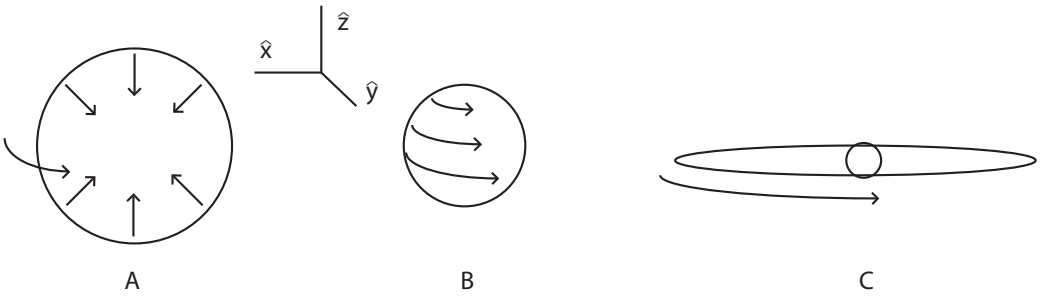

Figure 1.2 Contraction

approximately 10^5 yr and is characterized by an emptying out of the protostellar cloud. Most of the material is accreted onto the protostar or onto the circumstellar disk by the end of this phase. As material from the disk is accreted onto the surface of the protostar, the disk mass decreases. After approximately 10^6 yr, the mass of the disk has dropped to 1% of the protostar's mass. This corresponds to a Class II source. After $\sim 10^7$ yr, the disk has been mostly cleared of gas (Haisch et al., 2001) and the remnants are the solid objects formed from grain growth in the disk midplane. In the inner part of the disk, mostly rocky material is formed via grain growth, but beyond the frost line ice particles from the μm scale to 10^3 km objects ('dwarf' planets) are formed. In this Class III scenario, the the gas has been accreted onto the star or planets, or ejected from the solar system in high velocity jets along the magnetic axis of the star, or via interaction with the strong stellar winds generated in the photosphere. Class III objects are best described as 'debris disk' systems, where the disk is optically thin and the system mostly contains solid phase materials in a planar orbit around the central star. Between disks in Class II and Class III systems are transition disks, which exhibit an optically thin disk in the inner ∼few AU from the central star, and an optically thick disk exterior to the inner disk. This 'clearing-out' of the inner part of the disk can have multiple causes and introduces an uncertainty in the interpretation of the SED. Examples of SEDs of YSOs are shown in Fig. 1.4. Transition disks are discussed in more detail below.

1.3.3 Transition Disks

Transition disks are laboratories for testing gas dissipation mechanisms. Transition disks have optically thin inner disks (up to $\sim$ 70AU) with optically thick outer disks. Modeling of SEDs of these objects indicates that dips in the SEDs can be

attributed to gaps in the disks on the order of several AU, as in TW Hydra and GM Aurigae (Koerner et al., 1993; Calvet et al., 2002, 2005). These gaps can be created by a planetesimal accreting material (Quillen et al., 2004). Eventually, these gaps would cut off replenishment of the inner disk and the inner disk accretes onto the central star on the viscous timescale. Measurements of transition systems using high angular resolution later showed that the disks were cleared up to $\sim$ 10AU, at which distance the typical viscous timescale is too long to clear the disk by the measured ages (10^7 yrs). The implication is that multiple planets must be clearing the inner disk simultaneously. Hydrodynamic simulations performed show that the optically thin region cannot be formed by a single planet sculpting the disk, they require multiple planets (Dodson-Robinson & Salyk, 2011).

1.3.4 Era of Planet Formation

As the disk clears, other processes are occurring in the disk. Grain growth allows the large numbers of small grains (μm size) to coagulate into larger objects. For typical densities in circumstellar disks, it takes $\sim 10^7\ yrs$ to form a 10 Earth-mass object. At this mass, the gravitational potential is sufficiently strong to overcome the kinetic energy of individual gas molecules with temperature of several hundred Kelvin such that the gas collapses onto the core to form a gas giant planet. Further accretion from the disk can enhance the mass of this object over multiple orbits. This process is known as the core accretion model. Further out in the disk, the temperature is much lower, but the timescale for grain growth is very long. Forming massive cores at distances of tens of AU is not likely on disk dissipation timescales. Therefore, if planets form at these larger radii, another formation mechanism must exist. If the gas is cold at $\sim$200K, small perturbations in the density of the gas can cause the gas

to locally collapse under gravity very rapidly, forming a Jupiter mass planet in only several thousand years. This formation process doesn't adequately explain the so-called 'Hot-Jupiters', however this issue is typically resolved by allowing the gas giant planets to form at large AU and then interact with other objects (planets, asteroids), exchange angular momentum, and migrate to smaller radii. If the planet formation scenarios are to be tested, test cases need to be found. Because transition disks exist at a point in protostellar evolution similar to the core-accretion timescale, they are natural targets for looking for forming (or formed) planets.

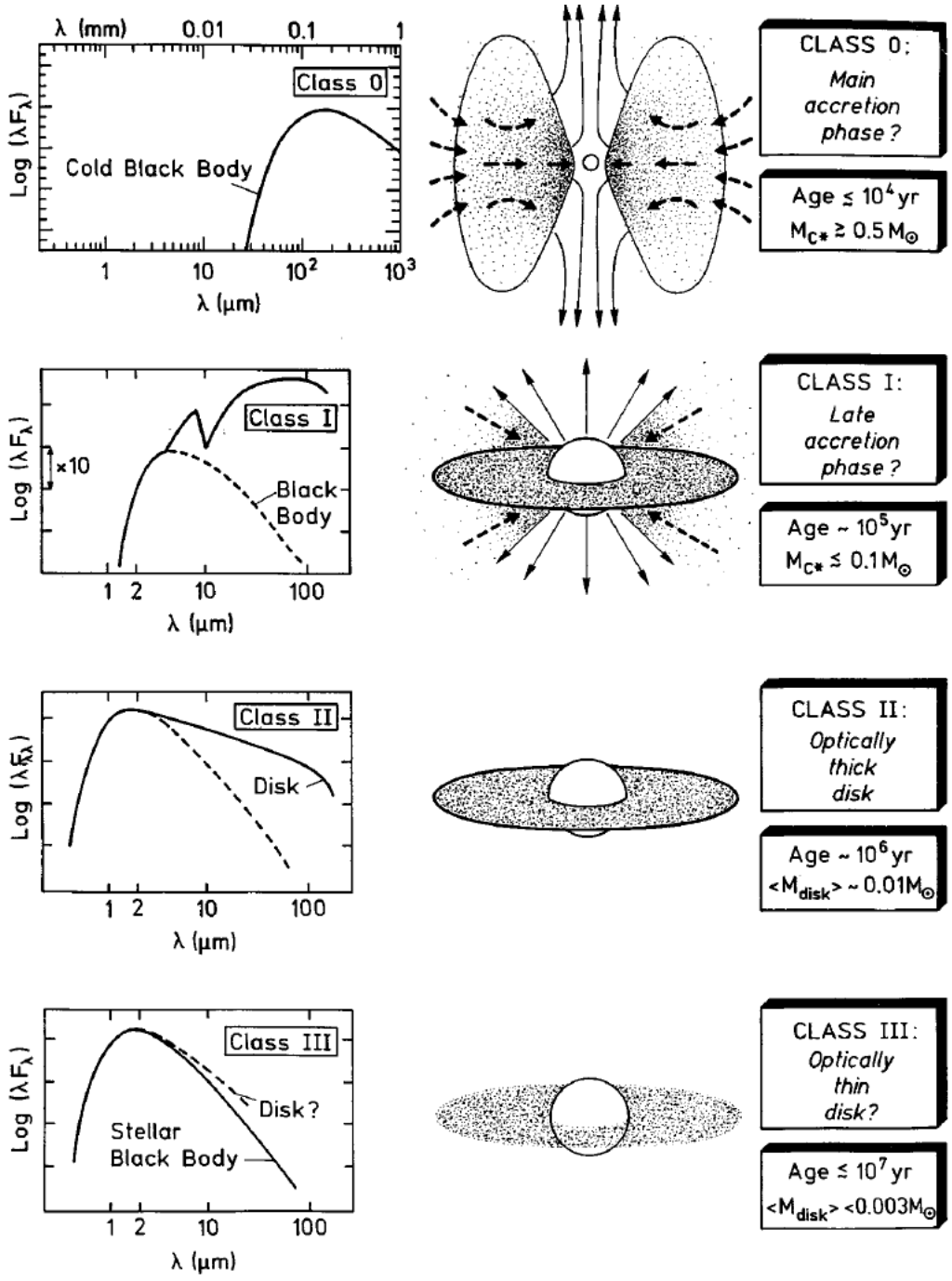

Figure 1.3 YSO Classes - (Figure 11 from Bachiller, 1996)

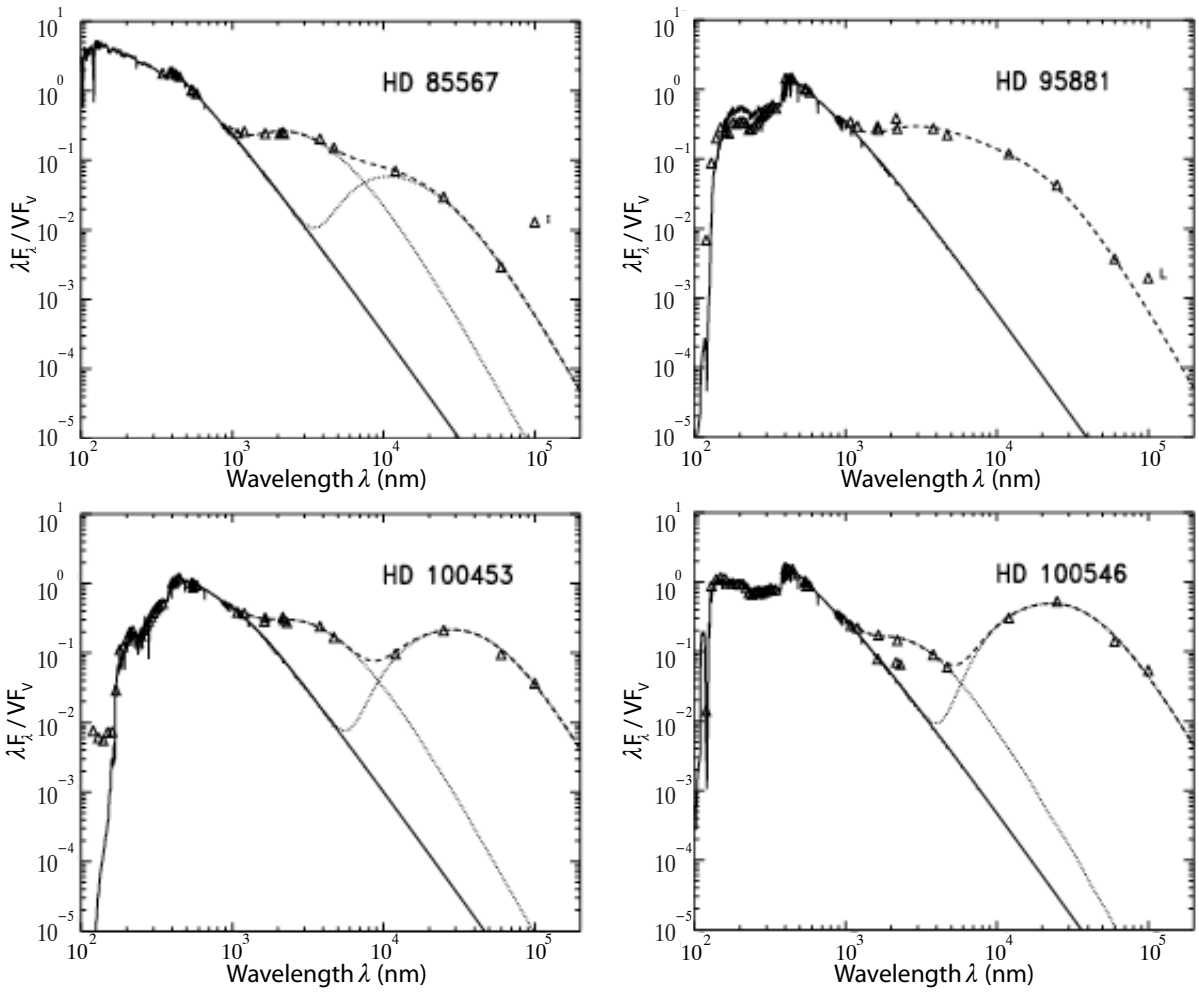

Figure 1.4 SEDs of YSOs - (Excerpt from Figure 1 from Malfait et al., 1998)

Chapter 2

Physics of Disks

2.1 Simple Hydrostatic Equilibrium Model

Like most stars on the main sequence, the vertical structure of a circumstellar disk is supported in a hydrostatic state - the pressure gradient of the gas is balanced by gravity. This is easily derivable by considering the forces on a parcel of gas in the disk (Fig. 2.1). In this case, the parcel of gas is cylindrical in the diagram, however this is entirely general; this derivation assumes that the vertical height dz is small compared to the length of the region under consideration - this is a thin slab. The derivation of the condition of hydrostatic equilibrium generally begins by a pressure equation

$$P_{up} - P_{down} = \Delta P = -\frac{1}{A}[\Delta m|g|] \tag{2.1}$$

where m is the mass of the gas enclosed in the volume, Δm = ρAdz, P_{up} is the pressure term from gas exerting an upward force on the parcel, P_{down} is the pressure term from gas exerting a downward force on the parcel, and g is the acceleration due

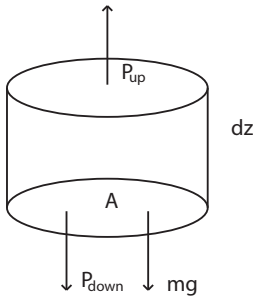

Figure 2.1 Diagram of a parcel of gas in hydrostatic equilibrium. The gravitational force on the parcel is balanced by the pressure gradient in the disk.

to gravitation from the mass of the disk.

Turning these Δ terms into perfect differentials and reorganizing terms, and noting that dm = ρAdz, we arrive at

$$\frac{dP}{dz} = -\rho|g| \tag{2.2}$$

where ρ is assumed to be constant throughout the collapsing cloud. From this equation, and given some physical dependence of g, it is possible to solve the differential equation for a physical situation. This is a typical starting point for understanding disk physics.

The velocity of the gas is typically assumed to be Keplerian and circular, such that the velocity profile of the gas is uniquely determined by its distance from the central star. The equation for the velocity of the gas around the star is

$$|\vec{v}| = \sqrt{\frac{GM_\star}{r}}. \tag{2.3}$$

A more complicated geometry is illustrated in Appendix C.

2.2 Accretion

The accretion of material onto the protostar is of central importance. The initial collapse of the cloud will form a core, however the final mass of a star is not realized until material from the disk is cleared. Accretion may occur in multiple ways, typically either by magnetospheric accretion ($\sim 10^{-7}\ M_{\odot}\ yr^{-1}$, Fig. 2.2) or via a catastrophic infall event called an FU Orionis outburst ($\sim 10^{-4}\ M_{\odot}\ yr^{-1}$).

If the star has a strong enough magnetic field ($\sim kG$) which threads the circumstellar disk, material from the inner disk which is hot ($\sim 10^{3}K$) and partially ionized can travel along the magnetic field lines and be deposited on the surface of the star. Typically, the gas and plasma will be locked into a corotating orbit with the magnetic field, and from the frame of the gas, will fall ballistically onto the surface of the star, gaining velocity through gravitational acceleration. The impact on the surface of the star is violent ($\sim 10^{4}K$), producing X-ray emissions. Measurements of the funnel flow produce recombination emission of hydrogen lines, specifically Brackett γ and Balmer α in CTTSs, which have been shown to be correlated to accretion via direct measurement of the hot infrared excess in the SED (Classic T Tauri stars) (Muzerolle et al., 1998, 2003). At these accretion rates, only a small fraction of the star's final mass is accreted magnetospherically. In Herbig AeBe stars, the Balmer break is used as an accretion diagnostic (Muzerolle et al., 2004; Donehew & Brittain, 2011).

Alternatively, accretion can occur via massive accretion events called FU Orionis outbursts, named after the prototypical event. In the late 1930's, FU Orionis abruptly rose in brightness to 9.5 magnitudes from 16th magnitude (Fig. 2.3), (Hoffleit, 1939; Herbig, 1977). This was likely caused by a massive accretion event converting gravitational potential energy into kinetic energy and though interactions

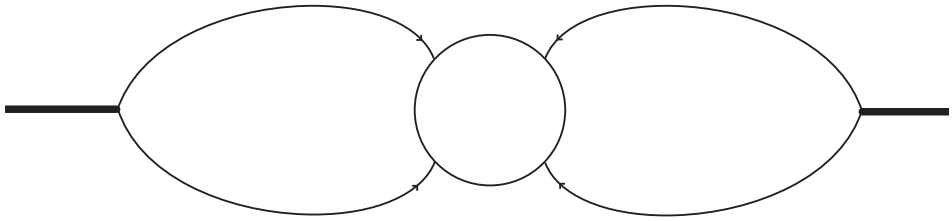

Figure 2.2 Magnetospheric accretion onto a CTTS. Field funnels material from the surface of the inner disk and allows it to fall onto the surface of the star.

between particles in the disk, infrared radiation. Because of the increase in luminosity of the source it is possible to calculate the accretion rate of the disk. Using

$$L = \eta G M \dot{M} / R \tag{2.4}$$

FU Orionis' outburst corresponds to an accretion rate $\dot{M}$ of $\sim 10^{-4}\ M_{\odot}\ yr^{-1}$. In this equation, G is the gravitational constant, M is the mass of the central star, R is the radius of the star, and η is a parameter which indicates the efficiency of the conversion of gravitational potential energy to radiation. Typically, $\eta = 0.5$. Mechanical heating (i.e. accretion) may be an important factor in establishing the warm inversion layer in the upper disk that gives rise to emission lines (Calvet et al., 1991; Glassgold et al., 2004). Accretion timescales for these events are $\sim$ 100 yr, meaning that in a typical FU Orionis outburst a star will likely accrete approximately $\sim$ 1% of its final mass. Repeated FU Orionis outbursts might be responsible for the buildup of the final mass of the star. Episodic accretion is invoked to solve the so-called Luminosity Problem, where the measured infrared flux from a sample of young stars is insufficient to explain the rate of star formation (specifically, the mass conversion

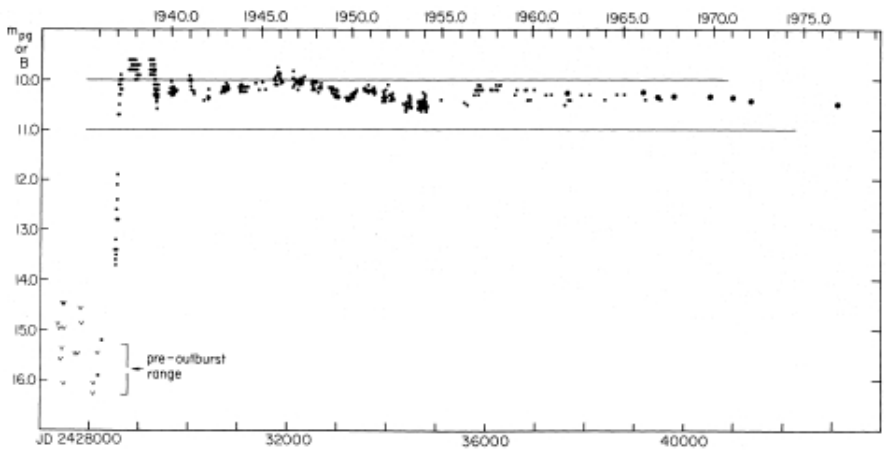

Figure 2.3 Lightcurve of FU Orionis from Herbig (1977). The abrupt rise in 1939 is evident, as well as the slow decay time of ∼decades.

from circumstellar material to stellar material) (Hartmann & Kenyon, 1996).

Chapter 3

Hydrodynamics Simulations

3.1 Background

In light of the question of the formation of planets, detailed numerical studies have been performed showing possible formation mechanisms (Mizuno et al., 1978; Mizuno, 1980; Pollack et al., 1996; Kley & Dirksen, 2006; Regály et al., 2010) of gas giant and terrestrial planets. Hydrodynamic simulations performed in this context show that a massive planet embedded in a circumstellar disk has a dramatic effect on the disk, inducing spiral density waves, clearing a large gap or inner cavity, and imparting an eccentricity to the inner cavity via Lindblad resonances. Kley & Dirksen (2006) show that these eccentricities can grow up to e=0.25 for multiple Jupiter mass planets. Fig. 3.1 shows the effects of placing a massive planet at a scaled radius of 1 unit on the circumstellar disk. A large eccentricity is generated in the disk (indicated by the white ellipse). Fig. 3.2 shows the azimuthally averaged eccentricity induced in the disk after 2500 orbits for various planet masses and positions within the disk. Most values generate some eccentricity in the disk, with smaller values being less likely to be detected. This procedure fixes the planet at its beginning radius, which

differs from our procedure (below). We follow this work with a similar study and present the results as supplemental material.

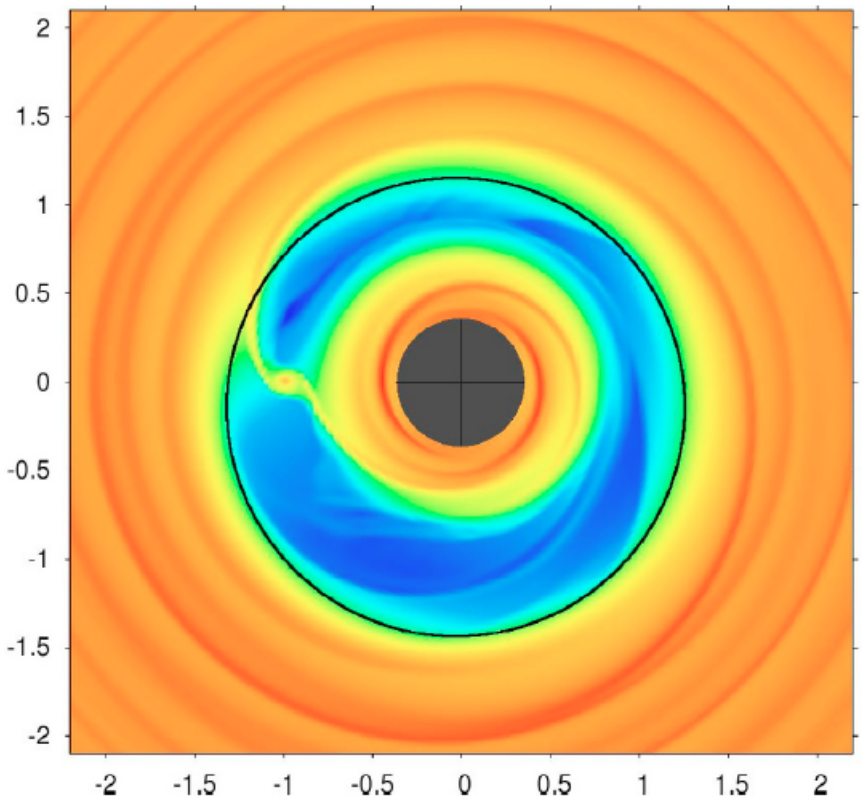

Figure 3.1 Fig. 1 from Kley & Dirksen (2006), which shows the gas density from hydrodynamic modeling of a circumstellar disk with a star and a massive planet embedded within. A large eccentricity is generated.

3.2 Physics of Hydrodynamics

The modeling above is based on the equations of hydrodynamics. These equations can be written as

$$\frac{\partial \rho}{\partial t} + \nabla \cdot (\rho \mathbf{v}) = 0 \tag{3.1}$$

$$\frac{\partial(\rho \mathbf{v})}{\partial t} = -\nabla \cdot (\rho \mathbf{v}^2 - P) \tag{3.2}$$

$$\frac{\partial E}{\partial t} = -\nabla \cdot (E\mathbf{v}) - (\frac{P}{\rho} - E)\nabla \cdot \mathbf{v} \tag{3.3}$$

which are statements describing the conservation of mass, momentum, and energy, respectively. Typically, these differential equations will be solved numerically on a grid (Eulerian or Lagrangian) and with appropriate boundary conditions, dictate the evolution of the system under study. There are multiple methods for solving these equations, however we adopt the method used in the FARGO code (Masset, 2000).

3.3 Application to HD 100546

The FARGO code (Masset, 2000) contributes to the field of star formation by providing a code which uses a novel numerical integration technique, the discussion of which is beyond the scope of this work. The main benefits to using FARGO are that it is excellently documented and is user-friendly; the tutorial guide gives an excellent description of how to run a hydrodynamic simulation of a star, circumstellar disk, and planet scenario. Output is clearly explained and an IDL visualization procedure is packaged with the distribution. We run a scenario where we attempt to emulate the HD 100546 system. The star's mass and the planet's position are set to $2.4 M_{\odot}$ and 13 AU within the scaled coordinates. For the simulation presented, we assume a planet mass of 2.4 M_{Jup}, however this value is not known, but is in line with estimates of a planet that could form in the system. The disk in the simulation is not self-gravitating, however the planet and star interact with the disk and the disk's gravity influences the planet. Fig. 3.3 shows the eccentricity gained by the planet as

a function of time. It shows that as the disk gains eccentricity, so does the planet. Multiple gas density plots are included at various time steps to show the evolution of the disk system over time. After the first time step, the disk shows accretion arms extending from the location of the planet into the inner and outer disks. As the disk evolves, the planet migrates toward the star as it loses angular momentum. This can be seen in Figs. 3.5 - 3.10.

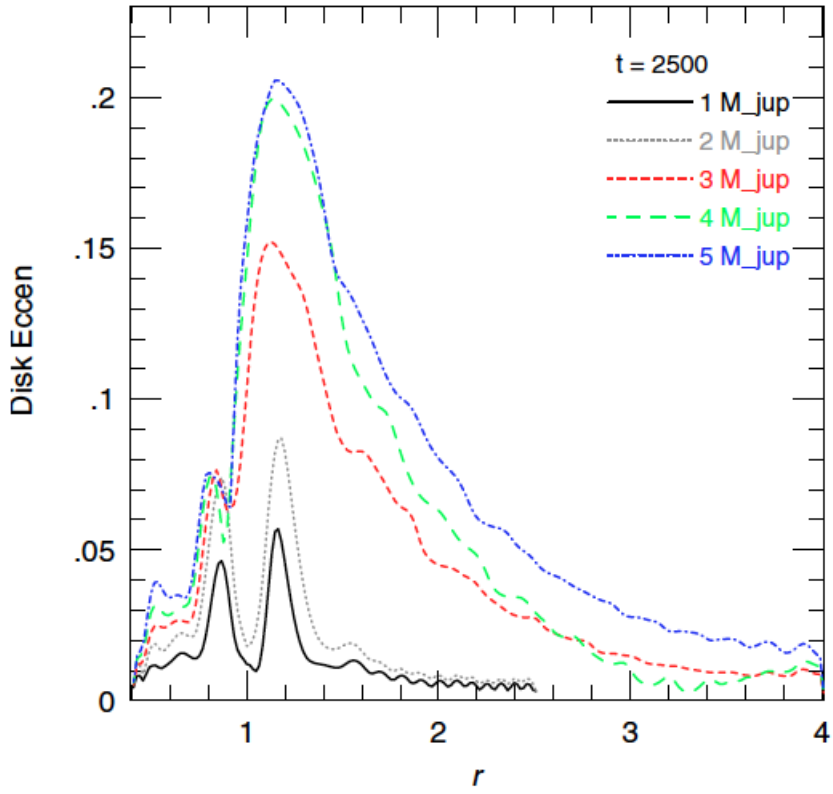

Figure 3.2 (Fig. 2 from Kley & Dirksen (2006)), which shows the results of hydrodynamic modeling of a circumstellar disk with a star and a massive planet embedded within. Eccentricities for a sample of masses and radial positions are shown. The eccentricity axis here is an azimuthally averaged eccentricity for a particular radius from the central star.

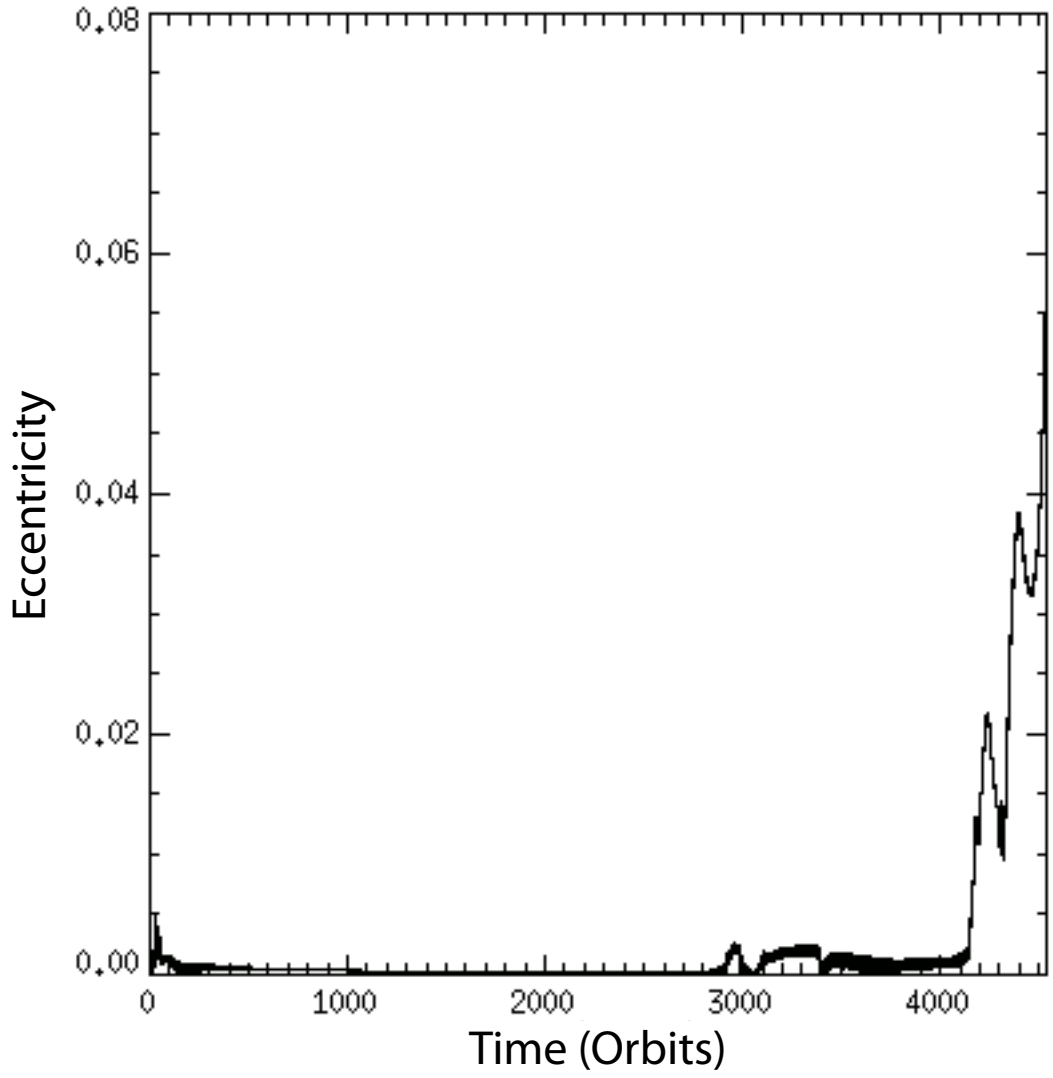

Figure 3.3 The eccentricity gained by the planet in the disk as a function of orbit number. The planet gains eccentricity over time, though the eccentricity is lower than the disk eccentricity. Created using FARGO (Masset, 2000).

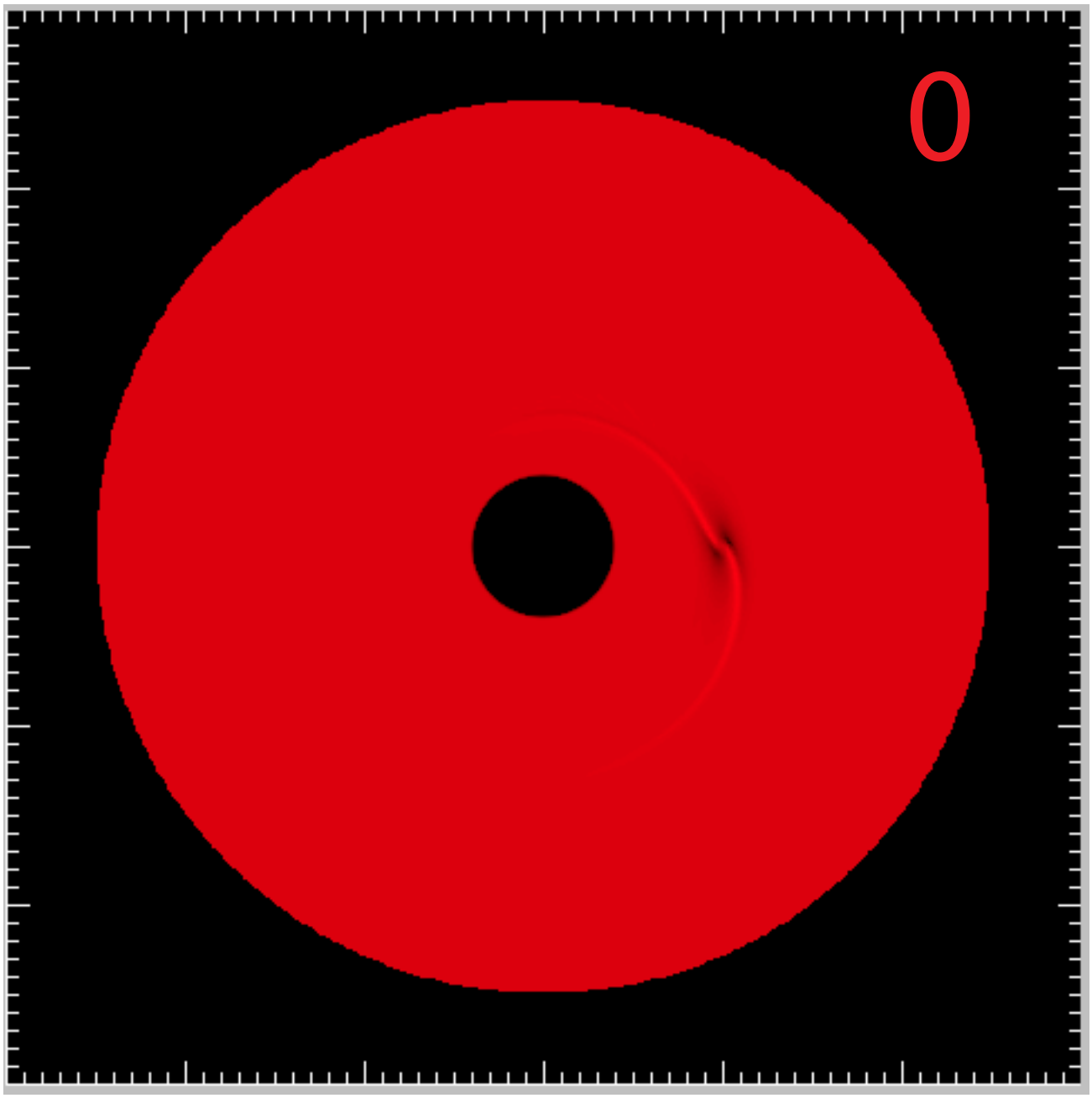

Figure 3.4 Log gas density plot after the first orbit. The spiral accretion arms onto the forming planet are already visible. The orbit number is given within the image.

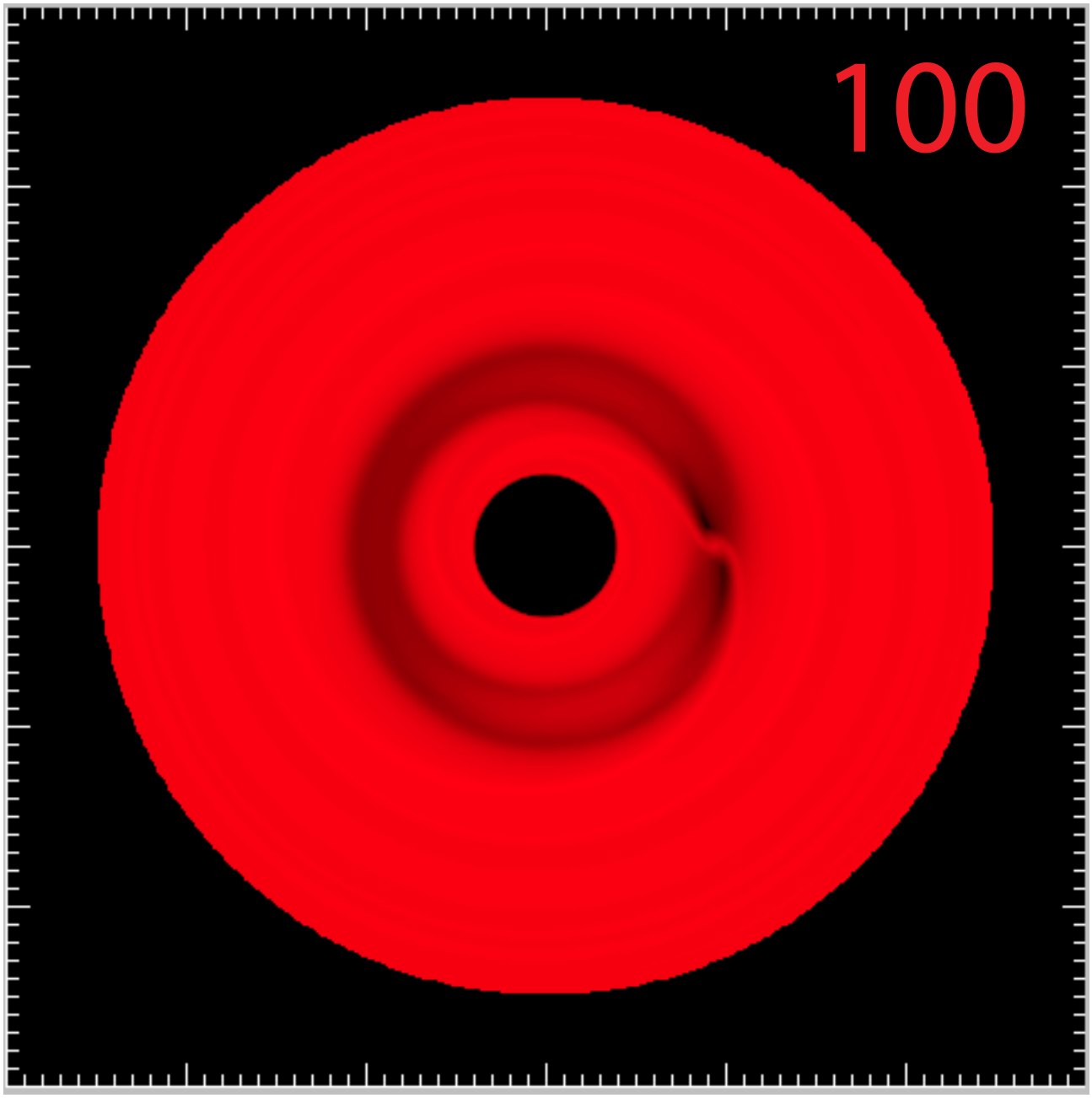

Figure 3.5 Log gas density plot after the 100th orbit. The planet has migrated slightly from its initial position. The orbit number is given within the image.

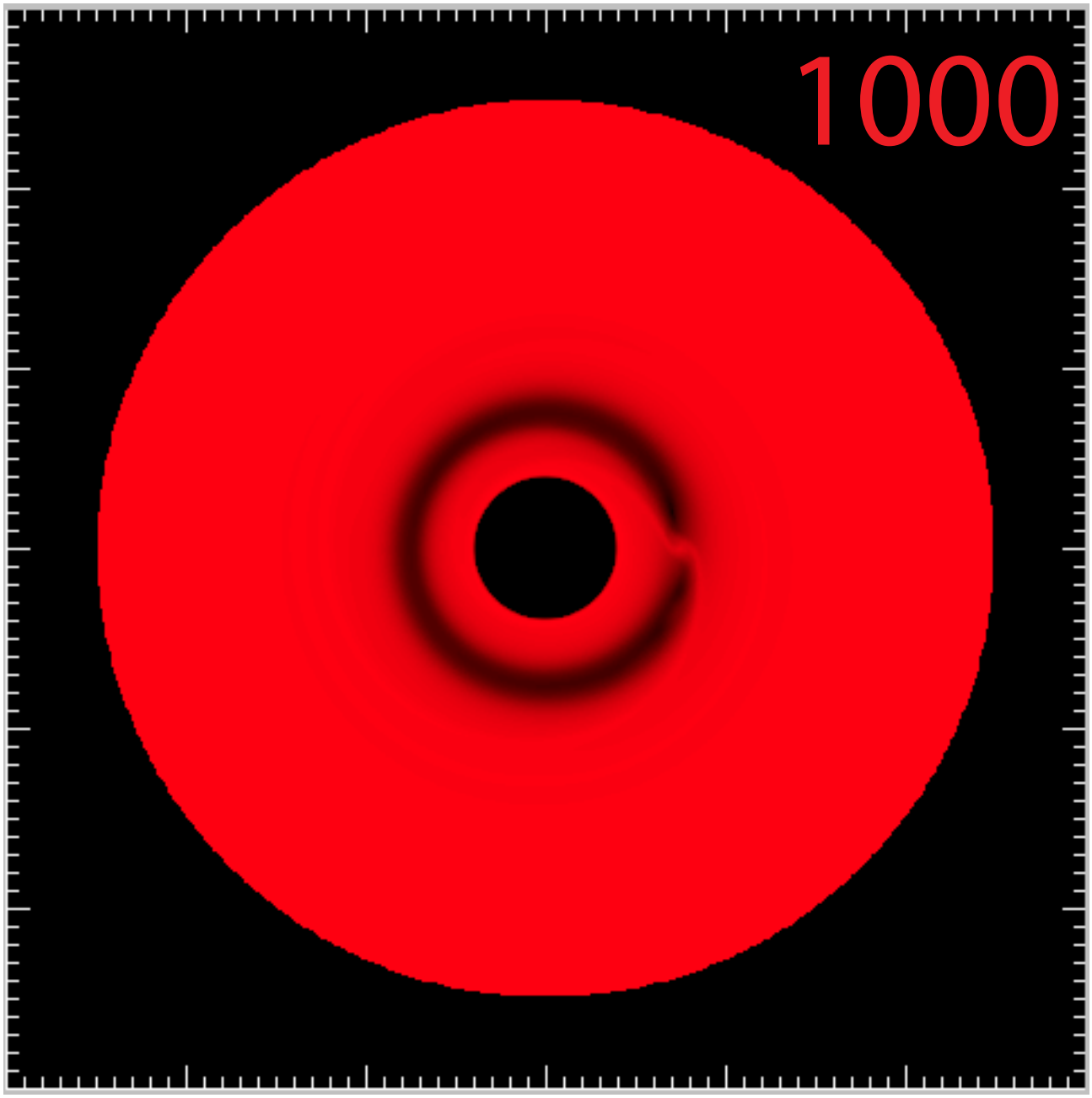

Figure 3.6 Log gas density plot after the 1000th orbit. The planet continues to migrate. The orbit number is given within the image. Large tick marks correspond to 1 scaled distance unit.

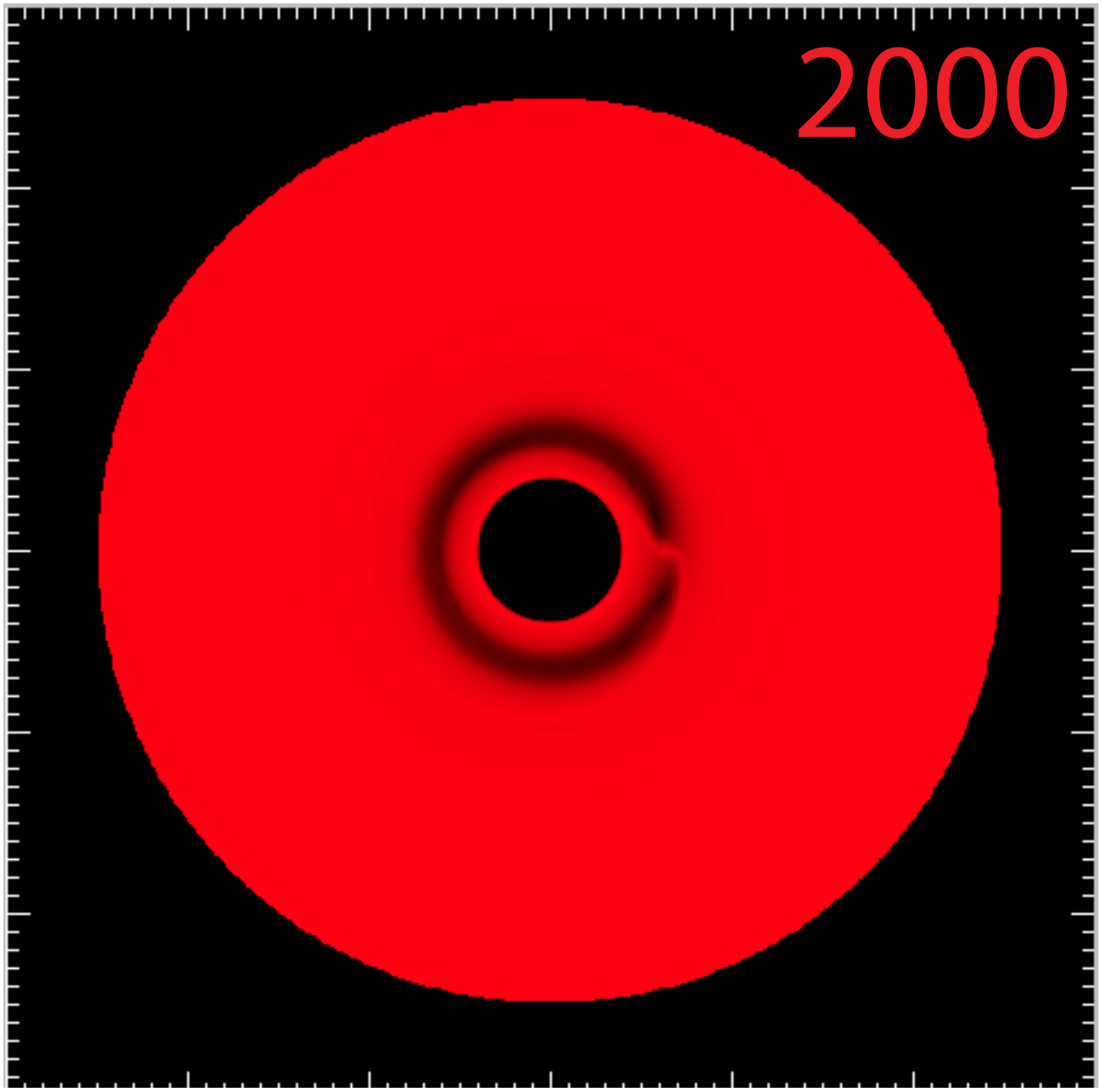

Figure 3.7 Log gas density plot after the 2000th orbit. The planet continues to migrate. The orbit number is given within the image. Large tick marks correspond to 1 scaled distance unit.

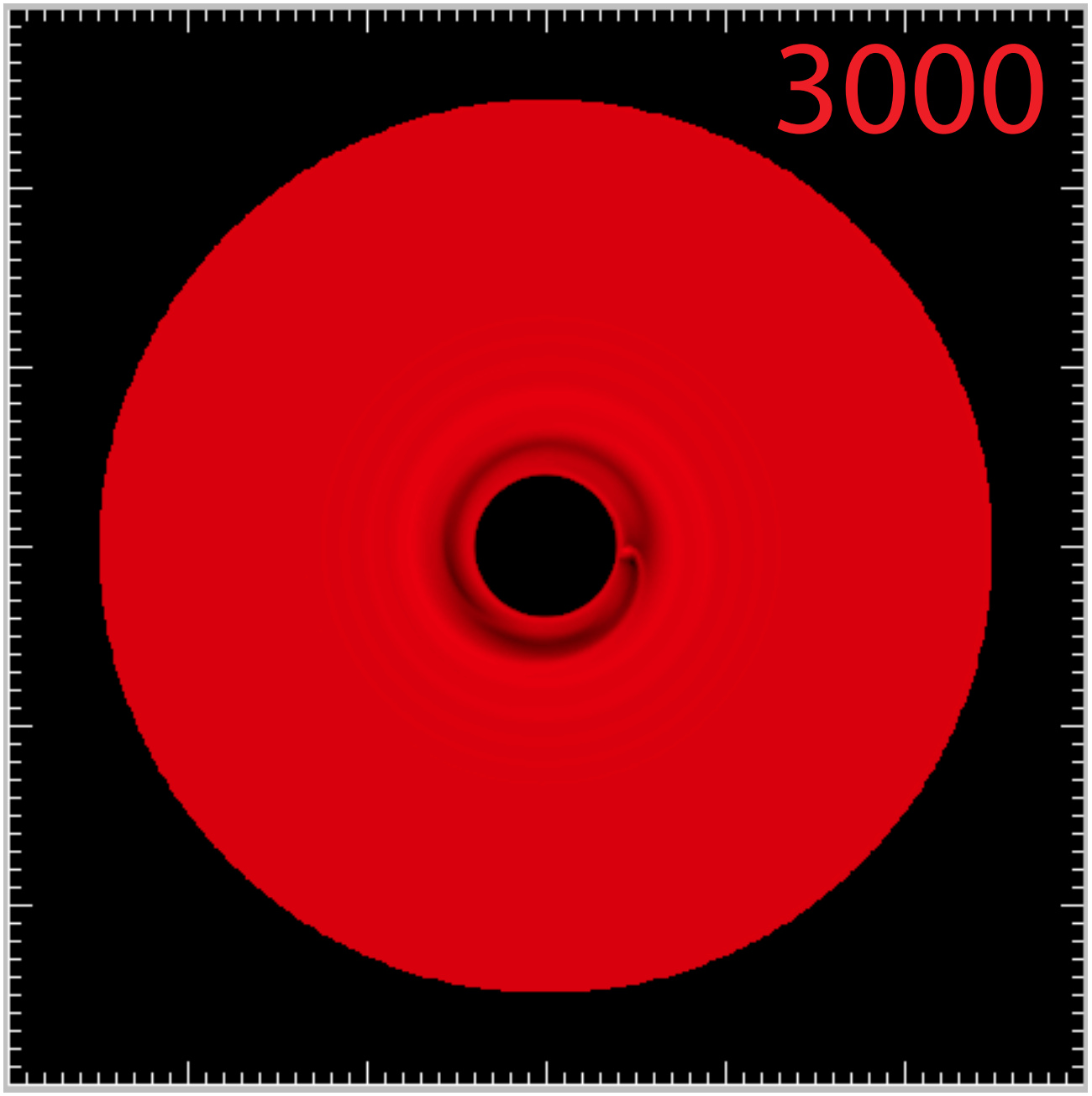

Figure 3.8 Log gas density plot after the 3000th orbit. The planet continues to migrate. The orbit number is given within the image. Large tick marks correspond to 1 scaled distance unit.

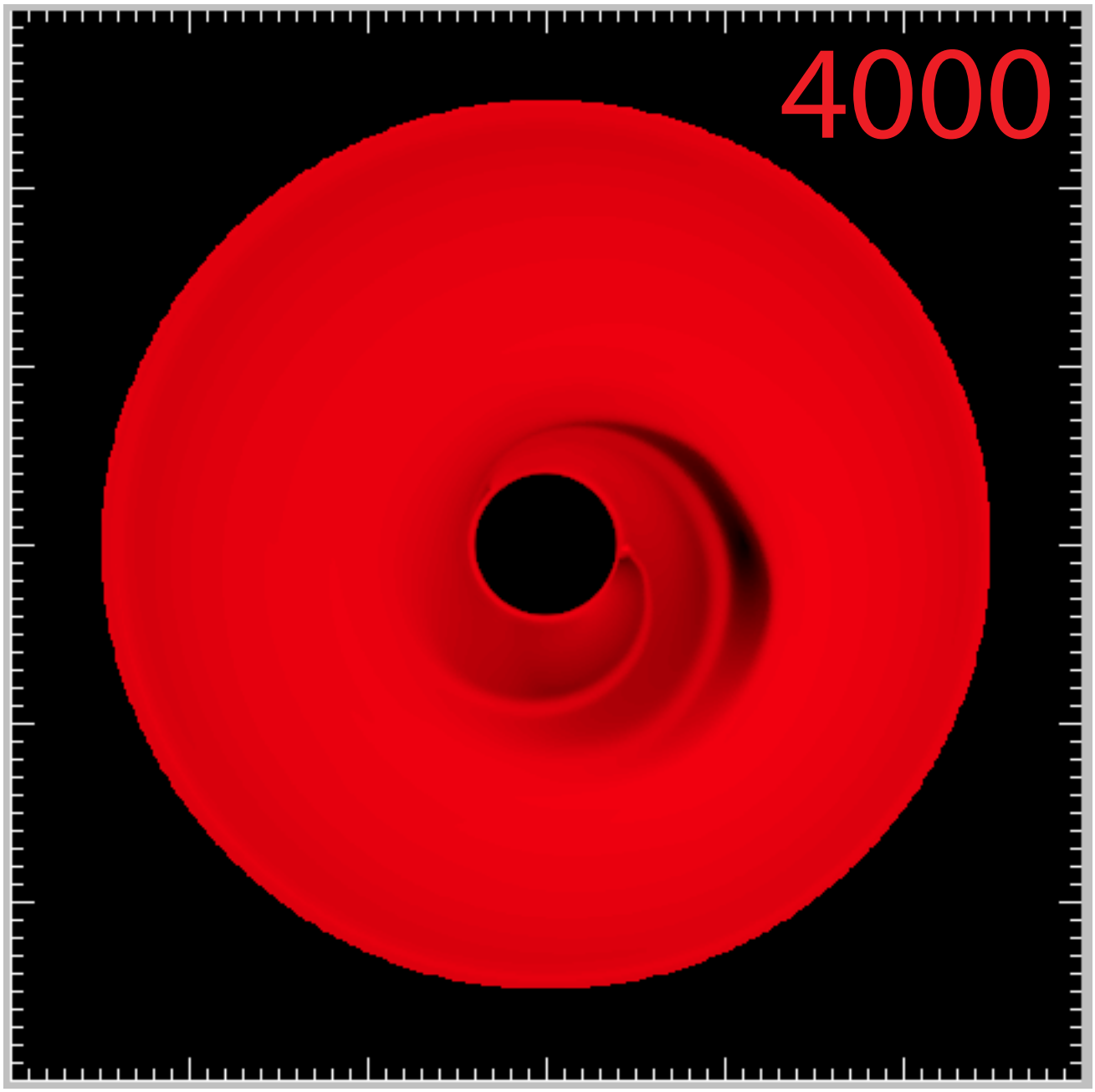

Figure 3.9 Log gas density plot after the 4000th orbit. The disk eccentricity increases and large spiral density waves become evident. The gas is now being perturbed by several Lindblad resonances, where the 1:3 resonance comes to dominate the ramping eccentricity. The orbit number is given within the image. Large tick marks correspond to 1 scaled distance unit.

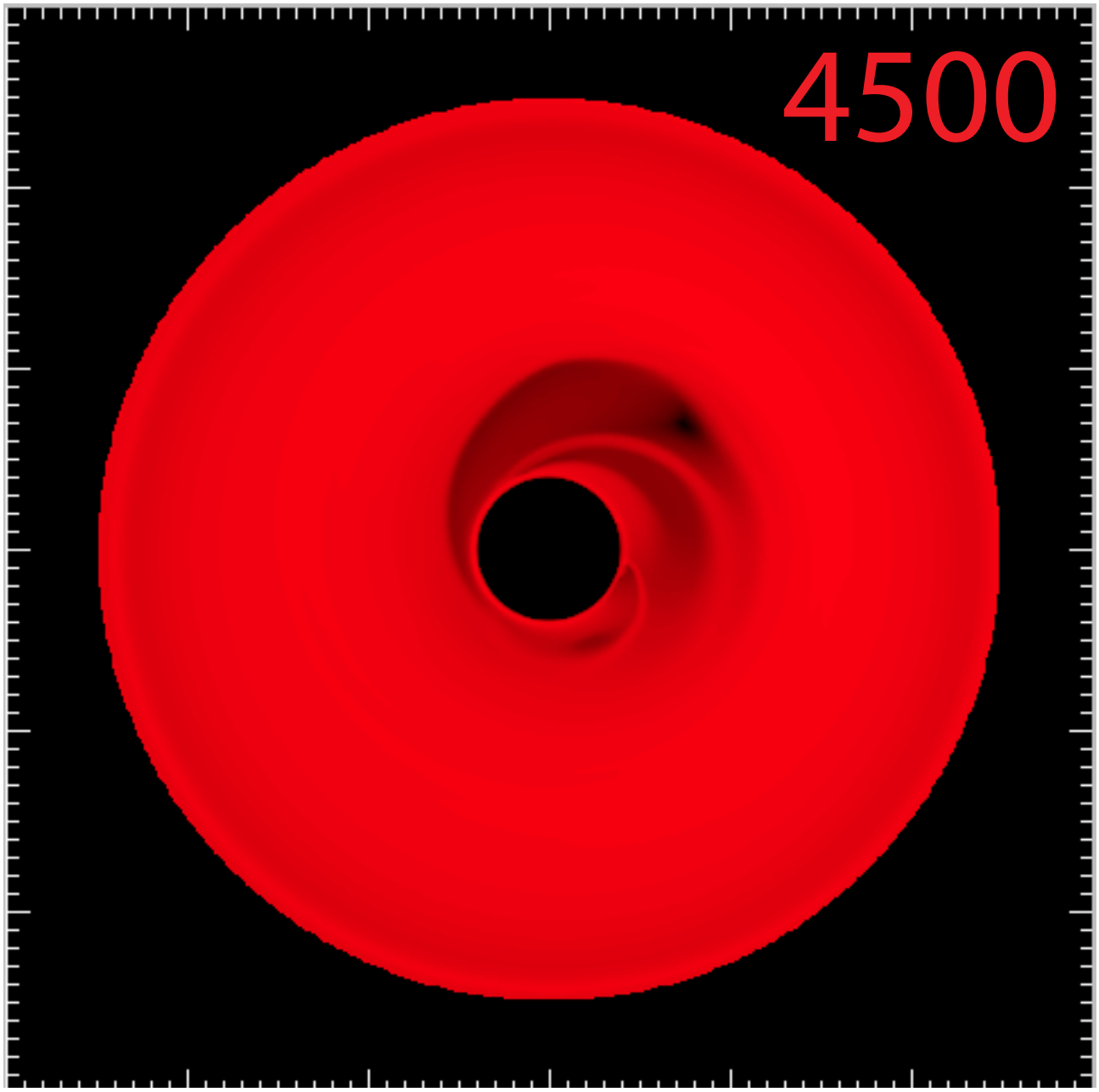

Figure 3.10 Log gas density plot after the 4500th orbit. The disk eccentricity continues to increases and large spiral density waves remain. The orbit number is given within the image. Large tick marks correspond to 1 scaled distance unit.

Chapter 4

Spectroscopy

4.1 Overview of Spectroscopy

This document presents ro-vibrational near-infrared spectroscopy of CO and OH gas. The following section describes the physics of spectroscopy and follows the logic and explicit derivations in Herzberg (1950); Bernath, Peter F. (2005).

Both CO and OH are linear diatomic molecules. OH is a slightly more complicated molecule due to the uncoupled spin of the hydrogen atom. Here I will describe the derivation of relevant quantities of the CO molecule. For a diagram, see Fig. 4.1. A linear diatomic molecule undergoes rotational transitions and vibrational transitions. The energy levels of rotational transitions can be derived by considering the Hamiltonian for a linear rigid rotor with no extraneous sources of angular momentum (spin or electron orbital):

$$\hat{H}_{rr} = \frac{\hat{J}^2}{2I} \tag{4.1}$$

where J is the semi-classical angular momentum operator in the z-basis, and I is the

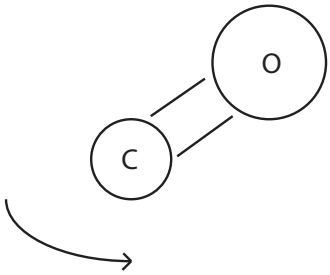

Figure 4.1 Diagram of a rigid rotor, in this case, CO. The molecule is free to rotate about its center of mass.

moment of inertia. The corresponding time independent Schrodinger equation for this Hamiltonian,

$$\frac{\hat{J}^2}{2I}\psi = E\psi, \tag{4.2}$$

can be solved for isotropic space with the spherical harmonic functions, Y_{LM}, and in this format Y_{JM}, with energy eigenvalues $\frac{\hbar^2}{2I}J(J+1)$. The moment of inertia can be written in terms of the reduced mass, μ, as $I = \mu r^2$ and reduced mass

$$\mu = \frac{m_C m_O}{m_C + m_O}, \tag{4.3}$$

for carbon monoxide. Selection rules can be obtained by considering the transition dipole moment and applying the recursion relationship for the Legendre Polynomials. The relevant selection rule for rotational transitions is $\Delta J = \pm 1$. Synthetic spectra can be calculated by assuming a population among states. Typically LTE is considered (Boltzmann distribution due to collisional excitation). See Appendix A for a brief discussion of how this can be implemented.

The selection rules give an equation to calculate the energy differences between

levels and hence the energy of transitions. The energy of a pure rotational transition is

$$\frac{E}{h} = \nu = \frac{\hbar^2}{2I}(J+1)((J+1)+1) - \frac{\hbar^2}{2I}J(J+1) = \frac{2\hbar^2}{2I}(J+1). \tag{4.4}$$

Hence, the location of each photon emitted or absorbed can be calculated using this formula. The separation between adjacent transitions is $\sim 3.8 cm^{-1}$, and typical energies for these transitions are around 20 cm^{-1}, placing them in the far-infrared.

The CO molecule, however, is not a perfectly rigid rotor. Because the molecule can stretch along its principal axis as it rotates, a centrifugal correction must be applied. Considering the forces on the molecule,

$$k(r' - r_o) = \mu\omega^2 r \tag{4.5}$$

the centrifugal force is balanced by the restoring force of the chemical bond between the C and O atoms, approximated for small deviations as arising from a Hooke potential. Here, r_o is the equilibrium length, r' the stretched length, and r is the internuclear distance (see figure 4.2).

This causes a distortion term to arise in the energy equation which is $DJ(J+1)^2$, where D is a constant of proportionality and is small in comparison to the other energy term. The new energy equation becomes

$$\frac{E}{h} = \nu = 2(B - 2D(J+1)^2)(J+1). \tag{4.6}$$

Here, $B = \frac{\hbar}{2I}$. High-precision values for B and D are 57.63596826(12) GHz and 0.18350552(46) MHz (Varberg & Evenson, 1992), though these values are for the

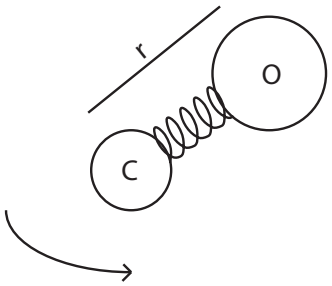

Figure 4.2 Diagram of a semirigid rotor, in this case, CO. The molecule is free to rotate about its center of mass with small oscillations along the internuclear axis.

ground electronic state of CO. Higher energy vibrational states have separate constants (See Herzberg (1950)).

The vibrational states of the molecule also affect the energy levels. Assuming the vibrational wavefunctions are decoupled from the rotational wavefunctions, we account for the vibrational energy by considering a harmonic oscillator potential along the inter-nuclear axis of the CO molecule, such that the Hamiltonian is

$$\hat{H} = \frac{p^2}{2\mu} + V(r), \tag{4.7}$$

where V(r) is the potential, which is approximated as a Dunham potential (Dunham, J.L. , 1932), or as a Morse potential. This Hamiltonian yields the energy eigenvalues for a harmonic oscillator

$$E = h\nu(v + \frac{1}{2}), v = 0, 1, 2, ... \tag{4.8}$$

which give an overall energy equation for a state in terms of v and J. The selection rules for vibrational transitions can be obtained by calculating the transition dipole moments, which yield $\Delta v = \pm 1,\ \pm 2,\ \pm 3$,... etc. Vibrational transitions can be

combined with rotational transitions to obtain so-called 'Ro-vibrational transitions'. In these cases, the selection rules for rotation and vibration apply to the transition.

The OH molecule represents a bit more of a difficulty and little experimental work has been performed on it under low density conditions present in circumstellar disks. The difficulty arises because the spin of the hydrogen's electron is not coupled to another electron, adding another angular momentum term into the total angular momentum budget. This spin couples to the angular momentum of the orbit, which splits the ground state into two states, creating a degeneracy and increasing the number of allowed levels. Furthermore, lambda-type doubling splits the rotational states (+ and -) due to the coupling of the rotation of the CO molecule and the orbital motion of the electrons. For a more complete treatment, see Schleicher & Ahearn (1982); Bernath, Peter F. (2005).

4.2 Gemini & Spectroscopy

The Gemini telescopes are two 8.19 meter telescopes separated by over 6000 miles, one in Hawaii, the other in Chile. This separation allows observations of targets in both hemispheres, with only small solid angles of the sky inaccessible. Gemini South (elevation of 2.7 km) was used to acquire the spectra reported in Chapter 5. The Gemini telescope (until recently) had a high-resolution spectrograph (Phoenix) as a visitor instrument (Hinkle et al., 2003). Phoenix is a long slit echelle spectrograph sensitive from 1-5μm. The widest slit, which is 4 pixels (.34" with the plate scale at Gemini), has a nominal resolution of 50000. While Gemini has an active optics system that constantly adjusts the focus to keep the image quality sharp, Phoenix does not work with an adaptive optics system, so our images are seeing limited, which is typically .4-.8" in the M-band.

Figure 4.3 Gemini South - The elevation is $\sim$ 2.7 km. The lack of vegetation echoes the importance of the site regarding rainfall. Courtesy of Gemini Observatory/AURA

Chapter 5

HD 100546

5.1 Background

[1]An important tool for tracing the evolution of circumstellar disks is the measurement of the spectral energy distribution (SED) of young stars (e.g. Strom et al., 1989; Hillenbrand et al., 1992; Malfait et al., 1998). The differences in the SEDs of young stars have led some to propose that they reflect an evolutionary sequence from optically thick disks to transitional disks (i.e. disks with optically thick outer disks and optically thin inner disks) to optically thin disks. A popular interpretation of transitional objects is that they reflect ongoing planet formation, but there are other processes that can also give rise to disks with transitional SEDs.

The proposed scenarios for the origin of transitional disks can be distinguished by the radial distribution of gas in the disk (Najita et al., 2007). The grain-growth and planetesimal formation scenarios predict an optically thin, gas-rich inner disk (e.g. Strom et al., 1989). A system that is forming a Jovian mass planet will show a

[1]The following chapter comes directly from Liskowsky et al. (2012). The main revisions come from changes in pagination and references to chapters within this work.

radial gap in the gaseous inner disk in the vicinity of the planet's orbit (e.g. Skrutskie et al. , 1990). Systems that have formed massive companions (>5 M_J; e.g. Lubow et al., 1999) or are being photoevaporated away (e.g. Clarke et al. , 2001) will be depleted in gas in the optically thin region of the disk. Thus, we can determine which scenario likely applies to any given transition object by probing the distribution of gas in the inner disk. As the planet-forming region of disks is generally spatially unresolved, high-resolution spectroscopy becomes a surrogate by spectrally resolving the velocity of gas. Assuming Keplerian rotation, spatial information can be extracted if the stellar mass and disk inclination are known.

Work to date that takes this approach presents conflicting results for well-known intermediate-mass transition objects such as HD 100546. HD 100546 is a nearby (d=103^{+7}_{-6} pc; van den Ancker et al., 1997) Herbig Be star with an ostensibly massive disk (M_{disk} = 0.072 $M_\odot$; Henning et al., 1998). Modeling of the SED (Bouwman et al., 2003) and imagery with the *Hubble Space Telescope* (Grady et al., 2005) indicate the presence of an inner hole in the dust distribution at 10-13 AU. While ro-vibrational CO observations of HD 100546 show that there is no CO within 13 AU of the star (Brittain et al., 2009; van der Plas et al., 2009), evidence of ongoing accretion indicates some gas persists in the inner hole (Guimarães et al., 2006).

In addition, the spectral profile of the [O I] λ6300Å line indicates that some gas extends inward to at least 0.8 AU (Acke & van den Ancker, 2006). Following the work by Storzer & Hollenbach (1998, 2000), Acke & van den Ancker (2006) suggest that the O I emission may arise from the photodissociation of OH. If this is the case, then the inner 13 AU of the disk is curiously rich in OH while depleted in CO, contrary to predictions for the chemistry of inner disks (e.g. Thi & Bik, 2005).

Rotational OH emission has been detected from the disk surrounding HD 100546, however, the spatial and spectral resolution are too low to resolve the line and thus

pinpoint the location of the gas within the disk (Sturm et al., 2010). Higher excitation ro-vibrational OH emission has been reported from other young stars: from the classical T Tauri stars AS 205A and DR Tau (Salyk et al., 2008), as well as SVS 13 (Najita et al., 2007) and V1331 Cyg (Najita et al., 2007; Doppmann et al., 2011), and several Herbig Ae/Be stars (Mandell et al., 2008; Fedele et al., 2011). Mandell et al. (2008) report P2.5 through P9.5 ro-vibrational lines of OH for two objects: AB Aur and MWC 758.

Reported below is the observation of ro-vibrational OH and CO emission from the transitional disk surrounding HD 100546 (Sec. 5.3). We compare the line profile of the OH emission to that of the ro-vibrational CO emission and the [O I] λ6300Å emission line in order to explore the properties in the region of the disk from which these emission features arise (Sec. 5.4). A detailed comparison of multi-epoch CO observations of this source is presented in a companion paper (Brittain et al., 2012) (hereafter Paper II).

5.2 Observations

High-resolution (R=50,000), near-infrared spectra of HD 100546 were acquired December 22, 2010 and December 23, 2010 using PHOENIX at the Gemini South telescope with the four pixel (0″.34) slit (Hinkle et al., 2003, 2000, 1998). A summary of observations is presented in Table 1. The position angle of the slit was 90° East of North for all observations. The spectra are centered at 3145 cm^{-1}, 2844 cm^{-1}, and 2032 cm^{-1} (Figs. 5.1, 5.2, 5.3). The PSF (point spread function) of the continuum is 0.″7. The spectral settings were selected to minimize telluric absorption of the CO and OH emission lines. The $M-$band observation includes the v=1-0 P25, P26, and P27 lines of CO as well as numerous other hot band transitions (Δ v=1, v$' \geq$ 2).

Table 1. Log of Observations

Date	Telescope/Instrument	Target	Spectral Grasp cm^{-1}	Integration minutes	S/N	Airmass
2010 Dec 22	Gemini S./PHOENIX	Theta Car	3138 - 3150	8	-	1.5
2010 Dec 22	Gemini S./PHOENIX	HD 100546	3138 - 3150	40	180	1.6
2010 Dec 23	Gemini S./PHOENIX	Theta Car	2837 - 2850	8	-	1.7
2010 Dec 23	Gemini S./PHOENIX	Theta Car	2027 - 2037.5	8	-	1.4
2010 Dec 23	Gemini S./PHOENIX	HD 100546	2837 - 2850	28	180	1.8
2010 Dec 23	Gemini S./PHOENIX	HD 100546	2027 - 2037.5	32	79	1.4

See Brittain et al. (2009) for complete line identifications. The $L-$band observations cover the $P9.5_{2^{\pm}}$, $P10.5_{1^{\pm}}$, $P15.5_{2^{\pm}}$, and $P16.5_{1^{\pm}}$ v=1-0 lines of OH.

The total rotational angular momentum of the upper state is given by the number following the P, the numerical subscript corresponds to electron spin of either $-1/2$ (1) or $+1/2$ (2), and the $+/-$ signs correspond to even/odd parity.

Unlike common diatomic molecules such as H_2 and CO, the total orbital angular moment of the ground electronic state of the OH radical is Λ=1 and is thus doubly-degenerate. The additional degrees of freedom require a somewhat more extensive labeling scheme to fully describe the transitions. In this paper, we adopt the nomenclature described by Schleicher & Ahearn (1982). Due to the interaction of the electron spin and orbital angular momentum (spin-orbit coupling), the ground electronic state is split into $^2\Pi_{\Lambda-1/2}$ and $^2\Pi_{\Lambda+1/2}$. The total angular momentum, J, is given by the sum of the molecular rotation, $N = 0, 1, 2, 3, ...$ and electron spin $s = \pm 1/2$, so that $J = N + 1/2$ in the $X^2\Pi_{3/2}$ state and $J = N - 1/2$ in the $X^2\Pi_{1/2}$ state. In addition, each rotational level is split into two states due to the coupling of the molecular rotation to the orbital motion of the electrons (lambda-type doubling); these split levels are labeled as (+) or (−) based on the parity of the level. The selection rules for a ro-vibrational transition in the ground electronic state are $\Delta J = 0, \pm 1$ and $\pm \Rightarrow \mp$.

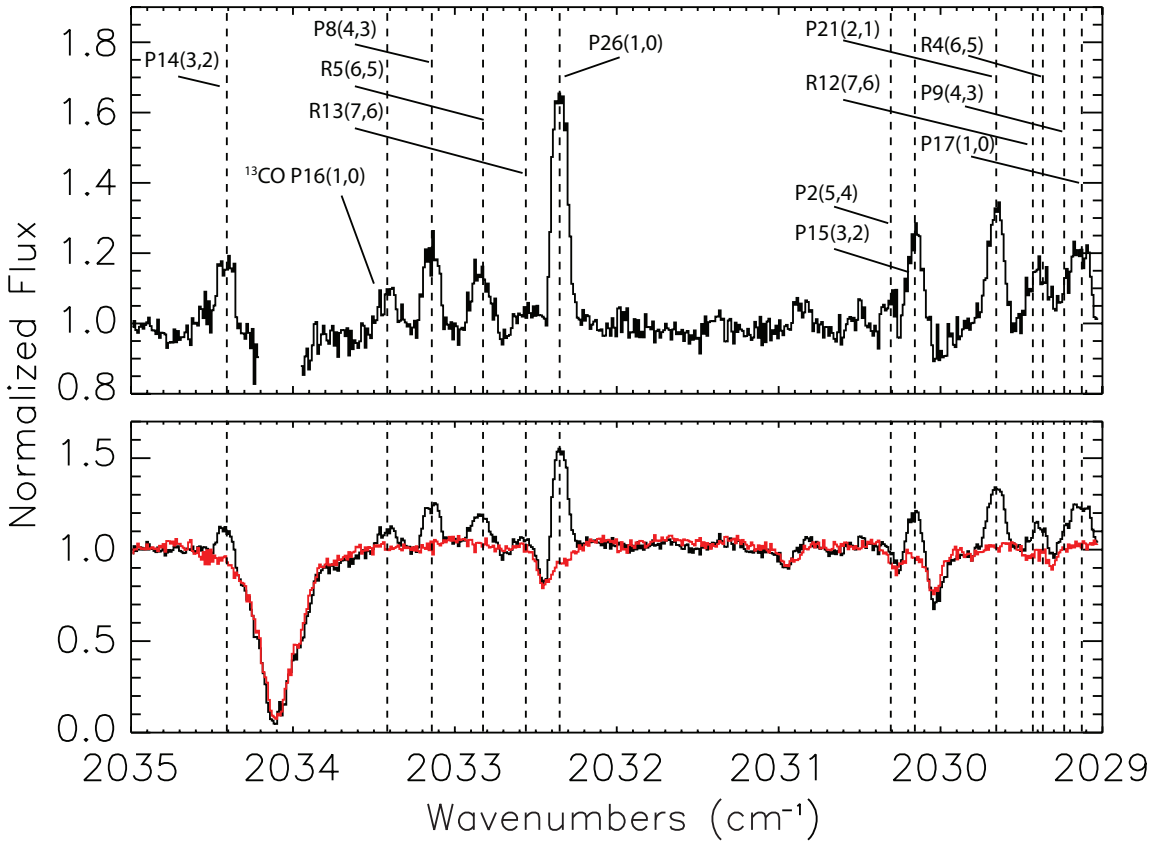

Figure 5.1 High resolution near infrared spectra of HD 100546 in the observed frame. The top panel shows the ratioed $M-$band spectra containing the ro-vibrational CO transitions. Numerous emission features are evident and are labeled. The positions of these features in this spectrum are marked by vertical dot-dashed lines. The bottom panel shows the observed spectrum for this wavelength range and the telluric standard in red. The strong emission visible in the top panel is also clearly seen here. The gaps in the spectrum are of regions where the transmittance of the atmosphere is less than 50%. The fundamental ro-vibrational CO P26 line and numerous hot band features are evident.

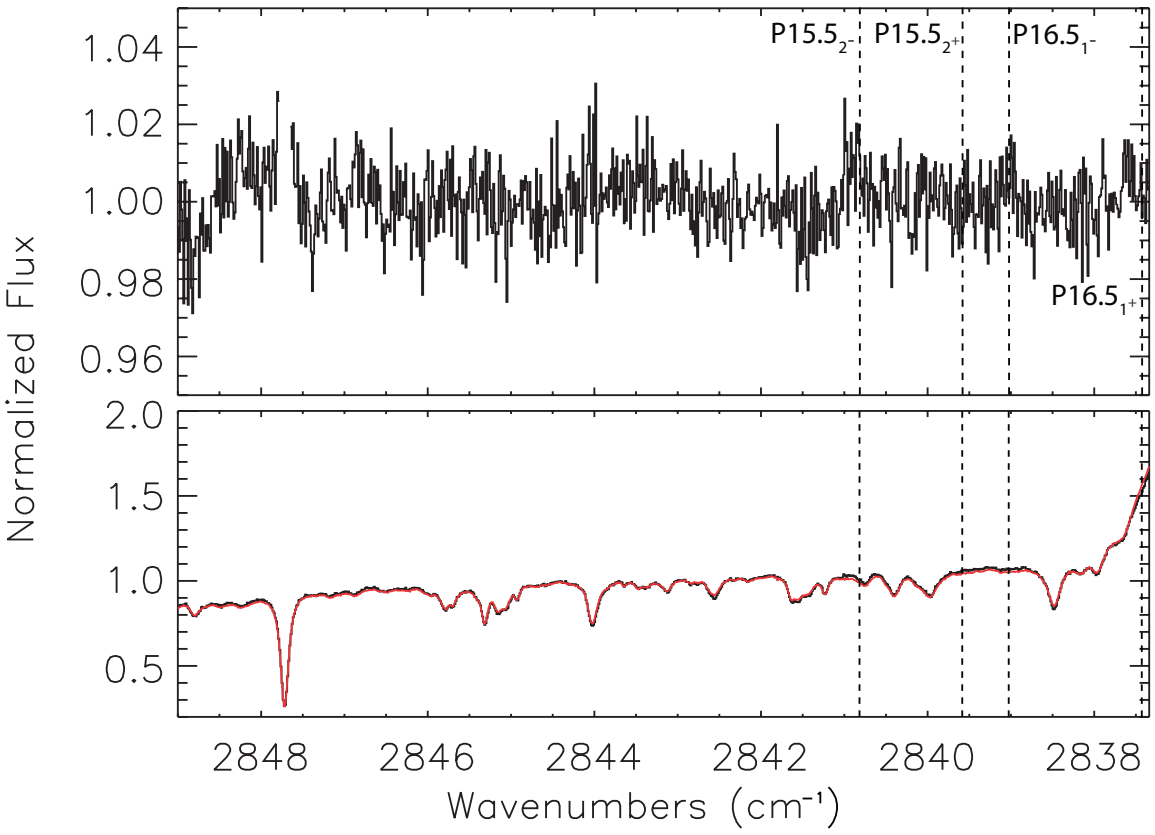

Figure 5.2 High resolution near infrared spectra of HD 100546 in the observed frame. The top panel shows the $L-$band spectra containing the ro-vibrational OH transitions while the bottom panel presents the observed spectrum (black) and the telluric standard (red). The gaps in the spectrum are of regions where the transmittance of the atmosphere is less than 50%. The positions of the v=1-0 OH lines are labeled with vertical dot-dashed lines. The P15.5$_{2\pm}$ and P16.5$_{1\pm}$ ro-vibrational emission lines are not detected. We use the noise in the continuum to set an upper limit on the equivalent widths of these lines, which are then used to put an upper limit on the rotational temperature. Detections of emission lines in this range are below the 1-σ level.

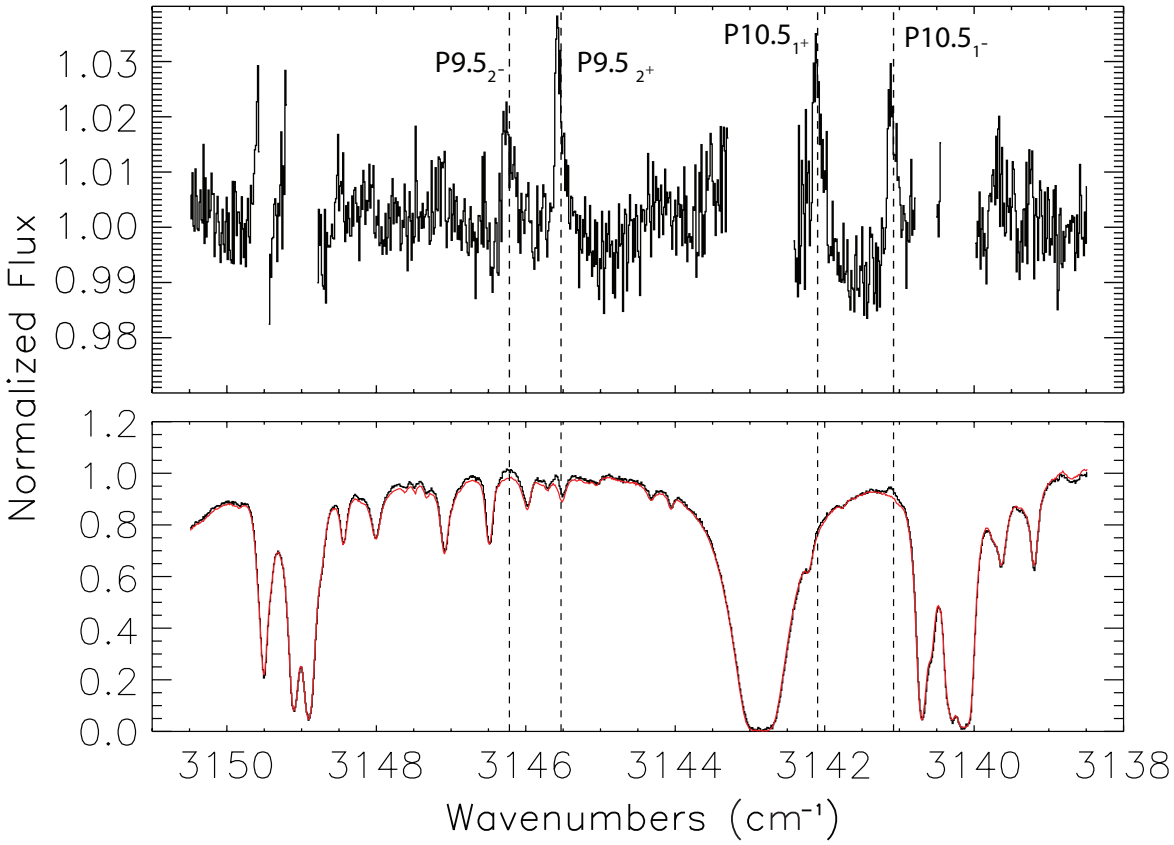

Figure 5.3 High resolution near infrared spectra of HD 100546 in the observed frame. The top panel shows the ratioed $L-$band spectrum containing the ro-vibrational OH transitions while the bottom panel presents the observed spectrum (black) and the telluric standard (red). The gaps in the spectrum are of regions where the transmittance of the atmosphere is less than 50%. The positions of the v=1-0 OH lines are labeled with vertical dot-dashed lines. The P9.5$_{2\pm}$ and P10.5$_{1\pm}$ ro-vibrational emission lines are detected and labeled with dot-dashed vertical lines.

Rotational transitions of $J'' = J'-1$, $J'' = J'$, and $J'' = J'+1$ are labeled R, Q, and P respectively. For transitions with $N+1/2$ (i.e. the $^2\Pi_{3/2}$ ladder), the rotational designation is labeled with the subscript 2. For $N-1/2$ the rotational designation is labeled with the subscript 1. When the molecule undergoes a transition between the $^2\Pi_{3/2}$ ladder to the $^2\Pi_{1/2}$ ladder, the 1 and 2 are given in the order of the transition (upper level first). The parity of the ground state is then labeled with the superscript $+$ (for even parity) or $-$ (for odd parity). The ground state electronic level is labeled X, the first excited bound electronic level A, the second excited bound electronic level B, etc. In this paper we are only concerned with ro-vibrational transitions within the ground electronic state and thus leave off the X.

Because of the thermal background in the $L-$ and $M-$ bands, the data were observed in an ABBA sequence where the telescope was nodded $5''$ between the A and B positions. The observations were combined as $(A - B - B + A)/2$ in order to cancel the sky emission to first order. Each frame was flat fielded and scrubbed for hot pixels and cosmic ray hits. The sky lines were tilted by about a pixel along the full length of the slit. The data were rectified in the spatial direction by fitting a polynomial to the centroid of the point spread function (PSF) of the continuum. The data were rectified in the spectral direction by fitting a sky emission model to each row and interpolating the wavelength solution of each row to the row in the middle of the detector. To calibrate the spectrum, we fit a telluric model to the spectrum. The model was generated by the Spectral Synthesis Program (Kunde & Maguire, 1974), which accesses the 2000HITRAN molecular database (Rothman et al., 2003). The fit to strong lines is generally accurate to within a fraction of a pixel ($\sim$1 km s^{-1}). However, near saturated lines (particularly water lines), there is a degeneracy between the width of the line and the dispersion; the latter varies across the array. The level of uncertainty in the calibration near such saturated water lines is typically at the

Table 2. Equivalent Widths of OH lines

Line	Wavenumber cm^{-1}	Equivalent Width $10^{-3}cm^{-1}$
$P9.5_{2-}$	3146.18	3.8±0.5
$P9.5_{2+}$	3145.49	4.1±0.5
$P10.5_{1+}$	3142.06	3.8±0.5
$P10.5_{1-}$	3141.04	5.3±0.5
$P15.5_{2-}$	2840.82	<.5
$P15.5_{2+}$	2839.58	<.5
$P16.5_{1+}$	2839.03	<.5
$P16.5_{1-}$	2837.43	<.5

level of a pixel (∼1.5 km s^{-1} for Phoenix). Of the four OH lines we observed, one line, $P10.5_{1+}$, was on the wing of a broad, saturated telluric water line. We shifted this line by 1 pixel blueward relative to the other three lines such that the standard deviation of the residuals between this line and the other three OH lines corresponded to the standard deviation of the noise along the continuum.

We extracted the one dimensional spectrum of the star weighted by the stellar PSF. The extraction window was 13 rows (1″.1). The spectrum of HD 100546 was ratioed with the spectrum of the standard star. Regions of the spectrum where the transmittance falls below 50% are omitted (Figs. 5.1, 5.2, 5.3). The equivalent widths of the OH lines are reported in Table 2, and a summary of the CO line positions is reported in Table 3.

Table 3. Unblended Lines

Line	Wavenumber cm^{-1}
v=3-2 P15	2030.16
v=6-5 R5	2032.83
v=4-3 P8	2033.14
v=1-0 P16 ^{13}CO	2033.42
v=3-2 P14	2034.41

5.3 Results

5.3.1 OH Temperature

We detect the v=1-0 P9.5$_{2^{\pm}}$, P10.5$_{1^{\pm}}$ OH lines (Fig. 5.3) and not the v=1-0 15.5$_{2^{\pm}}$, P16.5$_{1^{\pm}}$ lines (Fig. 5.2). We use the higher rotational lines to place an upper limit on the rotational temperature of the gas. If the gas is optically thin, the flux of an emission line is related to the column density of molecules in the upper energy state,

$$F_{ij} = \frac{hc\tilde{\nu_{ij}}A_{ij}N_i}{4\pi d^2} \tag{5.1}$$

where N_i is the number of OH molecules in the upper energy state, $hc\tilde{\nu_{ij}}$ is the energy of the emitted photon, and A_{ij} is the Einstein A coefficient. For gas in local thermodynamic equilibrium, the relative population of the energy levels is given by the Boltzmann distribution,

$$N_i = N g_i e^{-E_i/kT}/Q \tag{5.2}$$

where g_i is the statistical weight of the upper energy state, E_i is the energy of the

upper state, N is the total number of molecules, and Q is the partition function. Thus $ln(F_{ij}/hc\tilde{\nu_{ij}}A_{ij}g_i) = -E_i/kT + ln(N/4\pi d^2 Q)$ so that the rotational temperature is given by the negative reciprocal of the slope of a linear least squares fit of $ln(F_{ij}/hc\tilde{\nu_{ij}}A_{ij}g_i)$ and E_i/kT. Since we only detect the P9.5$_{2^{\pm}}$, P10.5$_{1^{\pm}}$ lines we can only place an upper limit on the rotational temperature of the gas. We fit the detected lines and the 1σ upper limit of the non-detected lines and find that T_{rot} <1400K (Fig. 5.4). This upper limit is consistent with the range of CO rotational temperatures at the inner edge of the disk (T = 1400 $\pm$400 K; Brittain et al., 2009). As the critical densities for rotational excitation of the levels we observe are high, it is possible that the OH is not rotationally thermalized. However, it seems likely that a disk environment that is dense enough to thermally populate the $v = 1$ vibrational state of CO (Brittain et al., 2009) would be dense enough to populate the rotational states of OH.

5.3.2 Comparison of HWZI of CO, OH, and OI

We previously reported the January 2006 detection of ro-vibrational CO emission from HD 100546 (Brittain et al., 2009). In our earlier report, we showed that the gas is excited by a combination of UV fluorescence and collisional excitation and that the emitting region extends from 13 AU to at least 100 AU. In data acquired five years later, which are presented here, we find that the equivalent width of the fundamental CO emission lines increased by 50% whereas the average equivalent width of the hot band lines increased by 30% (Paper II). We also find that while the line profile of the hot band CO emission lines remained constant, the line profile of the v=1-0 emission lines varied. In the present epoch, the v=1-0 CO P26 line profile is symmetric, whereas the majority of the luminosity in the hot band CO lines is on the blue side of the lines.

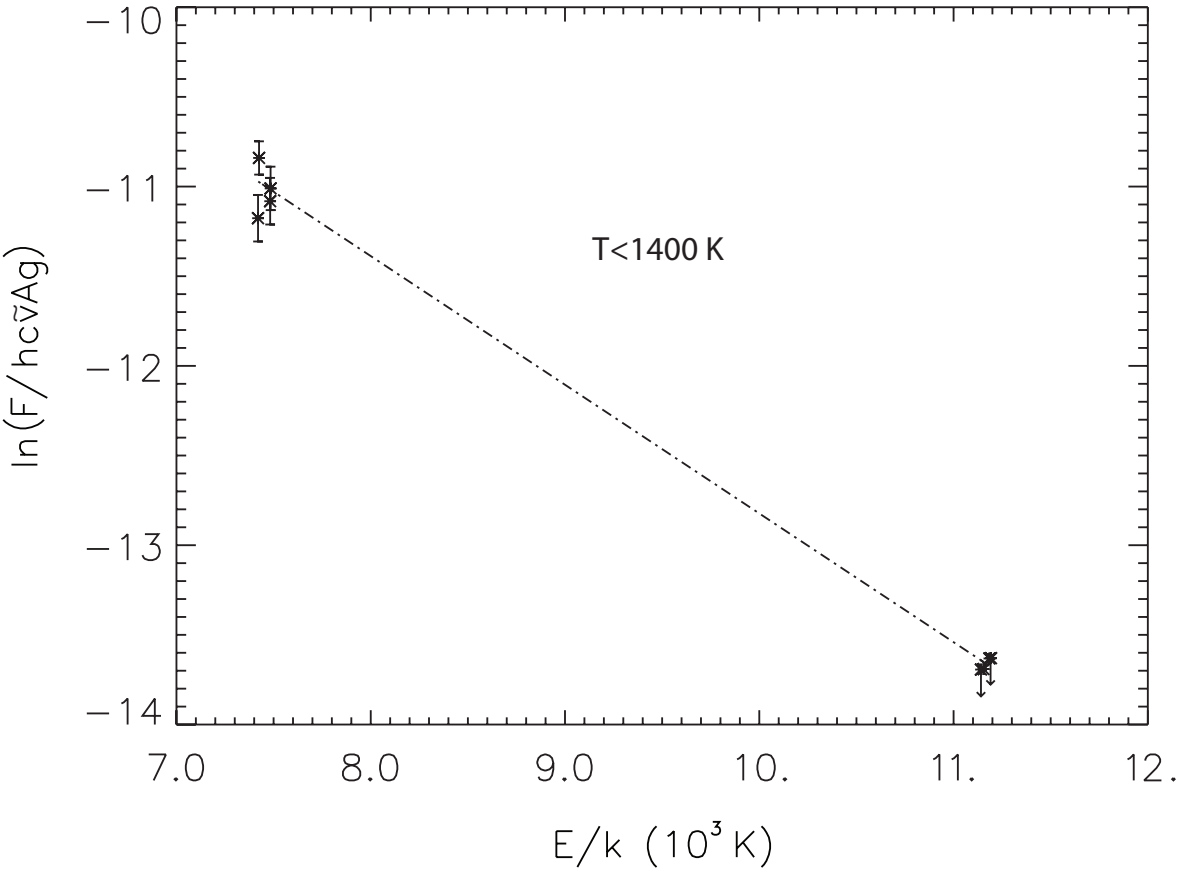

Figure 5.4 Excitation diagram of ro-vibrational OH emission lines. The quantity $\ln(F/hc\tilde{\nu}Ag)$ is plotted against E/k, the energy of the upper level, where F is the line flux (in erg/s/cm^2/cm^{-1}), $\tilde{\nu}$ is the wavenumber of the transition (in cm^{-1}), g is the multiplicity of the upper level, and A is the Einstein A coefficient of the transition. Thus the rotational temperature of the gas is given by the negative reciprocal of the slope. The solid line shows the fit to the detected values and the upper limits. The 1σ upper limit on the rotational temperature of the OH gas, based on the best fit line, is 1400 K.

A detailed study of multi-epoch CO observations is presented in Paper II. In that paper we show that over three epochs spanning 2003-2010 the spectral line profile and equivalent widths of the v=1-0 CO lines vary; the equivalent widths of the hot band lines are less variable and their spectral line profile remains constant. Because variations in the M-band continuum can account for the modest variations in the equivalent width of the hot band lines, we assume that the hot band lines are approximately constant in flux, and that the v=1-0 lines vary more dramatically. In this paper we restrict our comparison of the OH and CO line profiles to data taken contemporaneously, and we focus on the hot band CO lines because they are less variable.

Because the individual OH lines are of low signal to noise (a result of their low equivalent width) we constructed an average profile of the unblended OH lines in order to facilitate the comparison of the OH, CO, and [O I] λ6300Å line profiles (Fig. 5.5 and Fig. 5.6).

The full width at zero intensity (FWZI) of the OH emission is 24 km s^{-1} (Fig. 5.7) and is consistent with the CO emission (Fig. 5.8). The [O I] λ6300Å emission line (Fig. 5.7) has a FWZI of 90 km s^{-1}. While the O I extends to about 0.8 AU (Acke et al., 2005), the inner extent of the OH is consistent with that of the CO which is truncated at 13 $\pm$6 AU (Brittain et al., 2009).

The profiles of the OH lines differ from the profiles of the hot band CO lines. Inspection of the average CO line profile reveals a modest asymmetry where the emission peaks on red side of the line, though the blue side contains the majority of the flux. This is similar to what was observed in 2006 (Brittain et al., 2009). The OH line profile is also resolved and asymmetric (Figs. 5.5, 5.7, 5.8). The flux ratio of the blue side of the OH line to the red side of the OH line is $\sim$4.

We determine the Doppler shift of these asymmetric lines by fitting our model

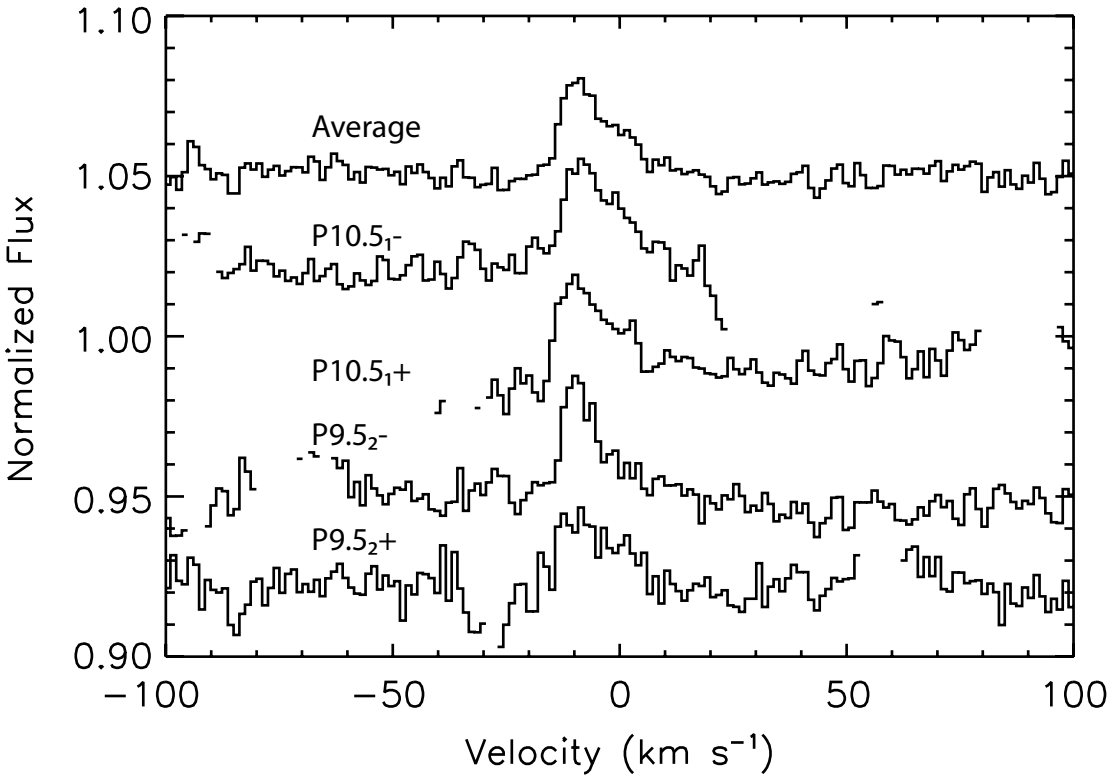

Figure 5.5 Individual OH lines used to construct the average OH line profile in the rest frame of the star. The S/N of the average continuum is ∼325. The average OH line to continuum ratio is ∼ 3% and the continuum noise is ∼ 0.6%. The HWZI is 12 ±2 km s^{-1}. The asymmetric line shape is evident in most of the individual lines, with approximately 80% of the emission in the blue and 20% in the red. The P10.5$_{1+}$ line was shifted 1.5 km s^{-1} blueward to line up with the other OH lines such that residuals between the P10.5$_{1+}$ line and the other OH lines corresponded to the noise along the noise along the continuum.

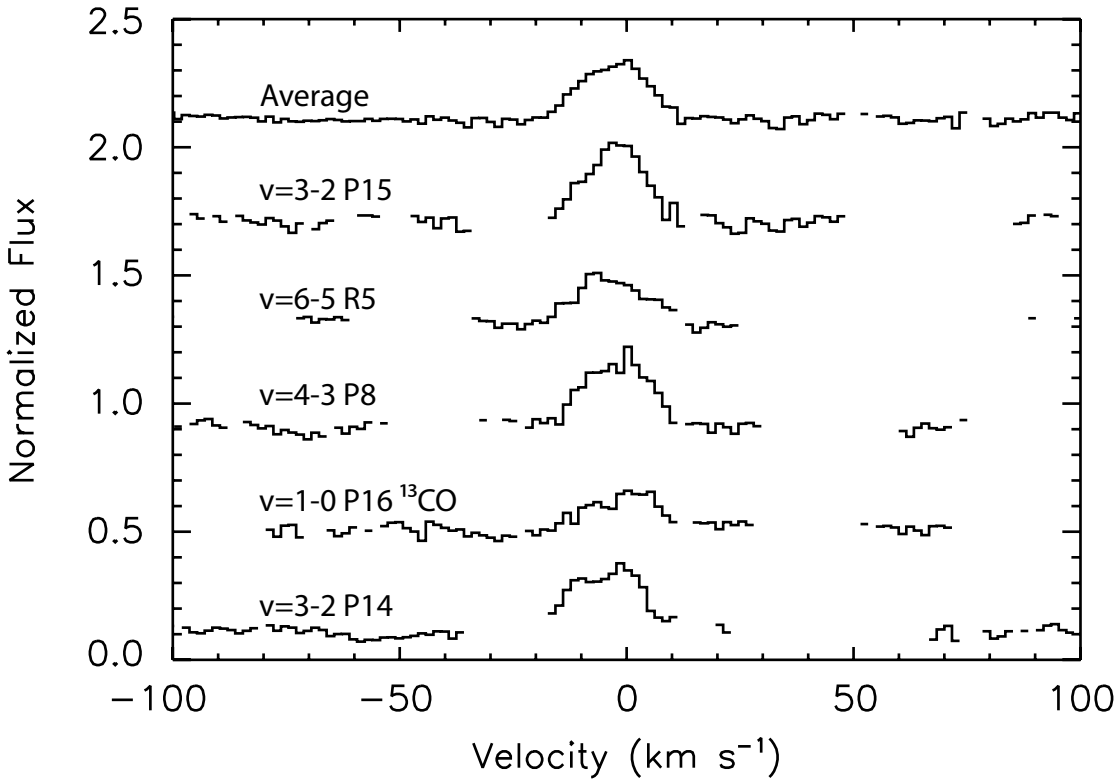

Figure 5.6 Unblended hot band CO lines in the rest frame of the star. The signal to noise of the continuum of the average profile is ∼110. The HWZI of the line is 13 ±2 km s^{-1}. Line positions are reported in Table 3.

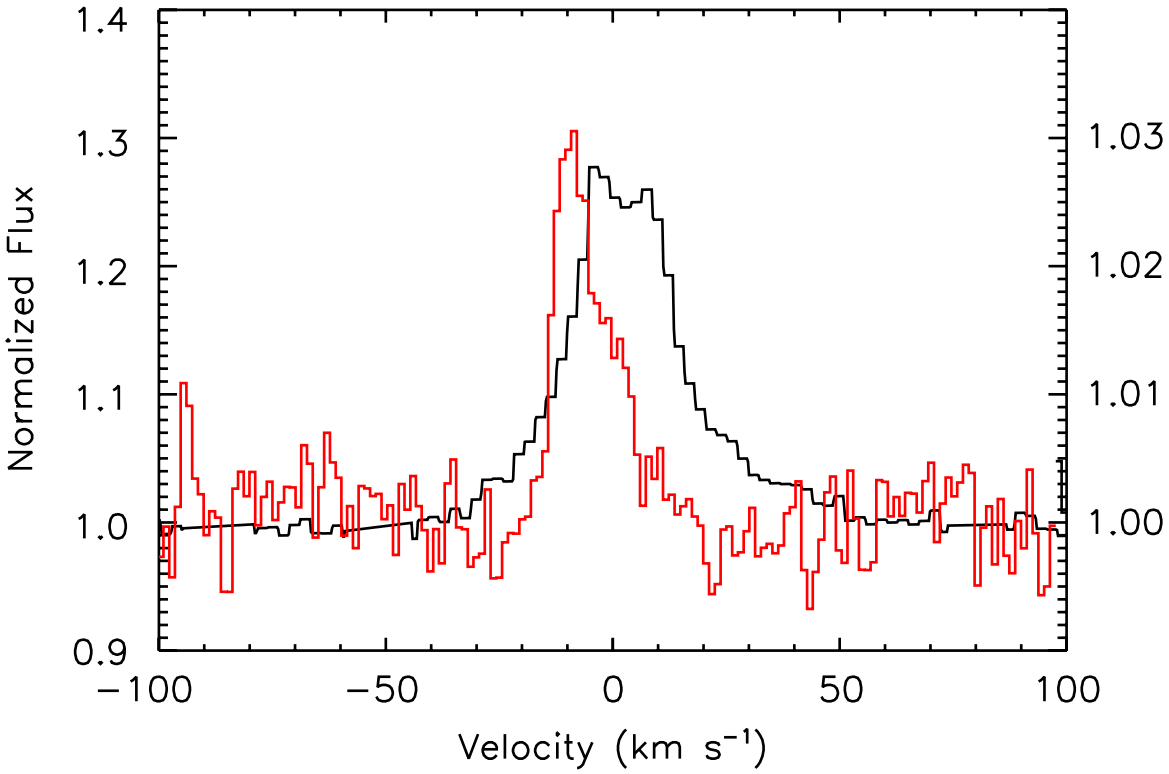

Figure 5.7 Comparison of the [O I] λ6300Å line and the average OH line profile (adapted from Acke et al. (2005)) in the rest frame of the star. The scale of the [O I] λ6300Å line (black) is the left vertical axis. The scale of the OH emission line (red) is denoted on the right vertical axis. The line profiles are clearly different, and the HWZI velocity of the OH emission is much narrower than that of the O I line indicating that it does not arise from the same region of the disk as the OH emission.

to the data. The barycentric Doppler shift is +16 km s^{-1}. This is similar to the radial velocity we infer from submillimeter observations of CO ($\sim$14 km s^{-1}; Panić et al., 2010). It is also similar to the value inferred by observation of the [O I] λ6300Å line ($\sim$18 km s^{-1}; Acke et al., 2005).

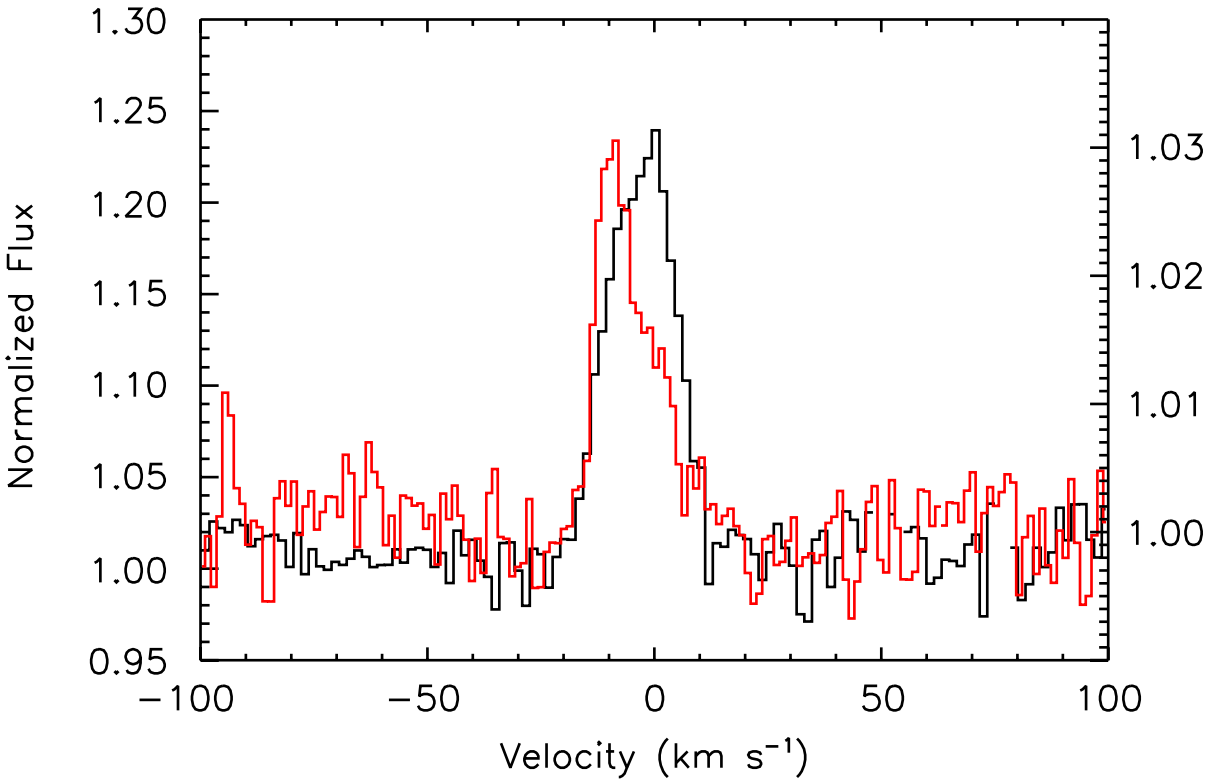

Figure 5.8 Comparison of the average hot band CO line profile (black) and the average OH line profile (red) in the rest frame of the star. The scale of each emission line profile is plotted in the left axis. The line profiles are clearly different, but the width of each line is consistent.

5.3.3 Origins of the Asymmetry

We consider four possibilities for the origin of the asymmetry seen in the average OH line. First, a wind may generate the blue-shifted asymmetry seen in the OH line. Pascucci & Sterzik (2009) show that the [Ne II] 12.81 μm emission in multiple T Tauri stars has a blue-shifted centroid of approximately a few km s^{-1} and a slight blue excess that they attribute to a disk wind. One difference between the [Ne II] emission and the OH line profile studied here is that the [Ne II] line profiles are marginally asymmetric, whereas our OH line profile is dramatically so.

Molecular line profiles indicative of disk winds have also been reported, although the line profiles are also much more symmetric than our OH line profile. In their study of CO emission from T Tauri stars, Bast et al. (2011) reported symmetric CO line profiles with a narrow peak and broad wings for a subset of the sources they studied. The spatial constraints on the emission led the authors to conclude that the emission likely arises from a combination of emission from a circumstellar disk and a slow-moving disk wind. Detailed modeling by Pontoppidan et al. (2011) shows that such a combination can produce a reasonable fit to the observed line profiles and their spectroastrometric properties. Additionally, NIR emission from organic molecules has been detected for several T Tauri stars, with line profiles similar to that found for the CO emission, suggesting a similar origin (Mandell et al. 2012). For systems with large disk inclinations like that in HD 100546, self-absorption is expected if the wind component is strong, which is not seen in HD 100546 (i=45°). Ro-vibrational CO emission lines forming in outflowing material of V1647 Ori have also been observed, but these have a P Cygni profile and a symmetric emission component (Brittain et al., 2007), a different line profile from that of the OH in HD 100546. While we cannot rule out that the ro-vibrational OH lines we observe form in a disk wind that gives rise

to a blue-shifted excess, our profile is distinct from the other profiles in the literature attributed to a disk wind.

Second, transonic turbulence in the disk (e.g., driven by the magneto-rotational instability) produces spatial inhomogeneities in the temperature and density distribution of the disk. If they are large, such inhomogeneities might produce an OH line profile as asymmetric as observed. Simulations by Fromang & Nelson (2006) find 1σ fluctuations from the mean density of $\sim$10%. A much larger fluctuation is likely necessary to produce the level of asymmetry that we observe. An additional potential difficulty with this picture is that we observe a much more dramatic asymmetry in the OH line profile than the CO profile. Could both profiles arise from the same turbulent disk? If the critical densities of CO and OH for ro-vibrational excitation differ significantly, their sensitivity to inhomogeneities might be more pronounced for one molecule than the other. This picture could be tested with future observations. If the asymmetry originates from turbulence in the disk, the OH line profile would be expected to show stochastic line profile variations, and we would not continue to see the profile that we now observe.

Third, a localized hot-spot or a dense lump of material could induce non-axisymmetric emission. Such a hot-spot in the disk could be caused by a planet/disk interaction if the planet warms the inner rim in its vicinity. If this is the case, then the profile of the line should vary with the orbital phase of the companion.

Finally, hydrodynamic modeling indicates that a gas giant planet in a circumstellar disk can induce an eccentricity as high as 0.25 in the inner rim that falls off as $\sim r^{-2}$ Kley & Dirksen (2006). The modeling also predicts that the semi-major axis of the eccentric disk precesses slowly ($\sim$10°/1000 orbits). Thus the OH line profiles should show minimal variation over the orbital period of the planet. To determine whether an eccentric inner rim can account for the observed asymmetry, we model

the hot band CO and OH emission line profiles assuming that the inner wall has a nonzero eccentricity while the outer disk is circular.

5.4 Modeling

In our model, we adopt the disk geometry described by Brittain et al. (2009). The inner rim is puffed up (Dullemond et al., 2001) with a scale height of 3.5AU (Bouwman et al., 2003; Brittain et al., 2009; Benisty et al., 2010). We adopt the inner radius found from the synthesis of the ro-vibrational CO emission (13 AU; Brittain et al., 2009) and the same radial profile for the disk emission found from our previous modeling ($\sim$R$^{-1/2}$). We use a stellar mass of 2.4 $M_{\odot}$ (van den Ancker et al., 1997), and an inclination of 45°, a value within the bounds measured by Quanz et al. (2011) ($47° \pm 2.7°$) and Ardila et al. (2007) ($42° \pm 5°$). See Appendix C for a description and derivation of the geometry and velocity field.

The magnitude of the bulk velocity of a parcel of gas in an eccentric orbit is not axisymmetric and is given by $v(\theta)^2 = GM_{\star}(1 + e^2 + 2ecos(\theta))/(a(1 - e^2))$, where G is the universal gravitational constant, $M_{\star}$ is the stellar mass, a is the semi-major axis of the eccentric annulus, e is the eccentricity, and θ is the phase of the orbit measured from periastron. For non-zero eccentricities, the velocity of the gas at periastron is larger than at apastron, so the side of the line profile arising from gas near periastron will extend to higher velocities (Fig. 9). Additionally, the gas in the disk near periastron is closer to the star making that gas warmer and brighter. We assume the temperature scales as $T = T_0(R/R_0)^{\alpha}$ and the luminosity of the line is proportional to $B_{\tilde{\nu}}(1 - e^{-\tau_{\tilde{\nu}}})$. Fig. 5.9 shows the effect of increasing eccentricity on a line profile. The synthetic emission line profiles shown arise from an eccentric, unresolved annulus inclined by 45°with $\alpha = -1$. For a more complete discussion of

the generation of the asymmetric lines, see Appendix D.

In modeling the line profiles, we assume the line of sight falls along the semi-minor axis of the disk and the slit is aligned with the semi-major axis of the disk.[2] Such an orientation maximizes the difference between the projected velocity on the red-shifted and blue-shifted sides of the disk. If the line of sight falls along the semi-major axis, this results in the gas at apastron and periastron having a zero projected velocity and a symmetric line. Thus the eccentricity inferred from our modeling is a lower limit.

For the line profile calculation, the disk is divided into annuli, and each annulus is then further divided azimuthally into zones, with each representing a change in the projected velocity (along the line of sight) of 1 km s^{-1}. We assume that the inner wall has an eccentricity that is left as a free parameter. The surface of the disk is comprised of annuli with an eccentricity of zero. In the expression for the radial temperature variation, $T = T_0(R/R_0)^{\alpha}$, the fiducial temperature T_o is assumed to be 1400 K based on what was observed for CO. The contribution to the luminosity of the emission lines from each zone is proportional to the area of the zone and $B_{\tilde{\nu}}(1-e^{-\tau_{\tilde{\nu}}})$. The emergent spectrum is then calculated by looping over all the zones and shifting the luminosity arising from each zone by the projected velocity. The spectrum is then convolved with the instrument profile, scaled to the flux of the OH feature, and resampled into a common velocity space. We leave the radial dependence on temperature (and thus the luminosity) of the OH emission in the inner rim a free parameter.

The fraction of the emission that arises from the inner wall of the disk is also left as a free parameter for the OH and CO distributions. We achieve the best fit if

[2]The position angle of a disk is defined by the apparent semi-major axis of the inclined disk. The apparent semi-major axis is not generally aligned with the intrinsic semi-major axis of the eccentric disk. In this paper the semi-major and semi-minor axes refer to intrinsic axes of the disk not the apparent axes.

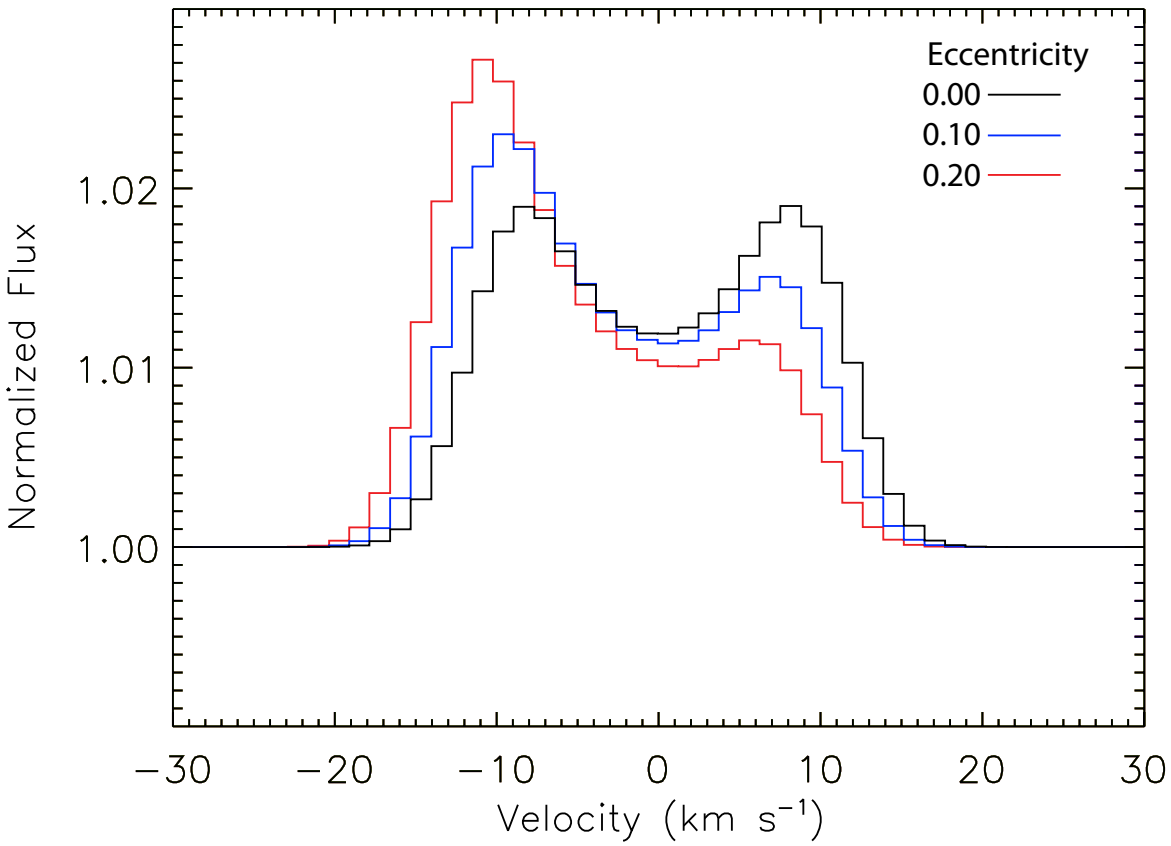

Figure 5.9 Synthetic, spatially unresolved line profiles of emission from an eccentric inner wall that is inclined by 45°to the line-of-sight in the rest frame of the star. The other model parameters are α = -1, an radius for the inner wall of 13 AU, and a stellar mass of $2.4 M_{\odot}$ (see text for details). The emission is entirely from the wall component in this example to best illustrate the asymmetry, which grows as we increase the eccentricity of the wall. For this example the equivalent width is held constant and equal to the measured equivalent width of the average OH line. The asymmetric emission bump is blueward of line-center due to the direction we have chosen for the rotation of the gas and the viewing angle of disk; these choices are entirely general. For HD 100546 we see a similar blueward emission bump in the OH emission (see text).

75% of the OH arises from the inner edge, which is similar to what has been found for CH^+ in HD 100546 (Thi et al., 2011) and agrees with models of OH abundance in the inner region of the disk (Chaparro Molano & Kamp, 2012). The remaining flux comes from the outer disk. For the best fit to the CO, 35% of the luminosity arises from the wall and 65% from the surface of the disk. Fluorescence modeling in Brittain et al. (2009) found a slightly smaller percentage (15%) of the luminosity arises from the inner wall. This ratio can be changed in their model by increasing the turbulent velocity of the gas in the inner rim and decreasing the flaring or turbulent velocity of the outer disk.

We are able to fit the line profiles with the following values (and associated 99.7% confidence levels): $e = 0.18$ (0.07 to 0.30), $\alpha = -2.5$ (< -1.2), an OH fraction (arising from the inner wall) of 0.75 (> 0.44), and a CO fraction (arising from the inner wall) of 0.35 (0.19 to 0.55). The uncertainty in the eccentricity does not include the uncertainty in the viewing geometry. The minimum reduced χ^2 for fits corresponding to a sampled parameter space near these values is 1.0, which corresponds to the overall reduced χ^2 of the model fits shown in Fig. 5.10 & Fig. 5.11. If the line of sight does not fall along the semi-minor axis of the disk, then the eccentricity of the disk will be higher. If the line of sight to the disk is offset from the semi-minor axis by 10°, 20°, and 30°, the eccentricity that results in the best fit for each line of sight is 0.28, 0.45, and 0.48, respectively.

The transition from the eccentric inner wall to the circular outer disk is dynamically complicated, but models of such disks indicate the transition is sharp (Kley & Dirksen, 2006; Regály et al., 2010). Gas emitting from the surface of the disk within a few AU of the inner rim makes a minimal contribution to the line profile. As a result, the lack of smooth continuity between the eccentric inner annulus and the rest of the circular disk does not appreciably affect our line profile.

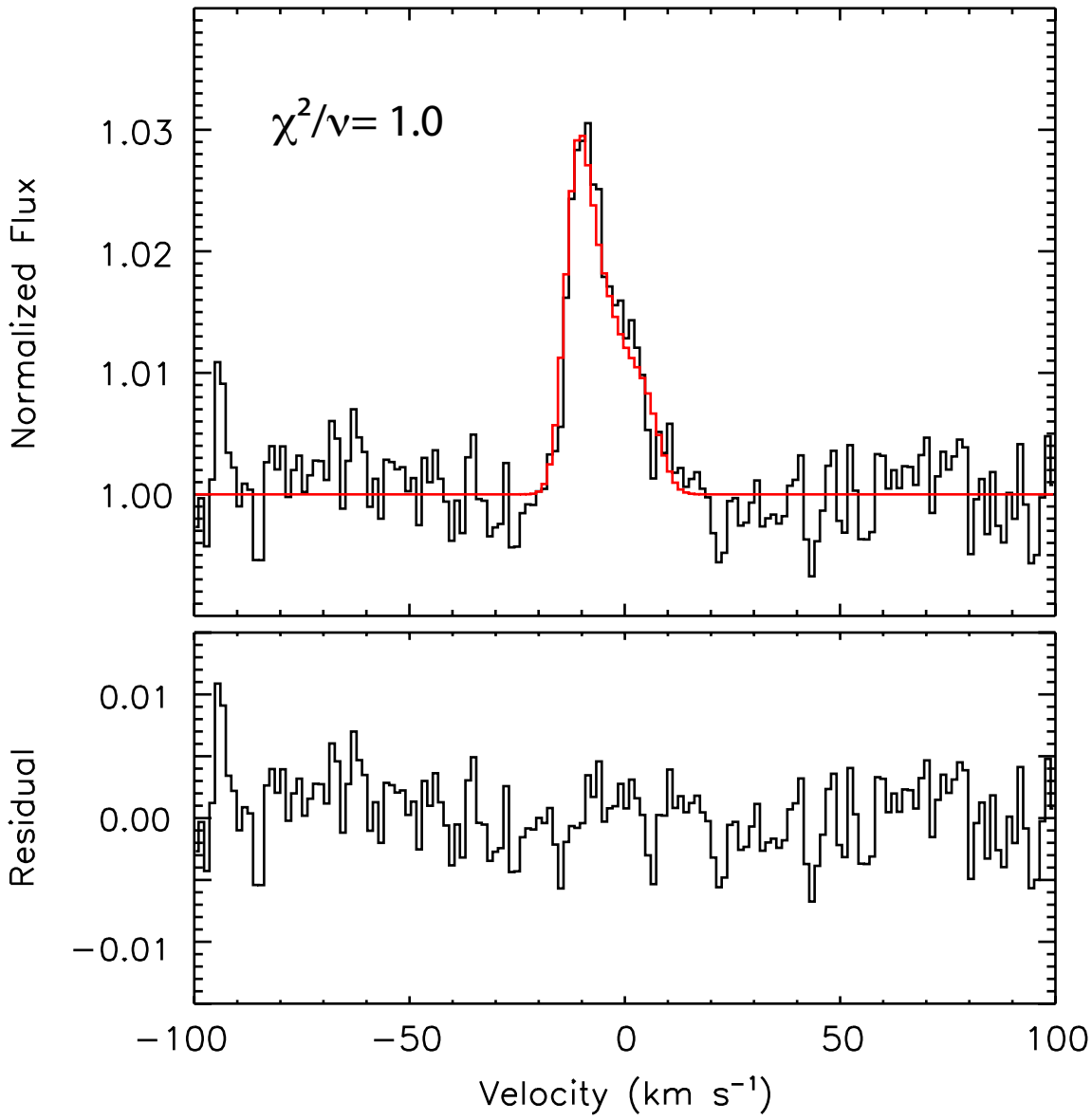

Figure 5.10 Synthesized spectrum of OH emission arising from the inner wall of a disk with an eccentricity of 0.18 in the rest frame of the star (red line). The average OH line profile (black line) is plotted in the upper panel. In the lower panel we plot the difference between the data and the model. To reproduce these line shapes we assumed that the ratio of the emission luminosity of the wall to the luminosity of the disk was approximately 3:1. Lower ratios produce a more double-peaked structure, while higher ratios do not adequately fill out the red component of the OH emission line. The minimum reduced chi-squared value, χ^2/ν, is 1.0.

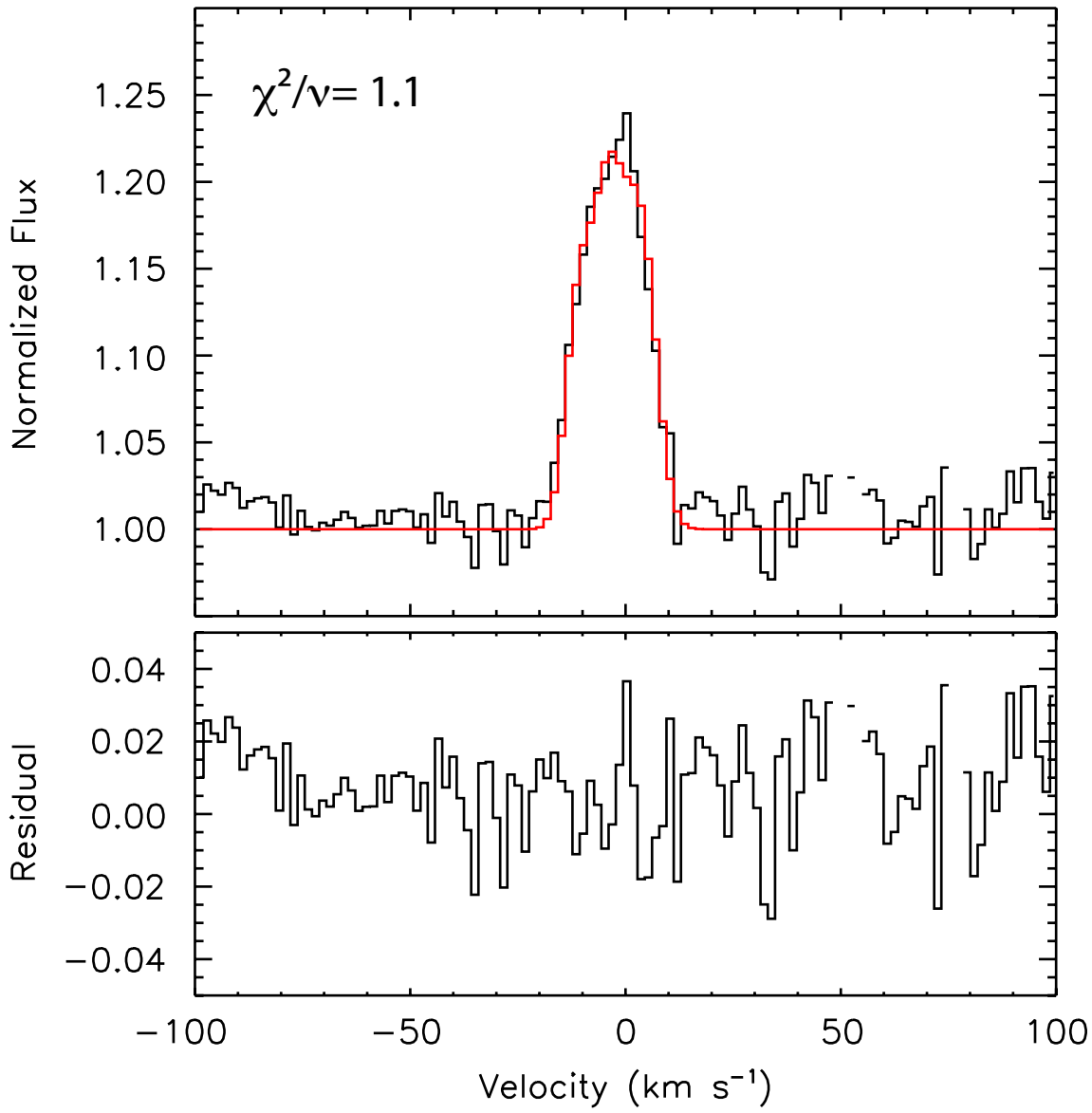

Figure 5.11 Synthesized spectrum of CO emission arising from the inner wall and the disk in the rest frame of the star (red line). The average line profile of the unblended hotband CO emission lines (black line) is plotted in the upper panel. The difference between the observed line profile and the modeled line profile is plotted in the lower panel. The synthetic CO line profile includes components from both the inner wall and disk. We assumed that the ratio of the emission luminosity of the wall to the luminosity of the disk was approximately 1:3. The reduced chi-squared value, χ^2/ν, is 1.1.

5.5 Discussion

5.5.1 Massive Companion

One possibility for the origin of the eccentricity of the inner disk is tidal interactions with an embedded gas giant planet. When a gas giant planet forms in a disk, tidal interactions between the planet and the disk cause the inner edge of the outer disk to grow eccentric (Kley & Dirksen, 2006; Papaloizou et al., 2001; Lubow, 1991). In these hydrodynamic simulations, the 1:3 Lindblad resonance induces the eccentricity. The 1:2 Lindblad resonance has a damping effect on the generation of the eccentric structure. Thus the gas must be cleared from this region of the disk.

For companion masses greater than q=0.003, where q is the ratio of the companion to stellar mass, and for a viscosity parameter value of $\alpha \sim .004$, which is typical of circumstellar disks (Kley, 1999), Kley & Dirksen (2006) show that significant eccentricities ($e \lesssim 0.25$) can be induced in the portion of the disk exterior to the orbit of the embedded gas giant. The azimuthally averaged eccentricity falls off approximately as r^{-2} where r is the distance from the star. As a result, only a narrow annulus of the disk has significant eccentricity (the precise radial dependence of the eccentricity depends on the viscosity of the gas).

The possibility of a massive companion to HD 100546 has been explored previously by several authors. First, the transitional nature of the SED may be indicative of dynamical sculpting of the disk by a massive companion (e.g. Skrutskie et al. (1990); Marsh & Mahoney (1992); Bryden et al. (1999); Calvet et al. (2002); Rice et al. (2003); Quillen et al. (2004); D'Alessio et al. (2005); Calvet et al. (2005); Furlan et al. (2006). Indeed, Kraus & Ireland (2011) have presented intriguing imagery of the transitional object Lk Ca 15 consistent with the presence of a forming planet. Bouwman et al. (2003) model the SED of HD 100546 and conclude that the inner

$\sim$10 AU of the disk is cleared. These authors suggest that the companion must be at least 5.6 M_J in order to open the hole in the disk. Second, Grady et al. (2005) used long slit images acquired with the *Space Telescope Imaging Spectrograph* on the *Hubble Space Telescope* and confirm that the inner edge of the disk is at 13 $\pm$3AU. They also find that the star is not centered in the inner hole of the disk. Rather the star falls 5 $\pm$3 AU to the northwest. If the offset is due to the eccentricity of the disk, then $e = 0.38 \pm 0.24$. This eccentricity is consistent with our result from modeling the line profile of the OH emission. In Paper II, we discuss how the observed variability in the CO fundamental emission may be an additional signpost of a forming gas giant planet orbiting HD 100546.

The result of our spectral synthesis of the asymmetric OH line profile is similar in spirit to the predictions of Regály et al. (2010), although the observations differ in detail from their model predictions. Regály et al. (2010) carried out hydrodynamic simulations of a disk with an embedded planet and used the ro-vibrational CO emission as a tracer in exploring how disk emission line profiles are modified by the presence of the planet. They confirmed the finding of Kley & Dirksen (2006) that an embedded planet induces a significant eccentricity in the disk. Planets above a critical mass ($\geq$3 M_J for a 1 $M_\odot$ star) will cause the outer edge of the gap opened by the planet to be elliptical in shape and induce a measurable asymmetry in the CO line profiles. Based on our line profile modeling, we anticipate detecting a small but observable velocity shift in the line profiles due to the difference between the projected velocities at apastron and periastron.

In the Regály et al. (2010) predictions for CO emission, the disk extends from $\sim$0.2 AU to 5 AU, and CO emits over this region of the disk, i.e., within, at, and beyond the orbit of the planet. In comparison, we do not measure any emission from the inner optically thin region of the disk around HD 100546 (i.e., within 13 AU).

Instead, the CO lines excited by UV fluorescence arise from the eccentric inner rim and the circular outer disk extending from ∼13-100 AU. The OH emission is mostly restricted to the inner rim of the disk. Thus the CO and OH line profiles of HD 100546 appear different from the synthetic profiles generated by Regály et al. (2010), but several of the elements of their scenario are consistent with the observations.

5.5.2 Comparison of OH and [OI] Line Profiles

Our results complement other studies of OH disk emission in the literature. In their study, Fedele et al. (2011) detected only the P4.5 line and therefore could not determine a temperature or the excitation mechanism with the available data. The authors do show that the [O I] λ6300Å line and OH emission lines observed toward HD 259431 have the same profile, providing some support to the hypothesis that the [O I] λ6300Å line arises from the photodestruction of OH. They also find that OH emission is more common from flared disks, which they suggest indicates the importance of fluorescent excitation. CO observations by Brittain et al. (2007) further show the width of the P30 ro-vibrational line to be similar to that observed in the OH and [O I] line for HD 295431.

Fedele et al. (2011) also observed asymmetric ro-vibrational OH lines toward V380 Ori, which they suggest could be caused by a deviation from axisymmetric Keplerian rotation or by a non-homogenous distribution of gas. Curiously, Alecian et al. (2009) find that V380 is a spectroscopic binary with a separation of rsin(i)$\lesssim$0.33 AU. Asymmetric ro-vibrational CO lines similar to the OH ro-vibrational lines presented here were observed in the recent outburst of EX Lupi (Goto et al., 2011). It should be noted that the EX Lupi system is highly variable due to rapid accretion; $\dot{M} \sim 10^{-7}\ M_{\odot}\ yr^{-1}$, (Aspin et al., 2010). Direct comparison to line for-

mation regions in HD 100546 is problematic due to HD 100546's comparably slow accretion rate; $\dot{M} \sim 10^{-9}\ M_{\odot}\ yr^{-1}$, (Grady et al., 2005).

The [O I] λ6300Å emission from HD 100546 has been interpreted as arising from the photodissociation of OH (Acke & van den Ancker, 2006). Storzer & Hollenbach (1998) show that in H/H_2 photodissociation regions far ultraviolet photons dissociate the OH molecule leaving just over half of the oxygen atoms in the $^1D_2$ state - the upper level of the [O I] λ6300Å emission line. The first pre-dissociation band of CO is near 1100Å where the UV field of HD 100546 is quite weak and atomic hydrogen can provide some shielding. In contrast, the first pre-dissociation band of OH is centered near 1600Å ($1^2\Sigma^-$; van Dishoeck & Dalgarno, 1984), which falls near the 4th positive system of CO. Thus CO and OH can self-shield one another. Acke & van den Ancker (2006) model the line profile of the O I emission from HD 100546 and show the gas is distributed from 0.8-100 AU. Building on the work by Störzer & Hollenbach (2000), they find that the surface density of the OH necessary to give rise to the O I emission is,

$$\Sigma_{OH}(R) = 3.6 \times 10^{21} (R/AU)^{-2.5}. \tag{5.3}$$

This interpretation requires the inner disk to be curiously rich in OH and very depleted in CO (N(OH)/N(CO)$\gg$100) contrary to predictions for the chemistry of inner disks (e.g. Thi & Bik, 2005).

Adopting this OH surface density and assuming the gas is in LTE, we find that the OH would need to be as cool as 450 K or have a low density to fall below our detection limit. Our upper limit on the rotational temperature of the OH is 1400 K which is comparable to the temperature of the CO at the inner rim of the disk (1400$\pm$400 K; Brittain et al. (2009)). It is not clear why OH in the inner disk

would be significantly cooler than CO beyond 13 AU. In principle, it is also possible that the gas in the inner disk is below the critical density necessary to thermalize the vibrational levels such that the effective vibrational temperature is much less than 1400 K. However, electronic excitation of the OH molecule can also populate the excited vibrational levels. If the OH is not electronically excited because it is shielded from the NUV radiation field, then it is unlikely that a significant quantity of OH is photodissociated and able to give rise to the observed O I emission. Thus it seems more likely that the inner disk is largely devoid of OH as well as CO and the [O I] λ6300Å line likely arises from a process other than the photodestruction of OH. Detailed modeling of the excitation of the OH will be considered in future work.

5.6 Contour Plots

Contour plots of the χ^2/ν statistic were generated to show its dependence on the variables over the search region (Figs. 5.12 & 5.13). The red lines indicate the necessary $\Delta\chi^2/\nu$. From these cuts along these plots through the best fit point (intersection of the red lines) the 99.7% confidence levels were extracted for each variable.

5.7 CO Observations

Like the OH lines presented above, spectroscopy of ro-vibrational CO emission offers an excellent window into the inner several AU of the disk, where it is not within the ability of current technology to resolve the disk spatially, but where however it is possible to resolve the Keplerian rotation spectrally and infer kinematic data (Najita et al., 1996; Brittain et al., 2003). In disks with massive gas components such that the disk is optically thick, the surface layer of the disk produces CO emission. Assuming that there exists a sufficiently strong enough UV continuum, the electronic states of CO, the first of which exists near 1500Å are fluoresced. Electronic transitions down to the ground state will populate the vibrational states, which then relax to the ground state. Similarly, for critical densities of H_2 of 10^{12} cm^{-3}, which are not typically found in the outer disk but which may be common in the inner disk, CO present in the disk may become collisionally excited and populate the the $v = 1$ state for temperatures of ∼1000 K. This excited state relaxes down to the ground level via an emitted NIR photon near 5 μm. In observed spectra of a circumstellar disk, both of these excitation mechanisms (collisions and UV excitation) can be important. Because collisional excitation is very dependent upon temperature and density, only the inner parts of a circumstellar disk are expected to be emitting via this process. On the other hand, the UV excitation of the bound electronic states will occur over the entire surface of the disk. The modeling of line emission will typically take both into account. Below are the results of multi-epoch observations of HD 100546 from Brittain et al. (2012) and an extended discussion of how these results affect the interpretation of the OH lines in light of planet formation scenarios and our preferred interpretation.

Spectro-astrometric measurements have been undertaken on HD 100546. The

basic principle of operation is as follows: The projected velocity of a parcel of gas in orbit in a circumstellar disk depends on its distance from the central star and its azimuthal angle. Mapping regions of equal projected velocity produces loop-like structures in projected velocity space which, depending on the observation angle, do not produce a centroid centered on the star. Because the vertical axis (axis orthogonal to the spectral axis) of the CCD gives physical information, an offset from the continuum can be calculated for each pixel along the continuum - a center of light for each vertical array on the CCD. This array of centroids can be plotted along the spectral axis which creates the spectro-astrometric signal. This is a useful tool for detecting extended or non-axisymmetric emission from the circumstellar disk. Below are the results of the spectro-astrometric measurement and modeling of HD 100546 from Brittain et al. (2012) and a discussion on their affect on our interpretation of the HD 100546 system with regards to planet formation scenarios.

High resolution (R$\sim$50000), near-infrared CO observations of HD 100546 were taken on January 14, 2006, December 21-22, 2008, and December 23, 2010 using PHOENIX at the Gemini South telescope Hinkle et al. (2003). These observations are similar to the OH observations except they cover 4 epochs, and a similar reduction technique was used to extra the spectra. A table of observations (Table 4 **?**, (Table 6.1))]2012 are presented below as well as the CO spectra from three of the four epochs. Data from 2008 were excluded because there was not significant spectral overlap between them and the other epochs.

The equivalent widths of the CO lines (hot band and fundamental lines) vary considerably over the three epochs: 2003, 2006, and 2010, evidently growing with time. Brittain et al. (2012) report that the equivalent width variation can be attributed to a drop in the continuum flux due to variability in the star. Morales-Calderón et al. (2011) report that approximately 5% of class II YSOs vary in the

Table 4. Log of PHOENIX Observations of HD 100546

Date	Integration minutes	Spectral Grasp cm^{-1}	Slit PA deg E of N	S/N	Seeing arcsec	Centroid rms milliarcseconds	Airmass sec(z)
2003 January 7	20	2029 - 2040	90	62	0.8	3.3	1.5
2006 January 14	12	2027 - 2038	90	43	0.6	4.3	1.4
	20	2141 - 2152	90	102	0.4	3.1	1.3
2008 December 21	12	2136 - 2147	37	113	0.4	2.1	1.6
2008 December 22	12	2136 - 2147	127	127	0.4	1.9	1.4
	12	2136 - 2147	307	122	0.4	1.9	1.6
2010 December 23	20	2027 - 2038	90	79	0.8	4.5	1.4

$M-$band by more than 0.5 mag in a 40 day period. This is sufficient to cause the variation seen ($\sim$0.4 mag over 8 years). The variation is not likely to be caused by a variation in the UV field of the central star as observations by Grady et al. (1997) show the FUV field of the source to vary by less than 5% over a two year timespan. Estimates by Brittain et al. (2012) show that the the variability of the hot band lines in the K band is consistent with this necessary drop in magnitude for the variation in time to be associated with a change in the continuum, though it remains unclear what is causing the variability. The fundamental lines presented by Brittain et al. (2012) have been scaled assuming the 2003 hot band data correspond to a baseline for the observations.

The CO lines presented in Fig. 5.15 show the P26 line in three different epochs (Brittain et al., 2012). Because the magnitude of the continuum likely changed between obversations, the hot band lines set the scale factor for the P26 lines; the P26 line was scaled by the factor which gives the hot band lines the same equivalent width as the hot band lines in 2003 for each epoch (2006 and 2010). The black data show the CO in 2003, the red data for 2006 and the cyan for 2010. The residuals between each year and 2003 are plotted below in their corresponding colors. The P26 residuals stand out in each year (2006 and 2010). In 2006, the excess emission is red-shifted by

$+6 \pm 1$ km s^{-1}, while the excess in 2010 is red shifted by -1 ± 1 km s^{-1}. Brittain et al. (2012) place an estimate on the emitting surface area causing these excess CO lines at $\sim$0.1 AU^2 by assuming a temperature of 1400 K and a optical depth τ_0 of unity (for collisional excitation). For each epoch, 2006 and 2010, they then model the excess emission as arising from a point source in orbit around HD 100546 at a distance of 13 AU. Given the velocity shifts indicated above, these emission excesses are located at $6^{\circ}{}^{+8^{\circ}}_{-10^{\circ}}$ east of north in 2006 and $54^{\circ}{}^{+7^{\circ}}_{-6^{\circ}}$ east of north in 2010. Given the presumed orbital radius of 13 AU, the object in 2003 would be at $-30^{\circ}{}^{+8^{\circ}}_{-10^{\circ}}$ east of north, and given the large scale height of the inner wall of HD 100546, would be obscured from view. Fig. 5.16 shows the positions of the excess given this interpretation.

5.8 Spectroastrometry

Spectroastrometry yields positional information from spectra. Taking the example of an intrinsically circular disk, inclining it along the line of sight, the disk appears elongated. Placing the slit of the spectrograph along the apparent semi-minor axis of the disk means that the gas with red-shifted velocities will be on the opposite side of the center of the slit from the blue-shifted gas. Spectrally, this will manifest itself as emission bumps above and below the centroid of the slit. Hence, physical information can be obtained from the off-spectral axis by fitting synthetic spectroastrometric curves to data. This relatively new technique is detailed in Pontoppidan et al. (2008) and is the procedure followed by Brittain et al. (2012). Spectroastrometric curves in the raw data are obvious (Fig. 5.17). At two different position angles separated by 180°, the two clear inversions of the spectroastrometric signals, illustrating the concept.

The measurement of the spectroastrometric signal is obtained by first stacking

the images in an ABBA set (Appendix B) to cancel the sky emission to first order. Flat fielding and darks are then are then applied and the resultant image is cleaned of cosmic ray hits via a boxcar routine. Typically, the spectra are not aligned horizontally with the CCD, so a rectification process is employed to 'straighten' the spectra. The extraction of the spectroastrometric signal is then accomplished by defining a continuum (defining the source beam) along the image and then for each column along this defined continuum, a centroid of the vertical PSF is measure using

$$X_{\tilde{\nu}} = C\frac{\sum_i (x_i(\tilde{\nu}) - x_0)F_i(\tilde{\nu})}{\sum_i F_i(\tilde{\nu})}. \tag{5.4}$$

where C is a correction factor used to account for flux not accounted for in the summation range, x_0 the continuum value in pixels, $x_i(\tilde{\nu})$ is the pixel within the i^{th} column, $F_i(\tilde{\nu})$ the flux at that pixel, and $X_{\tilde{\nu}}$, the spectroastrometric signal as a function of the wavenumber $\tilde{\nu}$.

In the spectroastrometric signals shown below from Brittain et al. (2012), the extracted signal is shown in the top of each panel as the solid black line, while the synthetic signal is the dot-dash line. The difference is shifted and plotted below the two. The synthetic line is generated using a Keplerian disk with the inclination of HD 100546. In 2003, the synthetic spectroastrometric signal fits the extracted signal well, in 2006 and 2010 the synthetic signal and the extract signal do not match Fig. 5.18. This implies there is extended emission on those two dates. Adding in the extra flux in the velocity bins corresponding to the two excesses for 2006 and 2010 in the synthetic spectroastrometric signal reproduces the extracted signals Fig. 5.19.

5.9 Differential Polarimetry

Differential polarimetric observations of HD 100546 were taken by Quanz et al. (2011) in 2006. They observe a curious dearth in the fractional polarization at 13° east of north, centered at approximately 27 AU from the star in the H and Ks filters, which they term a 'hole'. Curiously, this is very close to the physical location of the excess emission in Brittain et al. (2012) in 2006 ($\sim$6° east of north). Quanz et al. (2011) suggest that a forming companion interior to the 'hole' could shadow the disk decreasing the stellar flux available to be detected from that region. This further adds to the circumstantial circumstellar evidence that there is a massive object forming near 13 AU in the HD 100546 system.

5.10 Summary

The observed asymmetric emission line profile of OH can be reproduced as arising from an inner wall with an eccentricity that is in line with current estimates of the eccentricity induced by an orbiting gas giant companion. While it cannot be conclusively demonstrated that the emission arises from an eccentric rim, this hypothesis is testable. If the asymmetry is due to the eccentricity of the inner rim induced by a massive companion, then the line profile should remain approximately constant in time. One caveat is that if the orbiting planet warms the inner rim of the disk in its vicinity, the emission line profiles may shift position in velocity space as the planet moves through its orbit. If confirmed, this observation provides additional circumstantial evidence that the gap in the disk at 13 AU has been opened by a massive companion.

Other possible explanations for the line asymmetry include an origin in a wind

or a turbulent disk atmosphere. If the asymmetry is a consequence of disk turbulence, the profile shape should vary stochastically with time, and we would not continue to see the profile that we now observe. If the profile arises in a wind, the asymmetry should also be present in other molecular line diagnostics that probe similar physical conditions.

It has also been shown that the P26 CO lines are variable over the three epochs 2003, 2006, and 2010. The excess emission features from the scaled P26 lines in 2010 and 2006 over the scaled 2003 data show variability in the centroid of their profiles in velocity space. Extrapolating these velocities as an emission feature orbiting in the disk fits with the differential polarimetric data as well as the spectroastrometric data. Though not conclusive, these observations give strong circumstantial weight to the argument that a massive companion is forming near 13 AU in the HD 100546 system.

We have also shown that the OH emission lines are significantly narrower than the [O I] λ6300Å emission line. Thus we conclude that the OH and O I are unlikely to be co-spatial. The lack of OH emission from the inner disk suggests that the destruction of OH is not responsible for the [O I] λ6300Å emission line, which motivates further study into the nature and origin of the emission.

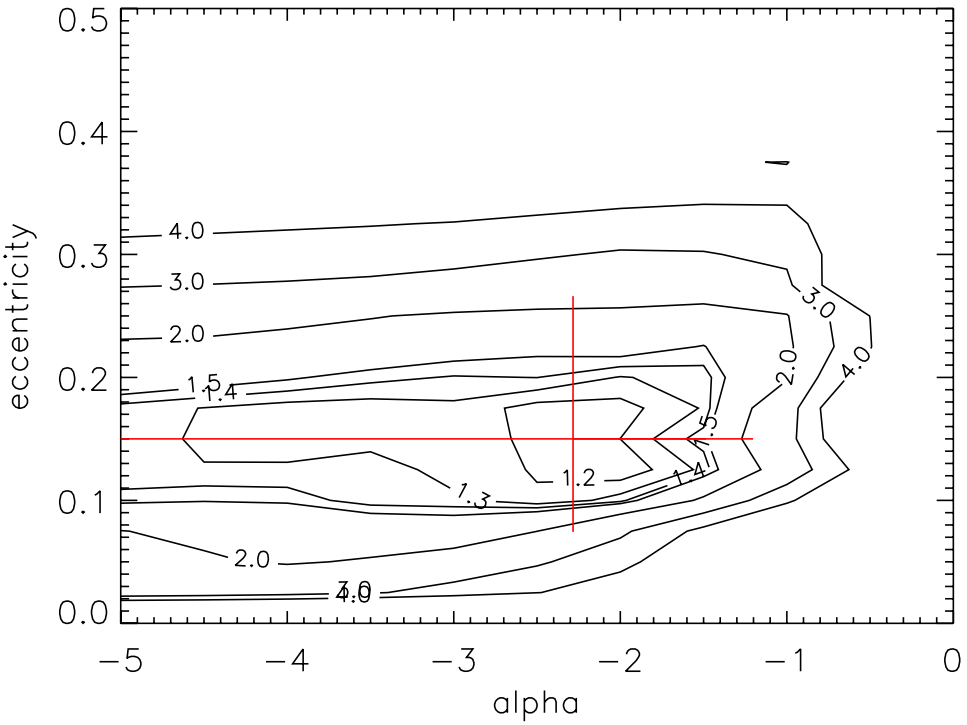

Figure 5.12 Contour plot of the alpha parameter vs. the eccentricity.

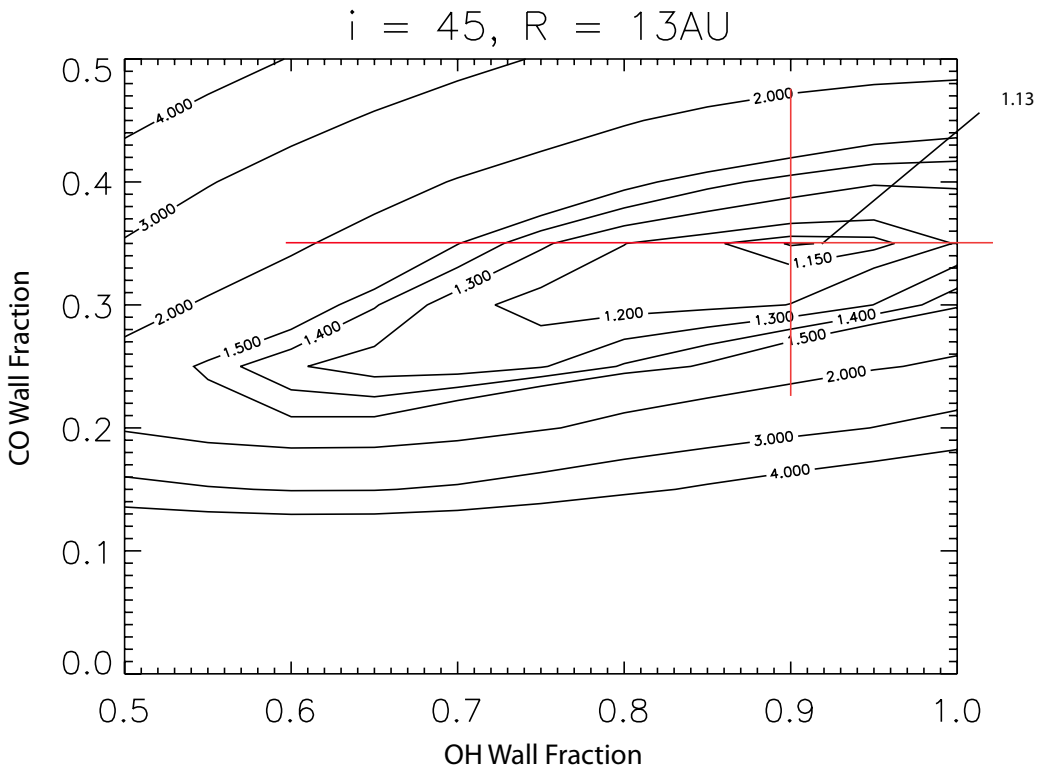

Figure 5.13 Contour plot of the fraction of the luminosity of the OH and CO coming from the wall.

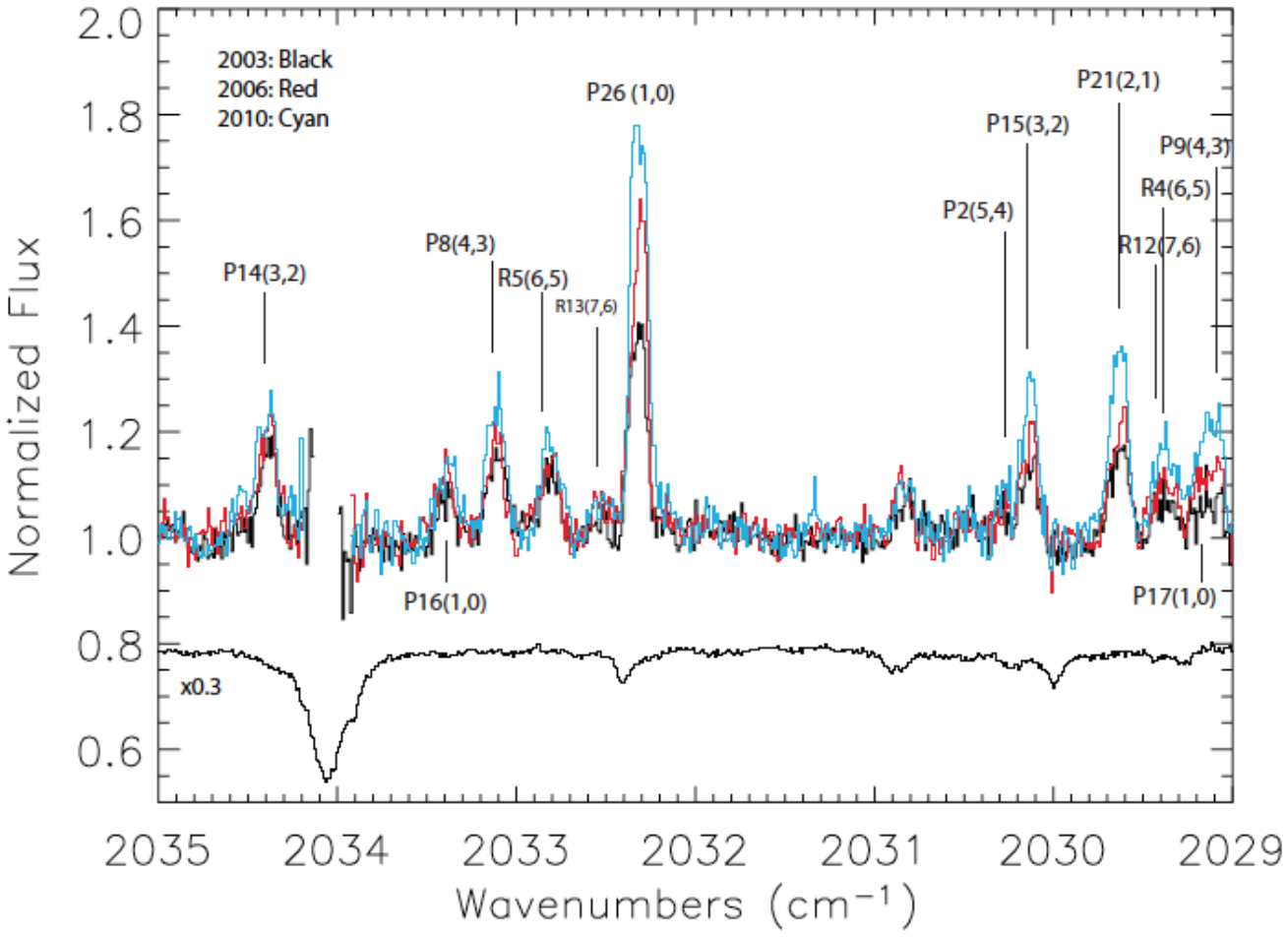

Figure 5.14 CO Lines from three epochs. (Brittain et al., 2012)

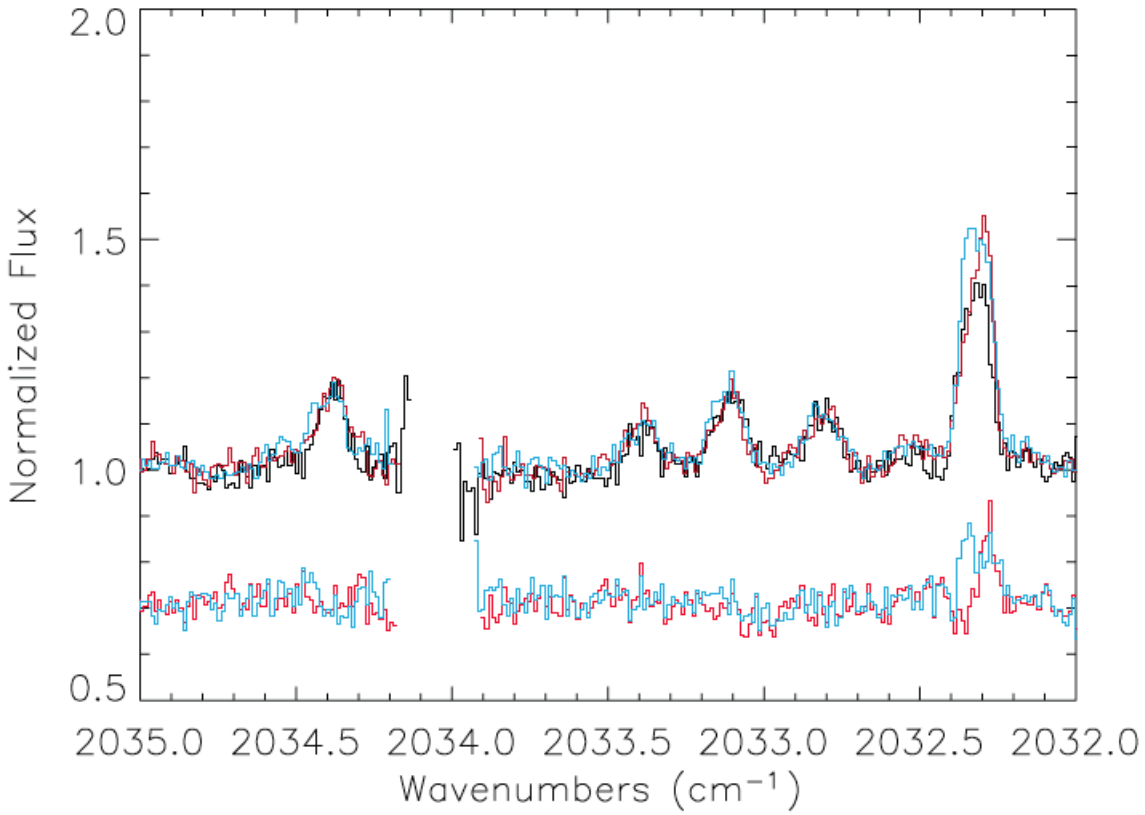

Figure 5.15 Ratios of CO Lines showing excess emission in 2006 and 2010 over the 2003 baseline. (Brittain et al., 2012, Submitted to ApJ)

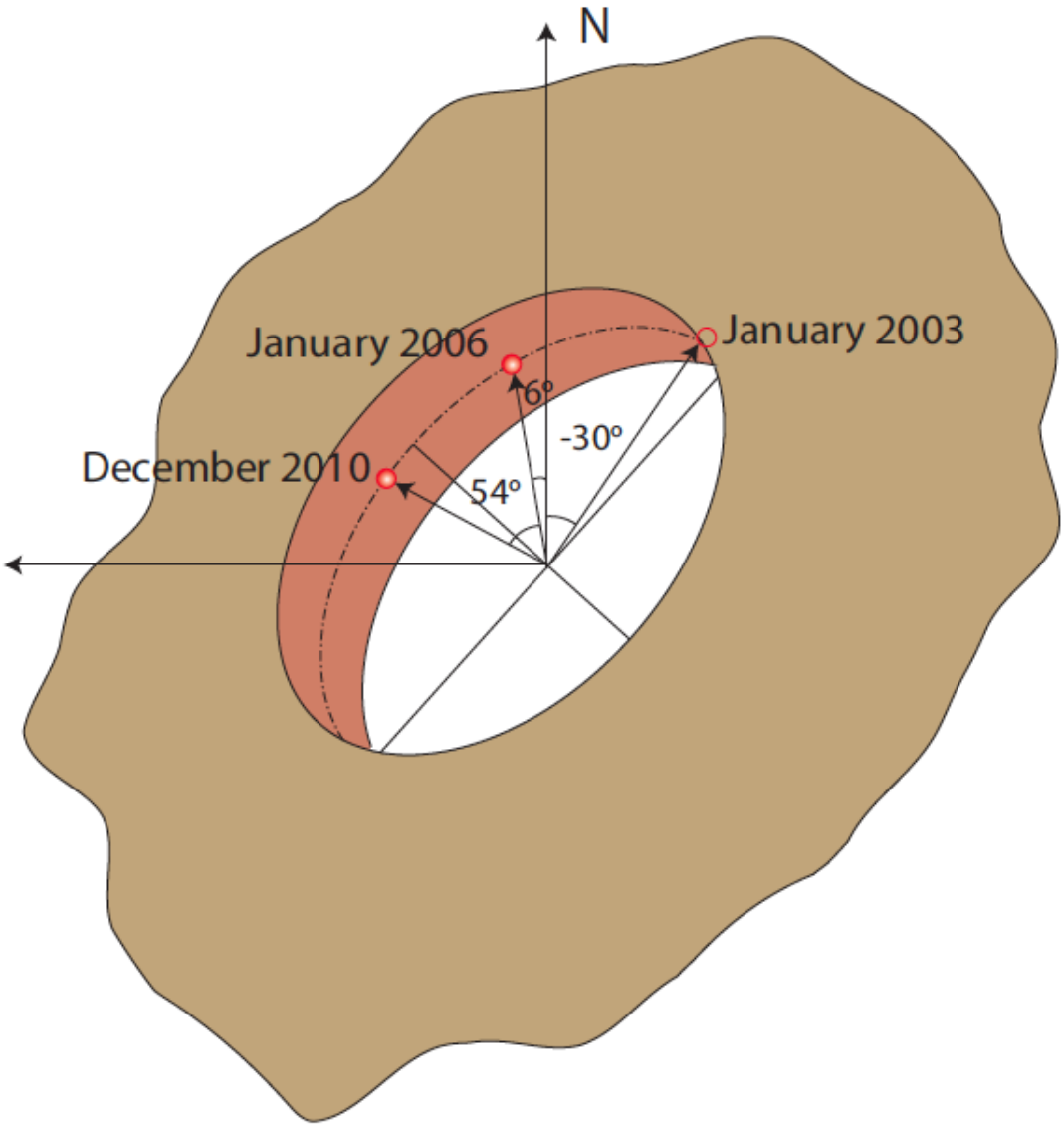

Figure 5.16 (Brittain et al., 2012, Submitted to ApJ)

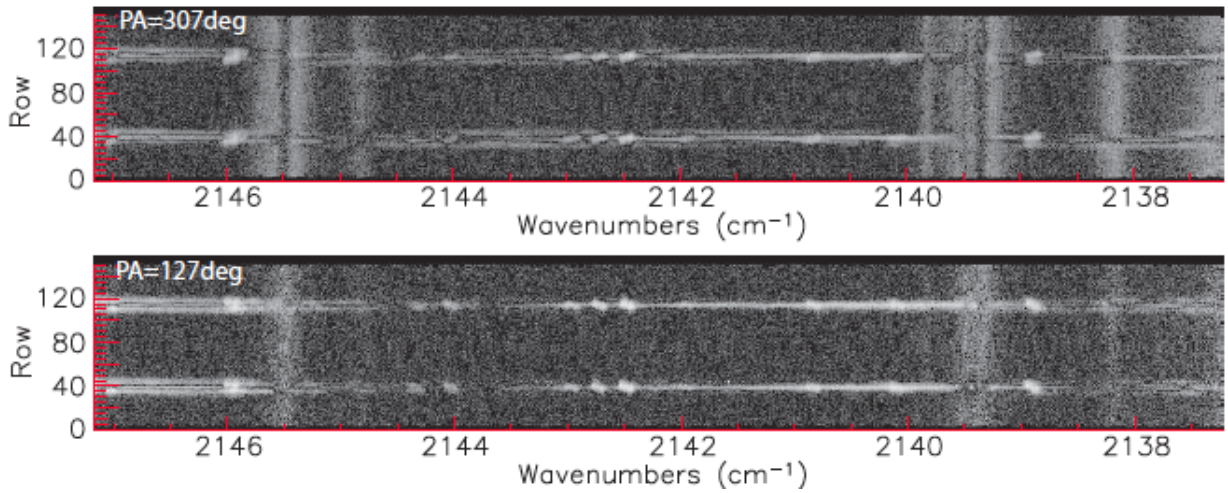

Figure 5.17 Raw spectra of HD 100546 $M-$band. (Brittain et al., 2012, Figure 4. Submitted to ApJ)

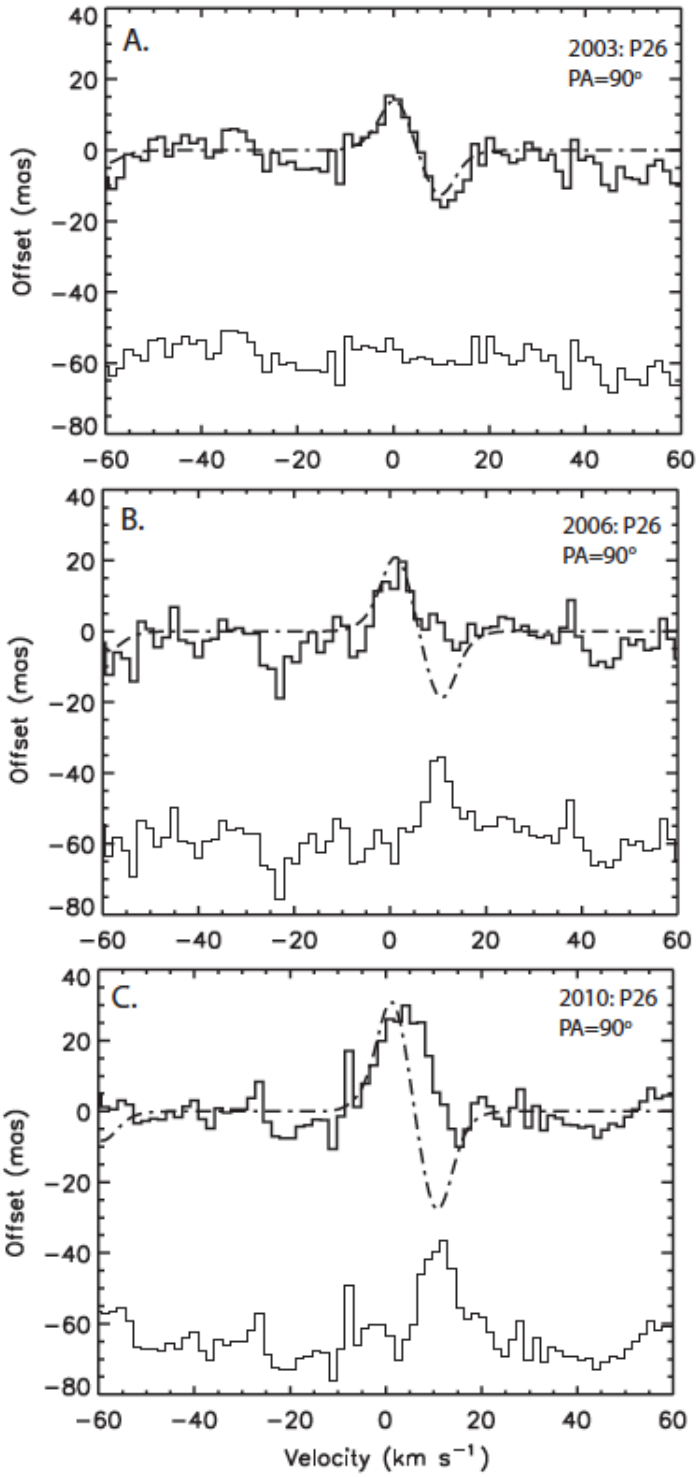

Figure 5.18 Spectroastrometry for the P26 line for the three epochs in question. (Brittain et al., 2012, Submitted to ApJ)

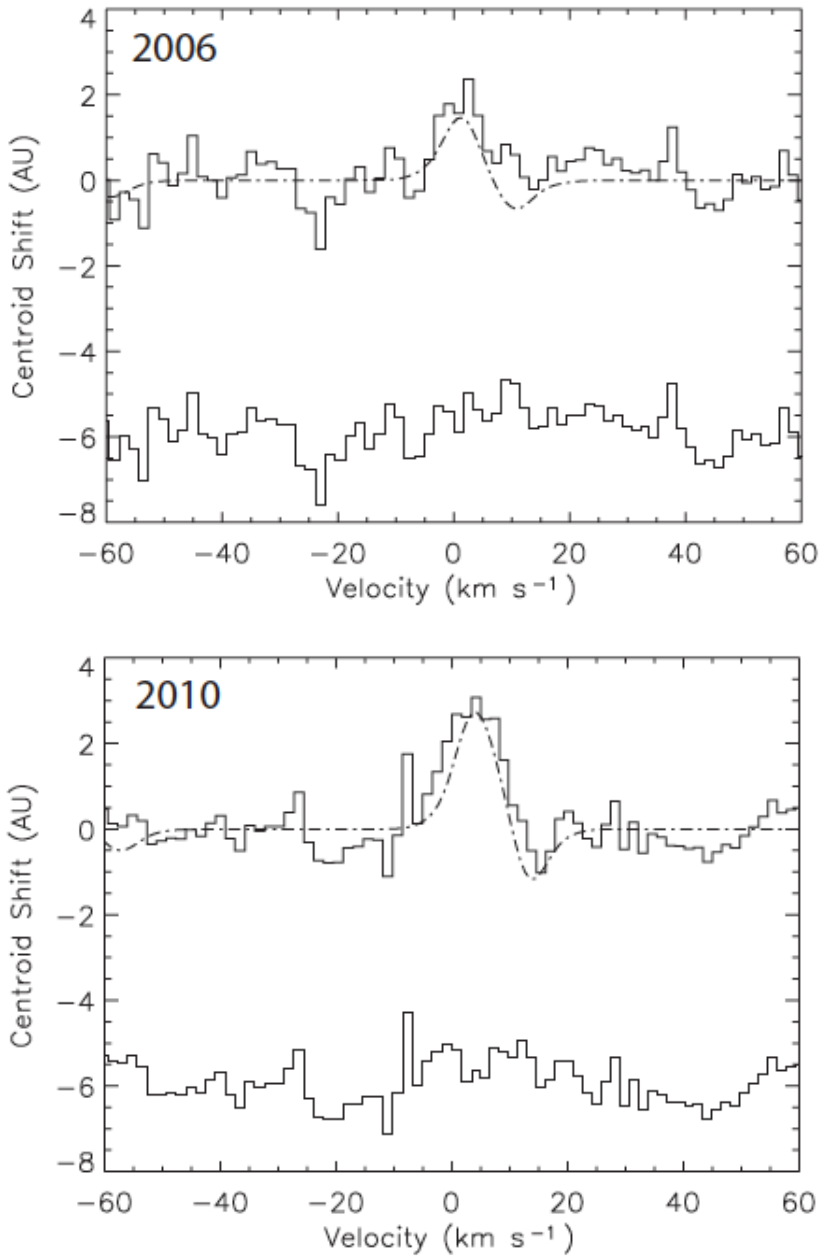

Figure 5.19 Spectroastrometry for the P26 line for the 2006 and 2010 epochs with added emission to account for an orbiting planet, with emission signatures equivalent to those measured from the excesses in the P26 line for both epochs. (Brittain et al., 2012, Submitted to ApJ)

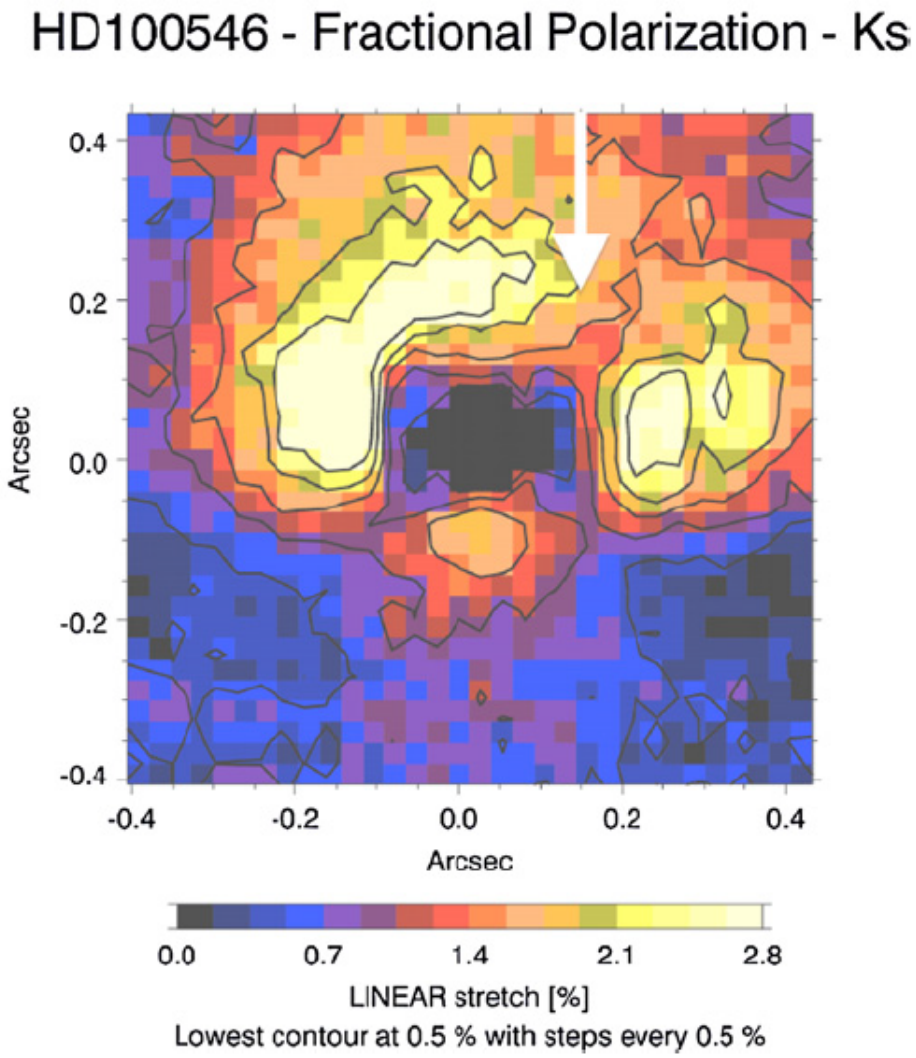

Figure 5.20 Differential Polarimetry of HD 100546. (Quanz et al., 2011)

Appendices

Appendix A Modeling of Circumstellar Disks and Spectroscopic Components

A.1 Introduction

We present a procedure to model a CO absorption spectrum from a circumstellar, Keplerian disk. This may be used to determine the velocity structure of the disk, the temperature profile of the disk, the inner and outer radii of the disk, and the inclination angle. Spectra taken at NIR wavelengths can then be compared to this code, and a best fit may be produced to extract the aforementioned information, to the degree that the model provides an accurate representation of the physical situation in the disk. We seek to apply this model to a sample of YSOs, to constrain the physical parameters that describe the disk. The following describes the theoretical framework of the calculations done in this prescription and what possible information may be extracted.

Additionally, we seek to better understand the gas excitation mechanisms in YSOs, especially in the inner AU of the disks. This region of the inner disk will likely contain the habitable zone. Understanding the chemistry and excitation mechanisms within this portion of the disk helps answer questions about how terrestrial planets obtain their final composition (including water, if present). In general, this procedure will be applied to a particular molecule's transitions, for instance, CO, to learn about the physical conditions of the disk in the planet forming region.

We intend to fit spectra of YSOs to the model spectra. Running a Monte-Carlo simulation and running a chi-square minimization algorithm on the model and source spectra will constrain the disk parameters. Degeneracies between model parameters will likely only allow a probabilistic interpretation of best fit parameters.

A.2 Discussion

We study a sample of YSOs in an ongoing survey project. To extract physical information from our sample, it is necessary to construct a model which will enable us to fit the data. The model is constructed assuming a Keplerian disk around a central star which has an input mass. This stellar parameter will be free to be varied as the user sees fit. We make the assumption that the disk has an inner and outer radius and that the midplane is a blackbody emitting at a specific temperature at a radial distance, that is, there is a radially dependent temperature profile. We also assume that the disk mass does not affect rotation and we assume a Keplerian velocity profile. The equation for a Keplerian orbit is

$$v(r) = \sqrt{\frac{GM_{\star}}{r}}. \tag{5}$$

That is, the velocity at a given distance is determined solely by the solar parameters. If we consider all of the zones of the disk, we can derive a velocity field for the disk, with appropriate definitions of the x, y, and z axes. The velocity field is given by

$$\overrightarrow{v(r,\theta)} = \sqrt{\frac{GM_{\odot}}{r}}[sin(\theta)\hat{z} - cos(\theta)\hat{x}]. \tag{6}$$

If we apply a rotation operator to the velocity field's components,

$$R = \begin{pmatrix} cos(i) & sin(i) & 0 \\ -sin(i) & cos(i) & 0 \\ 0 & 0 & 1 \end{pmatrix} \tag{7}$$

we may find a velocity field which is rotated into the appropriate frame for

our consideration, specifically one that is inclined with respect to our line of sight. Applying the rotation

$$\overrightarrow{v(r,\theta)}' = R\overrightarrow{v(r,\theta)} \tag{8}$$

we arrive at a rotated field. The velocity doppler shift of any point in the disk is given by

$$v = [1 - \frac{\hat{x} \cdot \overrightarrow{v(r,\theta)}}{c}]v_o. \tag{9}$$

This has a component directed along the line of sight with

$$|\overrightarrow{v(r,\theta)}'|_x = \sqrt{\frac{GM_\odot}{r}} cos(\theta)cos(\theta). \tag{10}$$

Using these, we can calculate the Doppler shifted line centers for each of the segments of the disk. We begin our calculations by breaking the disk up into annuli, each consecutive annulus is one velocity resolution element away from the previous. In each annulus we calculate temperature, number density, number of particles in each state, and optical depth. Each of these calculations is given below. All line values and parameters were acquired using the 2008 HITRAN database (Rothman et al., 2009). Temperature and number density are assumed to follow a decaying power law; temperature and number density are highest near the star. Populations are calculated using a Boltzmann distribution. This is acceptable because we assume that the levels are collisionally populated. For a more in-depth treatment of the quantum mechanics behind these equations, see Najita et al. (1996, see appendices) and Bernath, Peter

F. (2005).

$$T(r) = T_o[R_o/r]^{\alpha} \tag{11}$$

$$S(r) = S_o[R_o/r]^{\beta} \tag{12}$$

$$N_{J',\nu} = N\frac{ge^{-\frac{1}{T(r)}(\frac{E'}{k}+3084\nu)}}{Q} \tag{13}$$

Where g is the degeneracy of the upper state and is given by $2J'+1$, Q is the product of the rotational partition function kT(r)/hcB and the vibrational partition function $\frac{1}{e^{-3084/T(r)}+1}$, E' is given by $hcBJ'(J'+1)$, and where

$$B = B_e - \alpha_e(\nu+\frac{1}{2}) + \gamma_e(\nu+\frac{1}{2})^2 \tag{14}$$

and has coefficients given by Mantz et al. (1975). The optical depth is

$$\tau_{J',J'',\nu} = N_{J',\nu}\frac{2J'+1}{2J''+1}\frac{A_{J'\leftarrow J''}}{4\pi\tilde{\nu}^2}\phi(\tilde{\nu}), \tag{15}$$

where

$$\phi(\tilde{\nu}) = \frac{1}{2\pi b}e^{(-\frac{1}{2}(\frac{v}{b})^2)}. \tag{16}$$

The function $\phi(\tilde{\nu})$ is a line shape function that follows a Maxwell-Boltzmann distribution and depends on b, a thermal broadening term which includes turbulence. The optical depth is calculated, and applied to Beer's Law to determine the emergent luminosity from that section of the disk. The example presented here models an

absorption spectrum which has the luminosity function

$$L(\tilde{\nu}) = Area(r, \theta)B(T, \tilde{\nu})e^{-\tau_{\tilde{\nu}}}. \tag{17}$$

An emission spectrum could be generated using

$$L(\tilde{\nu}) = Area(r, \theta)B(T, \tilde{\nu})(1 - e^{-\tau_{\tilde{\nu}}}). \tag{18}$$

Both of these are functions of temperature, optical depth, and the area of the sector under consideration. Luminosity is summed over all the appropriate sectors, and calculated for each wavenumber. The synthetic spectra is then convolved with an instrument profile, which is also assumed to be Gaussian. The final convolved spectrum is compared to a spectrum from a YSO.

A possible modification to this would be into include a dynamic disk into this model. Currently, the disk assumes steady state. This modification would require the implementation of an MHD code. This model could include emission from the disk, as not all parts of the disk will necessarily be absorbing, which would model a disk which transitions from an active disk to a passive disk. Additionally, it would be possible to make the disk non-radially or non-azimuthally symmetric. This would allow us to introduce density variations in the disk and model their evolution over time.

A.3 Results

The plot below shows a real science spectrum and the model overlaid. The x-axis shows wavenumber, the y-axis shows ratioed luminosity. The calculated spectrum shows CO v(1-0) absorption lines. CO fundamental lines are marginally fit. The

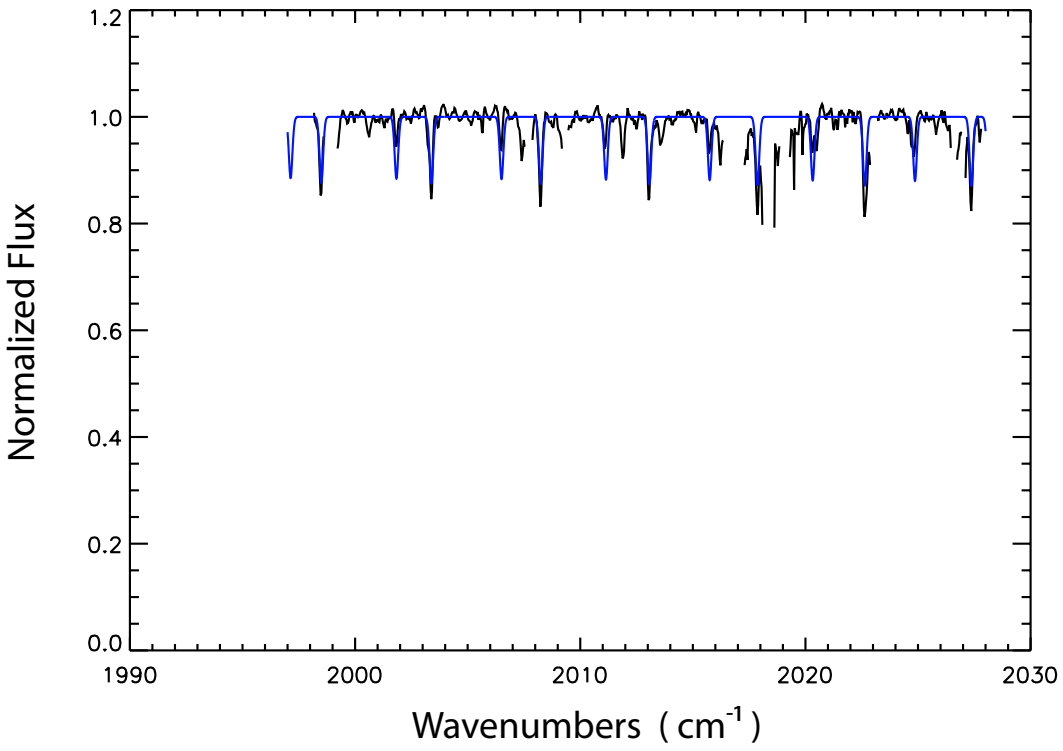

Figure 21 Synthetic and observed CO absorption lines. Spectral data are fit to Z CMa, M band and are in black. Synthetic data are in blue. The space between points has been plotted to clarify the spectral structure.

spectra plotted against the synthetic spectrum was obtained observing ZCMA, M band, an FU Orionis variable (likely). The star is in black and the model in blue. The model has been scaled to fit the YSO spectrum. This test is the zeroth order check on the code: does it match a simple spectrum? Once this test is passed, a code can be implemented in a Monte-Carlo minimization routine to constrain the chosen disk parameters. Additional lines can be added to a database to aid identification.

Appendix B ABBA Nod Pattern

B.1 ABBA Nod Pattern Derivation

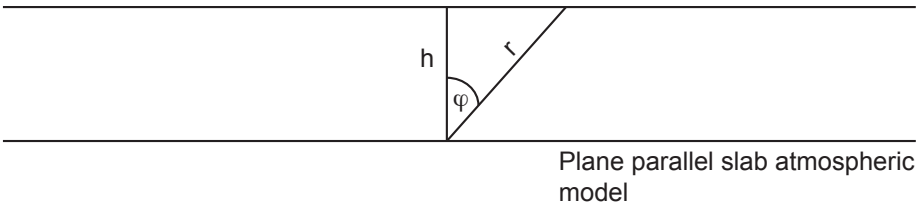

Figure 22 Diagram of plane parallel atmosphere

Because the airmass of the sky is proportional to the secant of the angle from zenith (see figure), we can compute the spectrum of the ABBA nod pattern using a Taylor expansion of the airmass function near the zenith angle of each nod position. The derivation is given below. Note that the parallel plane geometry gives the approximate answer assuming a constant density (opacity) atmosphere. If we keep this assumption but change to a spherical geometry, we retain the cancellation to first order, however we pick up a multiplicative term, $z(1 - \frac{z}{2R_\oplus})$, where z is the atmospheric height above the ground, and $R_\oplus$ is the radius of the earth.

$$r = \frac{h}{cos(\phi)} = hsec(\phi) \tag{19}$$

$$sec(x) = 1 + \frac{x^2}{2} \tag{20}$$

$$A - B - B + A = sec(x) - sec(x + dx) - sec(x + 2dx) + sec(x + 3dx) \tag{21}$$

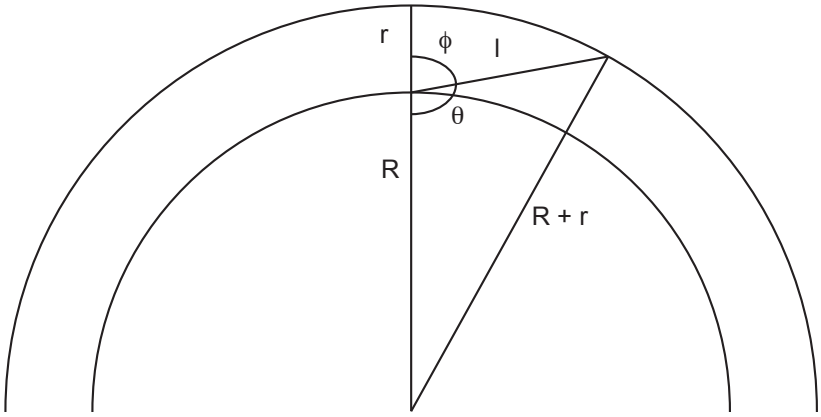

Figure 23 Diagram of spherical shell atmosphere

$$A - B - B + A = 1 + \frac{x^2}{2} - (1 + \frac{(x+dx)^2}{2}) - (1 + \frac{(x+2dx)^2}{2}) + (1 + \frac{(x+3dx)^2}{2}) \quad (22)$$

$$A - B - B + A = \frac{x^2}{2} - \frac{(x+dx)^2}{2}) - \frac{(x+2dx)^2}{2}) + \frac{(x+3dx)^2}{2} \quad (23)$$

$$A - B - B + A = 2dx^2 \quad (24)$$

Hence, in the limit of a plane-parallel atmosphere, we may cancel the sky emission to first order by using an ABBA nod pattern. If we take the atmosphere to be thin and as a spherical shell around Earth, we arrive at the geometry shown in the figure.

$$(R+r)^2 = R^2 + l^2 - 2Rlcos(\theta) \tag{25}$$

$$(R+r)^2 = R^2 + l^2 - 2Rlcos(\pi - \phi) \tag{26}$$

$$(R+r)^2 = R^2 + l^2 + 2Rlcos(\phi) \tag{27}$$

$$R^2 + 2Rr + r^2 = R^2 + l^2 + 2Rlcos(\phi) \tag{28}$$

$$2Rr + r^2 = l^2 + 2Rlcos(\phi) \tag{29}$$

$$l^2 + 2Rlcos(\phi) - 2Rr - r^2 = 0 \tag{30}$$

$$l = \frac{-2Rcos(\phi) \pm \sqrt{4R^2cos^2(\phi) + 4(2Rr + r^2)}}{2} \tag{31}$$

$$l = -Rcos(\phi) \pm \sqrt{R^2cos^2(\phi) + (2Rr + r^2)} \tag{32}$$

$$l = -Rcos(\phi) \pm Rcos(\phi)\sqrt{1 + \frac{2r}{Rcos^2(\phi)} + \frac{r^2}{R^2cos^2(\phi)}} \tag{33}$$

assuming that we are only observing at reasonable angles so that we can say $r^2 <<$

$R^2cos(\phi)$,

$$l = -Rcos(\phi) \pm Rcos(\phi)(1 + \frac{r}{Rcos^2(\phi)}) \tag{34}$$

becomes

$$l = \frac{r}{cos(\phi)}. \tag{35}$$

Hence, we have retained the original equation assuming reasonable angles for our observations. If we wish to go to $\frac{\pi}{2}$ or beyond (assuming we are on a mountain), we must use equation 15, without making any simplifying assumptions. As indicated before, this problem is solvable if we keep the r^2 term under the square root sign.

$$l = -Rcos(\phi) \pm Rcos(\phi)(1 + \frac{r}{Rcos^2(\phi)} + \frac{r^2}{2R^2cos^2(\phi)}) \tag{36}$$

$$l = -Rcos(\phi) \pm (Rcos(\phi) + \frac{r}{cos(\phi)} + \frac{r^2}{2Rcos(\phi)}) \tag{37}$$

$$l = \frac{r}{cos(\phi)}(1 + \frac{r}{2R}) \tag{38}$$

Which is a small correction to the original estimate, again assuming a non-right angle for our zenith estimate.

Appendix C Elliptic Code

C.1 Background

The following is a quick description of how we are physically modeling a circumstellar disk which has elliptical geometry with the central star at one focus. It is necessary to compute the velocity field of the disk in order to find the correct broadening for any circumstellar lines. We assume that there is no vertical (z direction) velocity, indeed we assume no vertical extent to the disk at all. This type of feature can be added in future versions. The impetus for performing this calculation is that the viewing angle of an elliptical disk can produce asymmetric emission or absorption features. Modeling these features is crucial to understanding gas physics in young stellar objects.

C.2 Mathematical Description of Physical Setup

We begin by noting that this problem is probably best attacked using a combination of polar coordinates and cartesian coordinates. The equation of an ellipse below is modified slightly by moving the origin of a new x coordinate, $x^{'}$, to the location of the star. From this origin, we can prescribe an r-coordinate and a θ coordinate which will give us the proper representation of this inherently polar system. We use the change of coordinates:

$$x \rightarrow x^{'} = x - c$$

$$y \rightarrow y^{'} = y$$

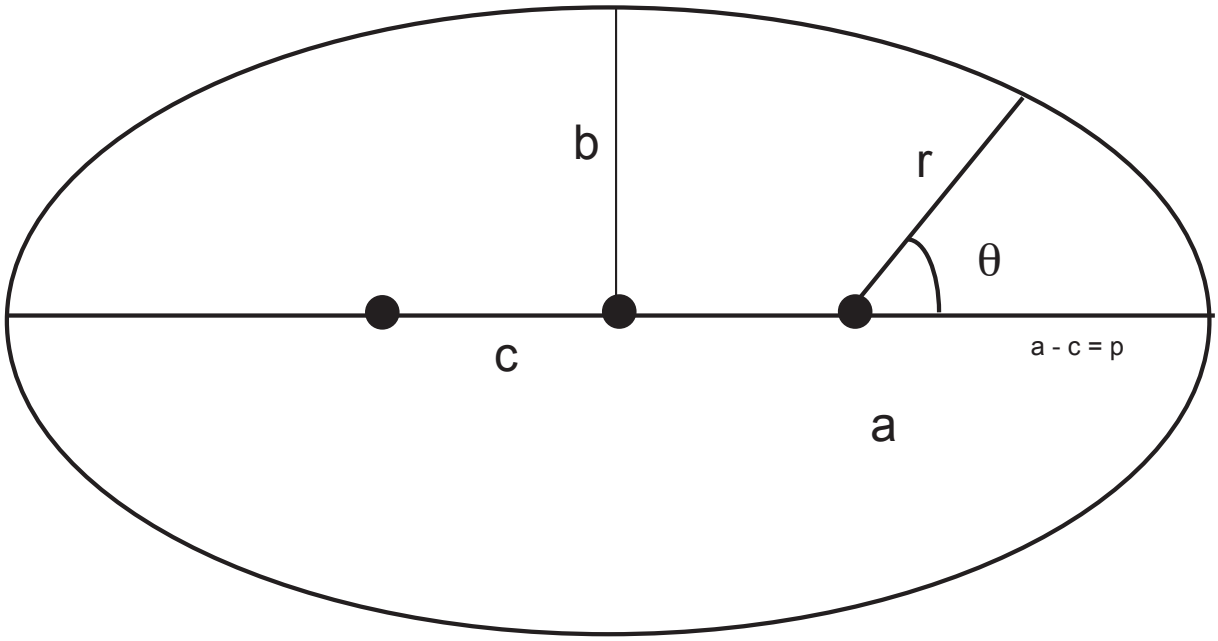

Figure 24 Diagram of an ellipse and the quantities used in this derivation.

$$\frac{(x^{'}+c)^2}{a^2}+\frac{(y^{'})^2}{b^2}=1$$

Inserting the polar representations:

$$x^{'}=rcos(\theta)$$

and

$$y^{'}=rsin(\theta)$$

We arrive at

$$\frac{(rcos(\theta)+c)^2}{a^2}+\frac{(rsin(\theta))^2}{b^2}=1.$$

Which leads to:

$$a^2(1-e^2)r^2cos^2\theta+2a^2(1-e^2)rcos\theta(ea)+a^2(1-e^2)(ea)^2+$$

$$...+a^2r^2-a^2r^2cos^2(\theta)=a^2(a^2(1-e^2))$$

after substituting for b and c with

$$b^2=a^2(1-e^2)$$

and

$$c=ea.$$

Simplifying we arrive at the following expression

$$-r^2 + (ercos(\theta) - a(1-e^2))^2 = 0$$

From which we may solve for r:

$$r = \pm(ercos(\theta) - a(1-e^2))$$

However, it is unclear which solution to use. We note that when $e = 0$, r must still be positive, hence we choose the negative solution. Hence, after solving for r,

$$r = \frac{a(1-e^2)}{1 + ecos(\theta)}$$

This equation shows that the ellipse may be parametrized by theta for a given semi-major axis a. We will use this result later. Now, we turn to the problem of identifying the velocity field with respect to the polar coordinate system. The kinetic energy, potential energy and Lagrangian for this physical system are

$$T = \frac{m}{2}(\dot{r}^2 + r^2\dot{\theta}^2)$$

$$V = -\frac{GMm}{r}$$

$$\mathscr{L} = T - V = \frac{m}{2}(\dot{r}^2 + r^2\dot{\theta}^2) + \frac{GMm}{r}$$

Hence the velocity field (this field yields the kinetic energy if projected onto itself)

$$\vec{v} = \dot{r}\hat{r} + r\dot{\theta}\hat{\theta}$$

where, in the x and y basis,

$$\hat{r} = \frac{x^{'}\hat{x}^{'} + y^{'}\hat{y}^{'}}{\sqrt{x^{'2} + y^{'2}}}$$

and after substantial simplifying,

$$\hat{r} = cos(\theta)\hat{x}^{'} + sin(\theta)\hat{y}^{'}$$

These unit vectors are the same as the unprimed vectors, but for the sake of exactness I have retain the primes. If we take the total derivative of r with respect to time,

$$\dot{r} = \frac{d}{dt}(r) = \frac{d}{dt}(\frac{a(1-e^2)}{1+ecos(\theta)}) = a(1-e^2)\frac{esin(\theta)\dot{\theta}}{(1+ecos(\theta))^2}$$

Now our job has been reduced to finding $\dot{\theta}$. We return to the Lagrangian and apply the Euler-Lagrange equation for θ.

$$\frac{d}{dt}[\frac{\partial \mathscr{L}}{\partial \dot{\theta}}] - \frac{\partial \mathscr{L}}{\partial \theta} = 0$$

$$\frac{d}{dt}[mr^2\dot{\theta}] = 0$$

This clearly implies that the quantity $mr^2\dot{\theta}$ is a constant of the motion. We identify this as the angular momentum, that is,

$$L = mr^2\dot{\theta}$$

Now, if we consider the kinetic energy of rotation at periastron and apastron, then we can ignore any energy of translation due to a change in radial distance. The

velocity vector at both of these points is orthogonal to the radial vector. Hence, the angular momentum can be written as

$$L = pmv(p)$$

where p is the periastron distance and v the velocity at periastron. Since the angular momentum is constant throughout the orbit, the previous equation can be inverted to obtain an expression for velocity at periastron:

$$v(p) = \frac{L}{pm}$$

And at apastron, $r = q$, hence

$$L = qmv(q), v(q) = \frac{L}{qm}$$

Hence, we can substitute into the kinetic energy expression and find the kinetic energy in terms of the angular momentum.

$$T(p) = \frac{m}{2}v^2(p) = \frac{m}{2}(\frac{L}{pm})^2$$

And similarly at apastron ($r = q$)

$$T(q) = \frac{m}{2}v^2(q) = \frac{m}{2}(\frac{L}{qm})^2$$

If we write the total energy at both locations, and noting that the total energy is conserved,

$$E = T(p) + V(p) = T(q) + V(q)$$

then

$$E = \frac{m}{2}(\frac{L}{pm})^2 - \frac{GMm}{p} = \frac{m}{2}(\frac{L}{qm})^2 - \frac{GMm}{q}$$

Now we note that

$$p = a(1-e), q = a(1+e)$$

And after solving the above equation for L we find that the angular momentum is

$$L = m\sqrt{GMa(1-e^2)}$$

Putting this result back into the total energy equation (at either r = p or r = q), we find the following very useful (and perhaps surprising) result,

$$E = -\frac{1}{2}G\frac{Mm}{a}$$

where 'a' is the length of the semimajor axis. Returning to the constant of motion definition for the angular momentum, we can now determine the function $\dot{\theta}$

$$m\dot{\theta}r^2 = m\sqrt{GMa(1-e^2)}$$

Hence

$$\dot{\theta} = \frac{\sqrt{GMa(1-e^2)}}{r^2},$$

into which we may now substitute the original parametrization of $r(\theta)$

$$\dot{\theta} = \frac{\sqrt{GMa(1-e^2)}(1+ecos(\theta))^2}{a^2(1-e^2)^2}$$

We now have a parametrization of our model in terms of θ. We should return to our definition of the velocity field, now that we are able to fill in some of the

information for r, $\dot{r}$, and $\dot{\theta}$. We do so, and after considerable simplifying we arrive at the velocity field for which we are searching:

$$\vec{v} = \sqrt{\frac{GM}{a(1-e^2)}}[esin(\theta)\hat{r} + (1 + ecos(\theta))\hat{\theta}]$$

As a sanity check, note that this velocity field at $\theta = 0, \pi$ produces zero radial components to the velocity, and the azimuthal component is non-zero at these points. This is what we would expect for an orbit in our geometry (see figure for definition of θ). Also, this equation returns the circular orbit equation for $e = 0$, which is perhaps a more convincing argument of its validity.

Because we will eventually wish to take all of these velocity components and dot them along our line of sight, it will aid us later to convert these direction vectors to a cartesian grid first. Our calculations on each bin of gas will be done in a polar coordinate system, but all velocity data will be given in cartesian coordinates. This simplifies calculations when computing the inner products.

We can apply the result of $\hat{r}$ in terms of $\hat{x}^{'}$ and $\hat{y}^{'}$ directly to $\vec{v}$. However, we still do not have $\hat{\theta}$. This unit vector can be found by requiring it to be orthogonal to $\hat{r}$, or letting it be a counter clockwise rotation of $\frac{\pi}{2}$. That is,

$$\hat{\theta} = \hat{R}\hat{r}$$

where

$$\hat{R} = \begin{pmatrix} cos(\phi) & -sin(\phi) \\ sin(\phi) & cos(\phi) \end{pmatrix}$$

and ϕ is the rotation angle and the hat over R denotes a matrix operator. For our rotation, $\phi = \frac{\pi}{2}$. Hence,

$$\hat{R} = \begin{pmatrix} 0 & -1 \\ 1 & 0 \end{pmatrix}$$

And, since we will be apply $\hat{R}$ to $\hat{x}^{'}$ and $\hat{y}^{'}$, we should define those as well:

$$\hat{x}^{'} = \begin{pmatrix} 1 \\ 0 \end{pmatrix}$$

$$\hat{y}^{'} = \begin{pmatrix} 0 \\ 1 \end{pmatrix}$$

We note that

$$\hat{R}\hat{x}^{'} = \hat{y}^{'}$$

$$\hat{R}\hat{y}^{'} = -\hat{x}^{'}$$

Which can be seen by either considering what these unit vectors represent or by performing the multiplication explicitly. We combine all of this together and perform the following operations:

$$\hat{\theta} = \hat{R}\hat{r},$$

and inserting the definitions for $\hat{r}, \hat{x}^{'}, \hat{y}^{'}, x^{'}, y^{'}$,

$$\hat{\theta} = \hat{R}cos(\theta)\hat{x}^{'} + \hat{R}sin(\theta)\hat{y}^{'}$$

$$\hat{\theta} = \hat{R}cos(\theta)\hat{y}^{'} - \hat{R}sin(\theta)\hat{x}^{'}$$

We may finally return to our definition of the velocity vector and apply all of our derived terms. After a considerable amount of algebra, this we arrive at the simplified expression

$$\vec{v} = \sqrt{\frac{GM}{a(1-e^2)}}[-sin(\theta)\hat{x}^{'} + [cos(\theta) + e]\hat{y}^{'}]$$

We may now compute the velocity of any point with semi-major axis a angle θ, and in an ellipse with an eccentricity $0 < e < 1$, with a central stellar mass M. This vector field will eventually be dotted with line-of-sight vectors to simulate a position angle and orientation of the disk. This is also an ideal time to calculate the total flux reaching the detector. We can easily explore the phase space of this problem by creating multiple sight lines and creating a spectrum from each. A Monte Carlo simulation or a parameter search will sample the phase space of these viewing angles and circumstellar parameters, and upon finding the maximum positive correlation between the calculated spectrum and the reduced spectrum, more finely searches the parameter space near that maximum.

Appendix D Eccentric Disk Code and Generation of Asymmetric Lines

D.1 Axisymmetric Line Generation

Lines generated from an axisymmetric disk produce symmetric line profiles, while lines generated from an eccentric disk are not (typically) symmetric. For a description of a code which calculates the spectrum of a disk with circular symmetry, see Appendix A. Adding eccentricity to disk codes which attempt to generate spectroscopic signatures is a relatively new idea (Regály et al., 2011), so the procedure followed in the code is described in detail below.

Typical parameters which define a circumstellar disk for spectroscopic comparison are the mass of the central star, the radius of the inner extent of the disk, the number of emitting particles (or equivalently, the number density) in the disk, the flaring angle of the disk, a fiducial temperature and the radial temperature dependence parameter, the eccentricity, and the viewing angle. These variables determine the velocity structure and some of the important parameters in collisional excitation of the disk. If the number density is given, emission characteristics can be determined from first principles. These parameters are entered as inputs into the code. We measure the inner extent of the disk by measuring the terminal velocities (maximum broadening velocity) of the most symmetric emission lines (CO fundamental line). For HD 100546, we measure $\sim$13 $km\ s^{-1}$, which corresponds to $\sim$13 AU, assuming circular symmetry. We seek to fit the emission lines of the measure CO and OH from the disk, and since we do not have an independent calibration of the continuum flux, we scale our observations to the measured continuum count value. We do the same for the luminosity of the disk, giving the synthetic lines the same equivalent width as

the measured lines. Because we do not know the exact distributions of the CO and OH gas in the disk, we add in two parameters which dictate the fraction of the luminosity of each which arises from the large wall at 13 AU. The remaining luminosity is assumed to arise from the optically thin surface of the disk.

We measure the rotational temperature of the disk by considering the four OH lines we did detect, the P9.5± and P10.5±, and the lines we did not detect, the P15.5± and P16.5± lines, and follow the procedure outlined in Chapter 5. This is input as the temperature at the inner radius of the disk. The α parameter determines the temperature structure (and therefore, the luminosity of the disk with radius) and is an input.

We take the input parameters eccentricity, α, and the two wall luminosity fractions (from OH and CO), and vary these over a sensible parameter space. First, we generate the disk by taking the physical parameters and creating bins for each velocity element at the velocity resolution. For example, if the velocity resolution is 1 $km\ s^{-1}$, the code will section the disk from the inner radius to the outer radius in elements radially and azimuthally of 1 $km\ s^{-1}$ in the projected velocity space. The line of sight, which is an input parameter, for the specific case of HD 100546, is along the semi-minor axis of the disk and inclined at $\sim$45°. The area of each 'bin' is calculated and the luminosity of the surface of the disk is calculated according to the luminosity function determined by Brittain et al. (2009). The luminosity in each 'bin' is assumed to be spread in a Gaussian line profile (due to thermal broadening and shocked gas). This small profile gets added to the total luminosity for each disk component. For the wall component, we assume that the luminosity is proportional

to an optically thin emitter near 2 μm, which is

$$L(v) \propto \frac{\phi(b,v)A}{e^{4528.7/T}-1}. \tag{39}$$

Here, the observation wavelength is constant throughout the calculation, and since we are only interested in the proportionality, we leave off the wavelength dependence of the Planck function. A is the area of the 'bin' under consideration, and $\phi(b,v)$ is the broadening function,

$$\phi(b,v) = \sqrt{2\pi b^2} e^{-\frac{v^2}{2b^2}}. \tag{40}$$

Here, b is the turbulent broadening term and v is the velocity deviation from zero in the rest frame of the 'bin'. For the calcuations presented here, the turbulent velocity is assumed to be 1 $km\ s^{-1}$. This process is done for each bin in the disk, for every turbulent velocity about zero deviation.

The raw luminosities of the disk and wall are generated in the rest frame of the disk, then two new luminosities are calculated, which are the linear combinations of the wall and disk components based on the input wall luminosity fractions. These new luminosities are the raw OH and CO luminosities. They are then convolved with the instrument profile (R$\sim$50,000 for Phoenix) to produce the final luminosities. These luminosities are then compared to the observed average line profiles and a chi-squared statistic is calculated to determine the appropriateness of the fit. The results of this process are shown in Chapter 5.

D.2 Visualization of Lines

The process of creating an eccentric disk is new, so for clarity, below is an walkthrough of how the eccentric lines are generated. The disk is divided into bins as

shown in Fig. 25. The wall is clearly visible with a height of ∼7 AU. The velocities projected along the line of sight are marked on the first ring of the disk. The wall sections inherit the projected velocity of the disk which is directly above it. For the circular disk, note that the terminal velocities of the disk are both ± 10 $km\ s^{-1}$. The line shape that arises from this is a combination of Fig. 29 and Fig. 30.

A portion of an eccentric disk is shown in Fig. 26. The eccentric disk model is not currently in use as the implementation has caused certain issues (such as overlapping regions of the disk). A solution has not been obvious within the current implementation, hence the wall component was assumed to be the only component which could attain an eccentricity. Any wall component with a non-zero eccentricity is generated in this fashion, where the wall 'bins' attain the projected velocity of the inner rim of an eccentric disk, however in all simulations the disk component is always assumed to be circular; the eccentric disk component is only used to create an eccentric wall component. From Fig. 26, it is evident that the projected terminal velocities on each side of the disk are different. These velocity differences have an effect on the line profile that arises from them. Fig. 27 shows the wall component only which is eccentric. This wall component will get added to the disk component (Fig. 30) to construct a luminosity profile, which then gets convolved with the instrument profile to create the final luminosity profile which is used to compare to the constructed average lines obtained from the reduced spectra.

Fig. 28 shows how the OH luminosity profile varies if the α parameter is set to zero and the eccentricity is retained (e = 0.18). In this case, blue-shifted gas has the same luminosity as red-shifted gas, however the blue-shifted part of the composite line is spread over more velocity channels, which reduces its 'height' over the continuum.

Fig. 31 shows the final OH line profile, which is a convolved linear combination of Fig. 27 and Fig. 30. This line profile is an example of a profile used to compare

against those obtained at the telescope.

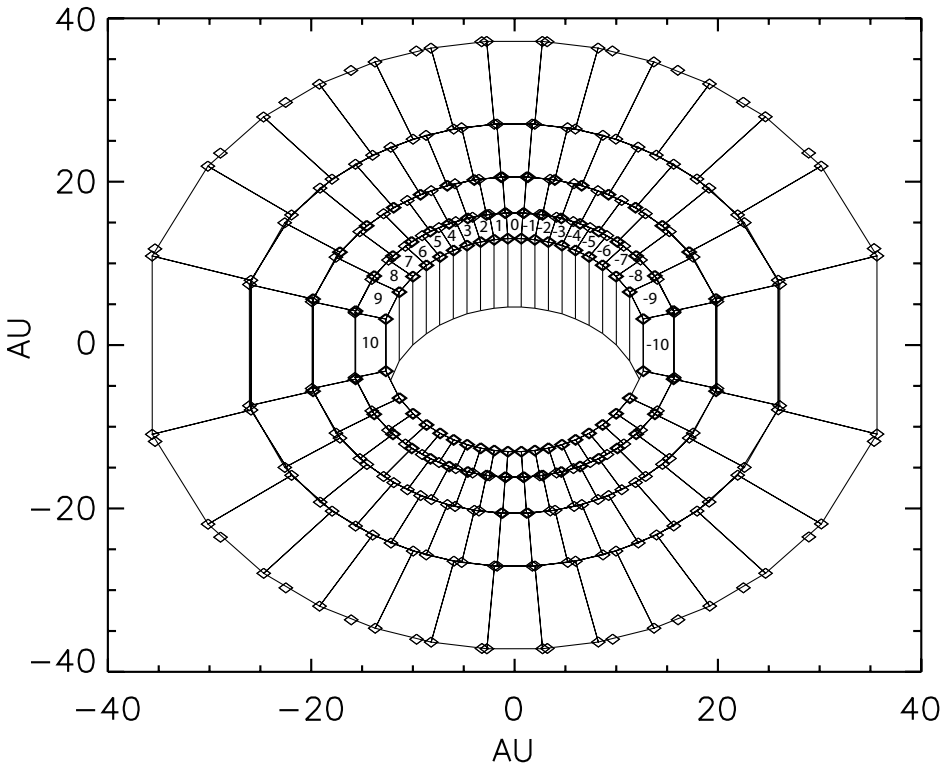

Figure 25 Circular Disk with four radial bins shown (other zones have not been plotted for clarity).

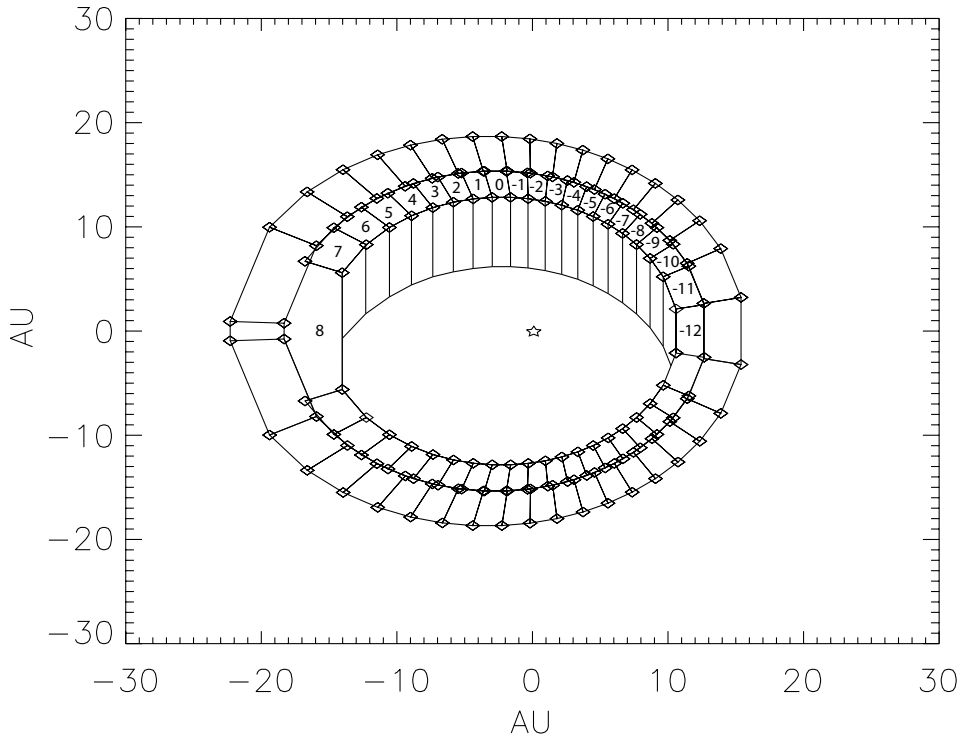

Figure 26 Eccentric Disk with two radial bins shown. The velocities for the inner rim have been shown. The redshifted gas at apastron does not get artificially cut shown in the diagram. Due to the limitations of the plotting routine and sampling, the zone at apastron appears squared-off, however the area under consideration is calculated in polar-coordinates and is much smoother than this plot indicates.

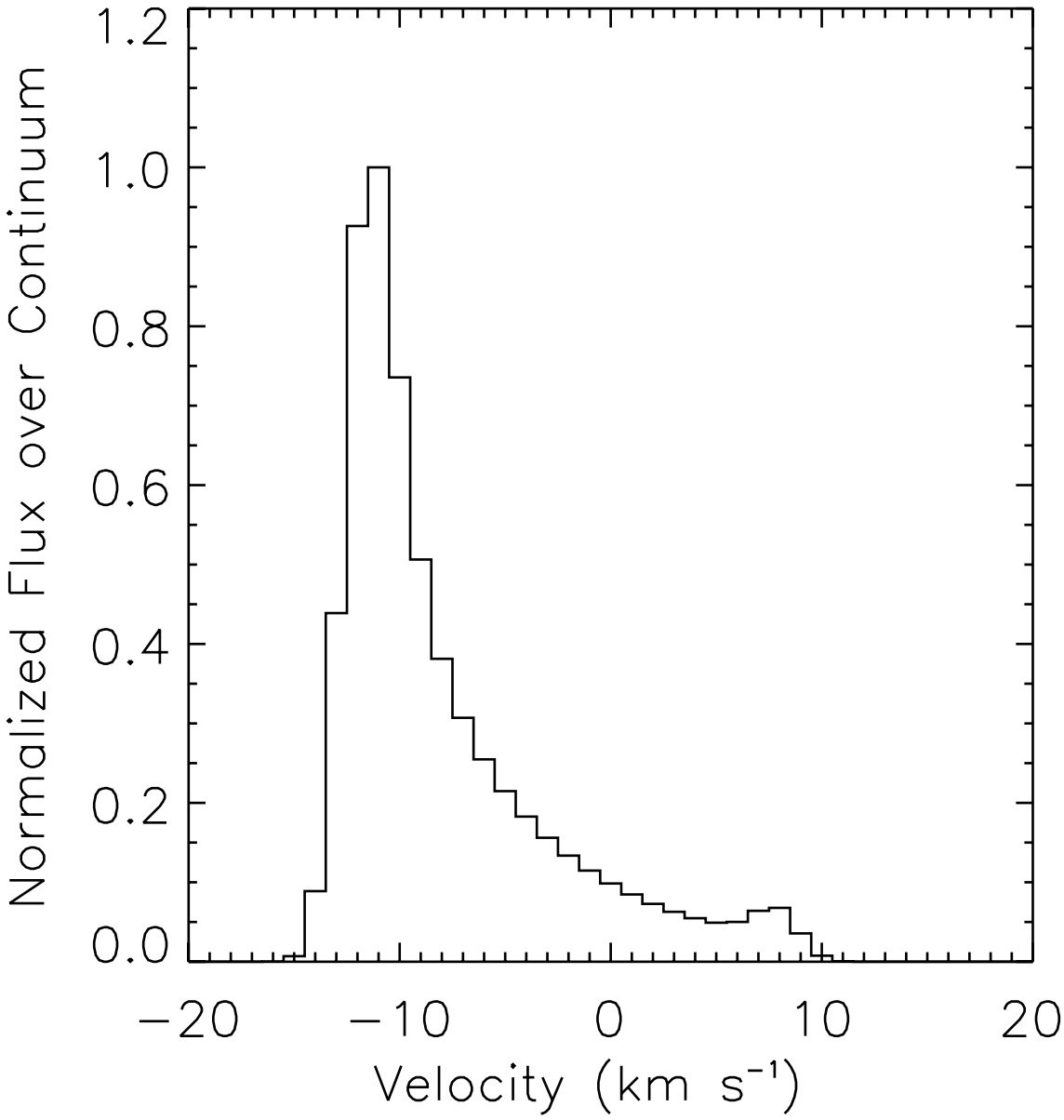

Figure 27 Unconvolved OH emission line from the eccentric wall where the α parameter is -2.5 and e = 0.18

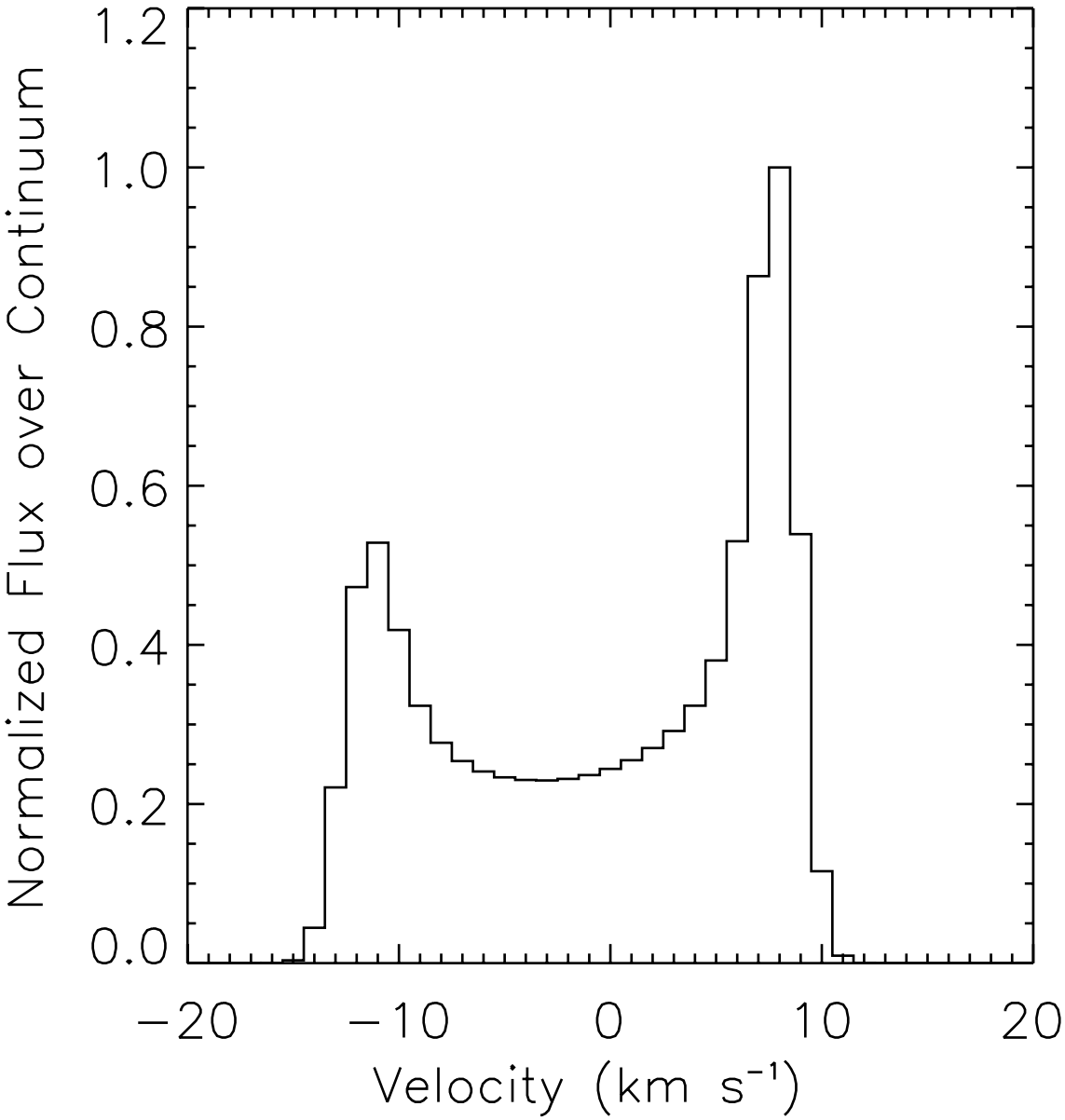

Figure 28 Non-convolved OH emission line from the circular wall where the eccentricity is 0.18 and $\alpha = 0$.

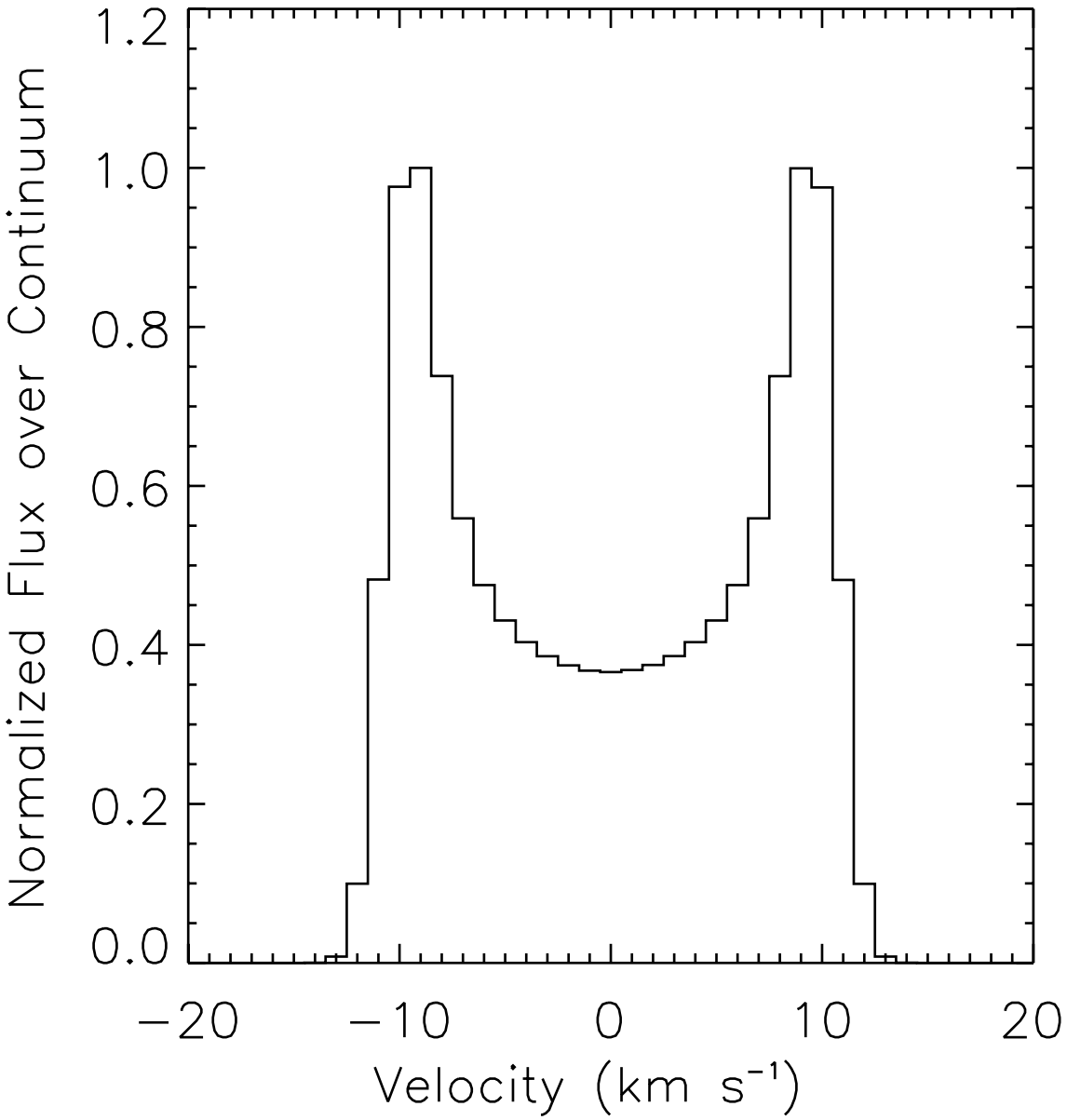

Figure 29 Non-convolved OH emission line from the circular wall where the α parameter is 0.

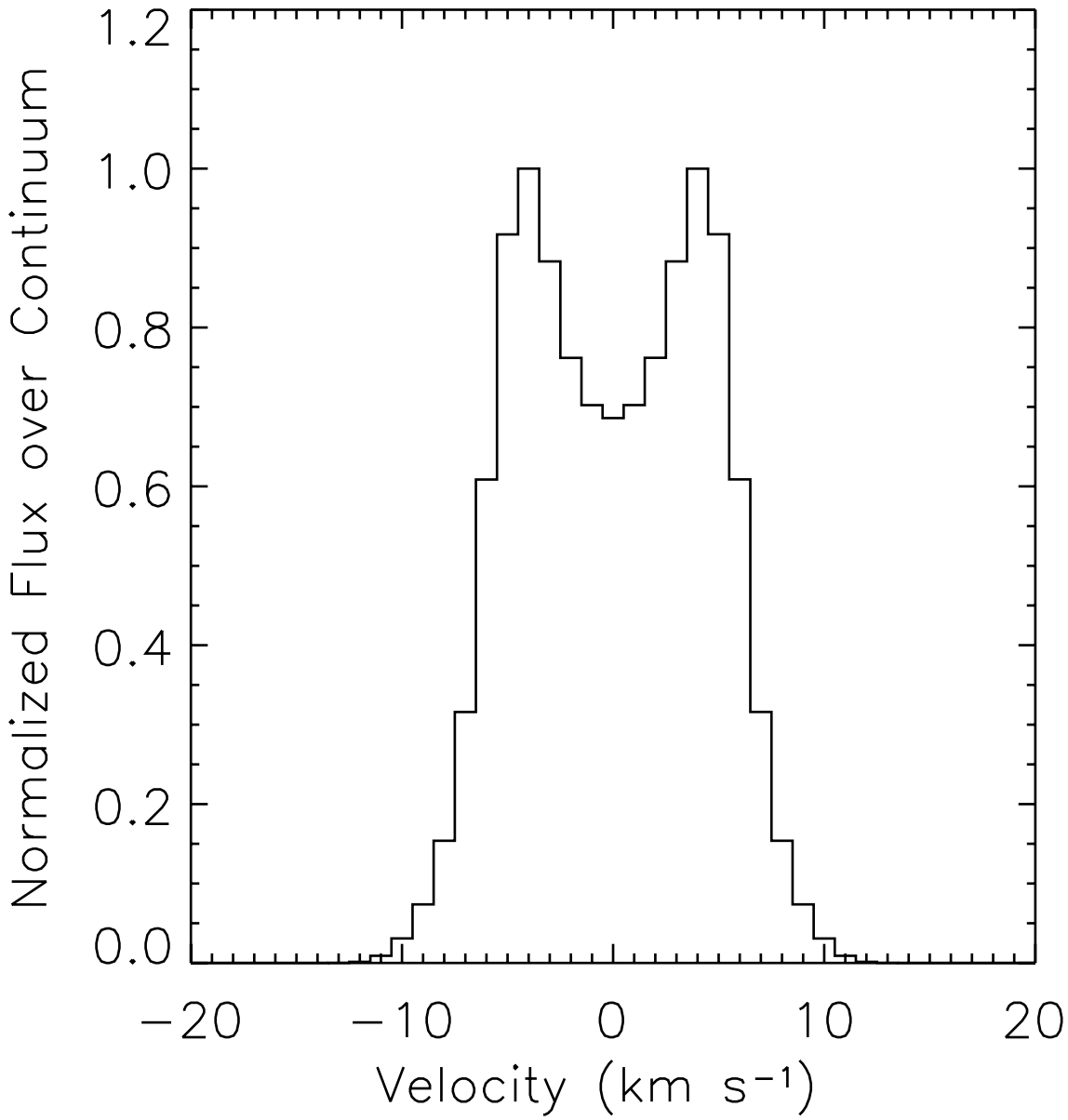

Figure 30 Non-convolved disk luminosity. This line profile will be summed with the non-convolved wall luminosity profile and then convolved with the instrument profile.

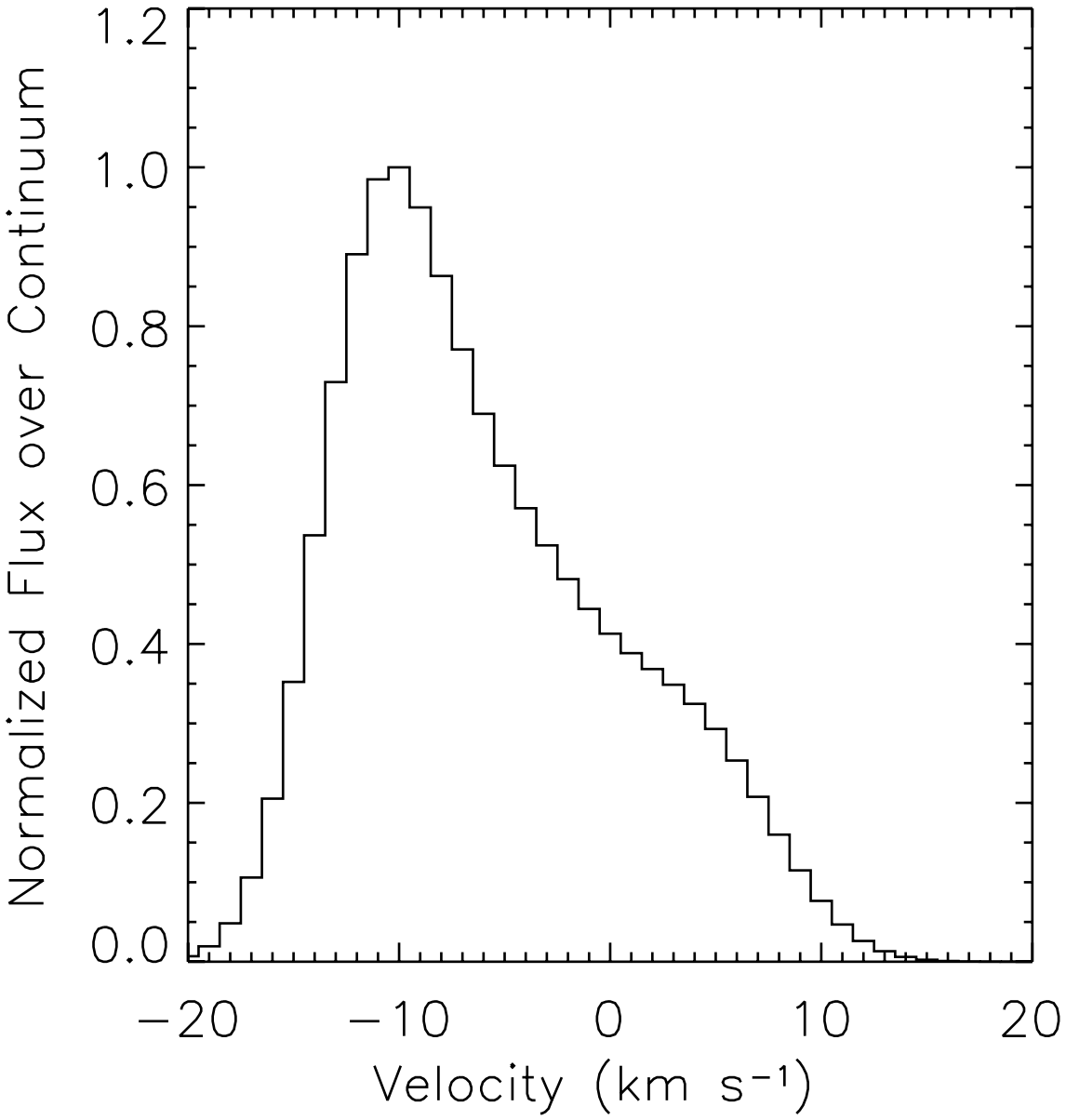

Figure 31 Convolved wall and disk luminosity with e = 0.18 and α = -2.5. This profile represents a line profile which would be used to compare against the spectral lines obtained at the telescope.

Bibliography

Acke, B., & van den Ancker, M. E. 2006, A&A, 449, 267

Acke, B., van den Ancker, M. E., & Dullemond, C. P. 2005, A&A, 436, 209

Alecian, E., Wade, G. A., Catala, C., et al. 2009, MNRAS, 400, 354

Andre, P., Ward-Thompson, D., & Barsony, M. 1993, ApJ, 406, 122

Ardila, D. R., Golimowski, D. A., Krist, J. E., et al. 2007, arXiv:0704.1507

Artymowicz, P. 1987, Icarus, 70, 303

Aspin, C., Reipurth, B., Herczeg, G. J., & Capak, P. 2010, ApJ, 719, L50

Bachiller, R. 1996, ARAA, 34, 111

Bast, J. E., Brown, J. M., Herczeg, G. J., van Dishoeck, E. F., & Pontoppidan, K. M. 2011, A&A, 527, A119

Benisty, M., Tatulli, E., Ménard, F., & Swain, M. R. 2010, A&A, 511, A75

Bernath, P. F., Oxford University Press, Spectra of Atoms and Molecules

Bouwman, J., de Koter, A., Dominik, C., & Waters, L. B. F. M. 2003, A&A, 401, 577

Brittain, S. D., Rettig, T. W., Simon, T., et al. 2003, ApJ, 588, 535

Brittain, S., Rettig, T. W., Simon, T., et al. 2007, ApJ, 670, L29

Brittain, S. D., Simon, T., Najita, J. R., & Rettig, T. W. 2007, ApJ, 659, 685

Brittain, S. D., Najita, J. R., & Carr, J. S. 2009, ApJ, 702, 85

Brittain, S. D., Najita, J. R., Carr, J. S., Liskowsky, J. P., Doppman, G. W., & Troutman, M. R. 2012, ApJ, Paper II, submitted

Bryden, G., Chen, X., Lin, D. N. C., Nelson, R. P., & Papaloizou, J. C. B. 1999, ApJ, 514, 344

Calvet, N., Patino, A., Magris, G. C., & D'Alessio, P. 1991, ApJ, 380, 617

Calvet, N., D'Alessio, P., Hartmann, L., et al. 2002, ApJ, 568, 1008

Calvet, N., D'Alessio, P., Watson, D. M., et al. 2005, ApJ, 630, L185

Chaparro Molano, G., & Kamp, I. 2012, A&A, 547, A7

Clarke, C. J., Gendrin, A., & Sotomayor, M. 2001, MNRAS, 328, 485

D'Alessio, P., Hartmann, L., Calvet, N., et al. 2005, ApJ, 621, 461

Dodson-Robinson, S. E., & Salyk, C. 2011, ApJ, 738, 131

Donehew, B., & Brittain, S. 2011, AJ, 141, 46

Doppmann, G. W., Najita, J. R., Carr, J. S., & Graham, J. R. 2011, ApJ, 738, 112

Dullemond, C. P., Dominik, C., & Natta, A. 2001, ApJ, 560, 957

Dunham, J. L., Physical Review 41, 721, (1932)

Fedele, D., Pascucci, I., Brittain, S., Kamp, I., Woitke, P., Williams, J. P., Dent, W. R. F., & Thi, W.-F. 2011, ApJ, 732, 106

Fromang, S., & Nelson, R. P. 2006, A&A, 457, 343

Furlan, E., Hartmann, L., Calvet, N., et al. 2006, ApJS, 165, 568

Goto, M., Regály, Z., Dullemond, C. P., et al. 2011, ApJ, 728, 5

Glassgold, A. E., Najita, J., & Igea, J. 2004, ApJ, 615, 972

Grady, C. A., Sitko, M. L., Bjorkman, K. S., et al. 1997, ApJ, 483, 449

Grady, C. A, Woodgate, B., Heap, S. R., Bowers, C., Nuth, J. A., Herczeg, G. J., Hill, H. G. M., 2005, ApJ, 620, 470

Guimarães, M. M., Alencar, S. H. P., Corradi, W. J. B., & Vieira, S. L. A. 2006, A&A, 457, 58

Haisch, K. E., Jr., Lada, E. A., & Lada, C. J. 2001, ApJ, 553, L153

Hartmann, L., & Kenyon, S. J. 1996, ARAA, 34, 207

Henning, T., Burkert, A., Launhardt, R., Leinert, C., & Stecklum, B. 1998, A&A, 336, 565

Herbig, G. H. 1977, ApJ, 217, 693

Herzberg, G. 1950, New York: Van Nostrand Reinhold, 1950, 2nd ed.

Hillenbrand, L. A., Strom, S. E., Vrba, F. J., & Keene, J. 1992, ApJ, 397, 613

Hinkle, K. H., et al. 2003, ProcSPIE, 4834, 353

Hinkle, K. H., Joyce, R. R., Sharp, N., & Valenti, J. A. 2000, ProcSPIE, 4008, 720

Hinkle, K. H., Cuberly, R. W., Gaughan, N. A., Heynssens, J. B., Joyce, R. R., Ridgway, S. T., Schmitt, P., & Simmons, J. E. 1998, ProcSPIE, 3354, 810

Hoffleit, D. 1939, Harvard College Observatory Bulletin, 911, 41

Jeans, J. H. 1902, Royal Society of London Philosophical Transactions Series A, 199, 1

Kley, W. 1999, MNRAS, 303, 696

Kley, W., & Dirksen, G. 2006, A&A, 447, 396

Koerner, D. W., Sargent, A. I., & Beckwith, S. V. W. 1993, Icarus, 106, 2

Kraus, A. L., & Ireland, M. J. 2011, arXiv:1110.3808

Kunde, V. R., & Maguire, W. C. 1974, Journal of Quantitative Spectroscopy and Radiative Transfer, 14, 803

Lada, C. J., & Wilking, B. A. 1984, ApJ, 287, 610

Lada, C. J. 1987, Star Forming Regions, 115, 1

Liskowsky, J. P., Brittain, S. D., Najita, J. R., Carr, J. S., Doppmann, G. W., Troutman, M. T. 2012 ApJ, 760, 153

Lin, D. N. C., & Papaloizou, J. C. B. 1993, Protostars and Planets III, 749

Lubow, S. H. 1991, ApJ, 381, 259

Lubow, S. H., Seibert, M., & Artymowicz, P. 1999, ApJ, 526, 1001

Malfait, K., Bogaert, E., & Waelkens, C. 1998, A&A, 331, 211

Mandell, A. M., Mumma, M. J., Blake, G. A., Bonev, B. P., Villanueva, G. L., & Salyk, C. 2008, ApJ, 681, L25

Mandell, A. M., Bast, J., van Dishoeck, E. F., et al. 2012, ApJ, 747, 92

Mantz, A. W., Maillard, J.-P., Roh, W. B., & Narahari Rao, K. 1975, Journal of Molecular Spectroscopy, 57, 155

Marsh, K. A., & Mahoney, M. J. 1992, ApJ, 395, L115

Masset, F. S. 2000, Disks, Planetesimals, and Planets, 219, 75

Mizuno, H., Nakazawa, K., & Hayashi, C. 1978, Progress of Theoretical Physics, 60, 699

Mizuno, H. 1980, Progress of Theoretical Physics, 64, 544

Morales-Calderón, M., Stauffer, J. R., Hillenbrand, L. A., et al. 2011, ApJ, 733, 50

Murray, N. 2011, ApJ, 729, 133

Muzerolle, J., Hartmann, L., & Calvet, N. 1998, AJ, 116, 2965

Muzerolle, J., Hillenbrand, L., Calvet, N., Briceño, C., & Hartmann, L. 2003, ApJ, 592, 266

Muzerolle, J., D'Alessio, P., Calvet, N., & Hartmann, L. 2004, ApJ, 617, 406

Najita, J., Carr, J. S., Glassgold, A. E., Shu, F. H., & Tokunaga, A. T. 1996, ApJ, 462, 919

Najita, J. R., Strom, S. E., & Muzerolle, J. 2007, MNRAS, 378, 369

Najita, J. R., Carr, J. S., Glassgold, A. E., & Valenti, J. A. 2007, Protostars and Planets V, 507

Panić, O., van Dishoeck, E. F., Hogerheijde, M. R., et al. 2010, A&A, 519, A110

Papaloizou, J. C. B., Nelson, R. P., & Masset, F. 2001, A&A, 366, 263

Pascucci, I., & Sterzik, M. 2009, ApJ, 702, 724

Pascucci, I., Sterzik, M., Alexander, R. D., et al. 2011, ApJ, 736, 13

Pollack, J. B., Hubickyj, O., Bodenheimer, P., et al. 1996, Icarus, 124, 62

Pontoppidan, K. M., Blake, G. A., van Dishoeck, E. F., Smette, A., Ireland, M. J., & Brown, J. 2008, ApJ, 684, 1323

Pontoppidan, K. M., Blake, G. A., & Smette, A. 2011, ApJ, 733, 84

Quanz, S. P., Schmid, H. M., Geissler, K., et al. 2011, ApJ, 738, 23

Quillen, A. C., Blackman, E. G., Frank, A., & Varnière, P. 2004, ApJ, 612, L137

Regály, Z., Sándor, Z., Dullemond, C. P., & van Boekel, R. 2010, A&A, 523, A6

Regály, Z., Sándor, Z., Dullemond, C. P., & Kiss, L. L. 2011, A&A, 528, A93

Rice, W. K. M., Armitage, P. J., Bonnell, I. A., et al. 2003, MNRAS, 346, L36

Rothman, L. S., et al. 2003, Journal of Quantitative Spectroscopy and Radiative Transfer, 82, 5

Rothman, L. S., et al. 2009, JQSRT, 110, 533

Salyk, C., Pontoppidan, K. M., Blake, G. A., Lahuis, F., van Dishoeck, E. F., & Evans, N. J., II 2008, ApJ, 676, L49

Schleicher, D. G., & Ahearn, M. F. 1982, ApJ, 258, 864

Skrutskie, M. F.; Dutkevitch, D., Strom, S. E., Edwards, S., Strom, K. M., Shure, M. A., 1990, AJ, 99, 1187

Solomon, P. M., Sanders, D. B., & Scoville, N. Z. 1979, The Large-Scale Characteristics of the Galaxy, 84, 35

Storzer, H., & Hollenbach, D. 1998, ApJ, 502, L71

Störzer, H., & Hollenbach, D. 2000, ApJ, 539, 751

Strom, K. M., Strom, S. E., Edwards, S., Cabrit, S., & Skrutskie, M. F. 1989, AJ, 97, 1451

Sturm, B., et al. 2010, A&A, 518, L129

Thi, W.-F., & Bik, A. 2005, A&A, 438, 557

Thi, W.-F., Ménard, F., Meeus, G., et al. 2011, A&A, 530, L2

van den Ancker, M. E., et al. 1997, A&A, 324, L33

van Dishoeck, E. F., & Dalgarno, A. 1984, ApJ, 277, 576

van der Plas, G., van den Ancker, M. E., Acke, B., Carmona, A., Dominik, C., Fedele, D., & Waters, L. B. F. M. 2009, A&A, 500, 1137

Varberg, T. D., & Evenson, K. M. 1992, ApJ, 385, 763